THE STUDY OF FEMTOSECOND SECOND HARMONIC GENERATION IN BULK CRYSTALS WITH LARGE WALKOFF

A Thesis

Submitted to the Faculty

of

Purdue University

by

Haifeng Wang

In Partial Fulfillment of the

Requirements for the Degree

of

Doctor of Philosophy

December 2003

This page is dedicated to my parents, my family.

ACKNOWLEDGMENTS

Special thanks to Zheng Zheng who gave me help in my early days in the lab, to Daniel E. Leaird for all five years of great support, to my supervisor Prof. A. M. Weiner for his excellent guidance, and to the members of my advisory committee Daniel Elliott, Vladimir Shalaev and Anant Ramdas for using their time to consider my work.

TABLE OF CONTENTS

Page

LIST OF TABLES

LIST OF FIGURES

ABSTRACT

Wang, Haifeng. Ph.D., Purdue University, December, 2003. The Study of Femtosecond Second Harmonic Generation in Bulk Crystals With Large Walkoff. Major Professor: Andrew M. Weiner.

Second harmonic generation (SHG) is a simple and effective method to generate coherent light at short wavelengths (400nm and below). In bulk nonlinear crystals there are two kinds of SHG: type I and II.

In type I SHG, the linearly polarized fundamental field interacts with itself to generate the harmonic field. The conversion efficiency is well-known for CW plane-wave sources. But for focused and pulsed sources, the process is very complicated with the spatial walkoff and temporal walkoff between the fundamental and harmonic fields. With high conversion efficiency, the pump depletion makes it even more complicated. Here we describe a theory which for the first time predicts type I SHG efficiency with both walkoffs and pump depletion in an analytical form. We will compare the results of our theory with those of a numerical model and our experiments. The comparisons strongly support our theory. Our theory can effectively predict type I SHG efficiency and improve our understanding of the SHG process.

In type II SHG, two fundamental fields with perpendicular polarizations interact with each other to generate the harmonic field. We found that it can be used to transfer a waveform from one fundamental field to the harmonic output. The harmonic waveform can be a magnified or compressed version of the fundamental waveform, depending on the configuration. We will use both theory and experiments to demonstrate this technique. It is a promising method to generate programmable waveforms in the blue and UV range, where directly programming a waveform is still challenging.

1. PART I: INTRODUCTION TO TYPE I SHG STUDY

1.1 Second Harmonic Generation with Walkoffs

Second harmonic generation (SHG), also known as frequency doubling, is an important nonlinear optical process which was first demonstrated shortly after the invention of the laser [1]. SHG provides a simple way to generate coherent light at wavelengths near 400nm or below, which is attractive to numerous applications including optical data storage, optical printing, visual displays, photolithography, and medical uses. It is also widely used for measurement of ultrafast optical pulses via autocorrelation [2] or frequency resolved optical gating [3].

From the classical point of view, the second harmonic (SH) field E_2 is radiated by the second-order nonlinear dielectric polarization P_2, which is excited by the fundamental field E_1. In a nonlinear medium, the dielectric polarization P is related to the input field E_1 by the matter equation [4–6]:

$$P(E) = \epsilon_0(\chi^{(1)}E_1 + \chi^{(2)}E_1^2 + \chi^{(3)}E_1^3 + ...) \tag{1.1}$$

$\chi^{(1)}$ is the linear dielectric susceptibility. $\chi^{(2)}$ is the second-order nonlinear dielectric susceptibility and it is generally a third-order tensor. The second-order polarization field is:

$$P_2 = \epsilon_0\chi^{(2)}E_1^2 \tag{1.2}$$

If E_1 oscillates at frequency ω_1, P_2 will have SH components at frequency $\omega_2 = 2\omega_1$. If E_1 contains several different frequency components, P_2 can have sum or difference frequency components. As a third-order tensor $\chi^{(2)}$ has 27 components. But after applying symmetry restrictions [7], there are only 10 independent non-zero components. In a nonlinear crystal, there are extra symmetry restrictions associated with the crystal structure, and so the number of independent components is further

reduced. Those components determine how the SH field is related to the fundamental field(s). In the so-called type I SHG, the fundamental field and the SH field have perpendicular linear polarizations, such as (in MKS units):

$$P_{2x} = 2\epsilon_0 d_{eff} E_{1y}^2 \tag{1.3}$$

where d_{eff} is the effective nonlinear coefficienct. In a unaxial crystal, in the case of type I SHG, one of the fundamental field and the harmonic field must be an ordinary wave (o-wave), whose polarization is perpendicular to the plane formed by the wave vector and the crystal optic axis, and the other must be an extraordinary wave (e-wave), whose polarization is in the plane formed by the wave vector and the crystal optic axis. The refractive index of o-wave doesn't change with the propagation direction, but the refractive index of e-wave does. If the fundamental wave is an o-wave, it's called ooe SHG, otherwise it's eeo SHG. Type I SHG is very widely used because it's very simple and effective.

Conversion Efficiency is defined as the energy of the generated SH wave divided by the energy of the input fundamental wave. High conversion efficiency is always preferred if it doesn't significantly degrade other parameters. The conversion efficiency in type I SHG for CW plane-wave source is well-known [8]. With the approximation of low efficiency (no pump depletion), the efficiency η is:

$$\eta = \eta_{max} sinc^2(\Delta k L/2) \tag{1.4}$$

where L is the crystal length and $\Delta k = k_2 - 2k_1$ is the phase mismatch. k_1 and k_2 are the wave vectors of the fundamental and SH light respectively, and they are in the same direction. The above equation shows that for CW plane-wave source SHG is the most efficient when $\Delta k = 0$ or $n_2 = n_1$(phase matching condition), where n_1 and n_2 are the refractive index of the fundamental and SH light respectively. In an isotropic media, the phase matching condition is impossible due to material dispersion. But it can be achieved using the birefringence of a nonlinear crystal, and it requires the input light to enter the crystal at a certain angle with respect to the

optic axis (the phase matching angle θ_m). Under the phase matching condition, the conversion efficiency for CW plane-wave source is:

$$\eta = \tanh^2(\kappa |A_0| L) \tag{1.5}$$

$\kappa = \omega_1 d_{eff}/n_2 c$ is a constant. c is the light speed and A_0 is the input fundamental field amplitude.

However, CW plane-wave sources can hardly achieve high efficiency in reality. As a second-order process, there are two major ways to increase SHG efficiency for a specified nonlinear material: increase input field intensity and increase the interaction length (or crystal length in type I SHG). The former invokes the need for pulsed laser sources and beam focusing; the latter increases the significance of temporal and spatial walkoff effects, which we don't need to consider if we use CW plane-wave sources.

The temporal walkoff is the phenomenon that due to the different group velocities of the fundamental and SH pulses in the media, they are separated in time when propagating. The characteristic length of this phenomenon, which we call the temporal walkoff length (also refered to as the quasi-static interaction length [9]), is defined as:

$$l_T = t_p/\beta \tag{1.6}$$

where t_p is the FWHM input pulse duration in intensity. β is the group velocity mismatch (GVM), and it's defined as:

$$\begin{aligned} V_1 &= \frac{\partial \omega}{\partial k_1} \\ V_2 &= \frac{\partial \omega}{\partial k_2} \\ \beta &= \frac{1}{V_2} - \frac{1}{V_1} \end{aligned} \tag{1.7}$$

V_1 and V_2 are the group velocities of the fundamental and SH pulses respectively.

The spatial walkoff is the phenomenon that the fundamental and SH pulse energy travel at different directions in the nonlinear media, and so they are separated in space when propagating. Specifically in a nonlinear crystal, an e-wave sees

anisotropic index, and that causes its Poynting vector (direction of energy flow) to deviate from the wave vector by a small angle ρ (called the walkoff angle or anisotropy angle [9]). Define θ as the angle between the wave vector and the optic axis of the crystal, $\rho = 0$ only when $\theta = 90°$. An o-wave sees isotropic index, and its Poynting vector is in the same direction as the wave vector. As we mentioned before in type I SHG one of the two waves (fundamental input or SH output) must be an o-wave and the other must be an e-wave. Under the phase matching condition their wave vectors must be in the same direction, so there is the walkoff angle ρ between their energy flow directions. Here we define a spatial walkoff length:

$$l_S = \frac{w_0}{\rho} \tag{1.8}$$

w_0 is the input beam waist radius (e^{-2} intensity radius). There is no spatial walkoff if $\theta_{pm} = 90°$, which is called non-critical phase matching (NCPM).

The walkoff effects can reshape the spatial and temporal profile of the output light field significantly if the crystal is long compared with the characteristic walkoff lengths. Specifically, large temporal walkoff can reduce the phase matching bandwidth and broaden the output pulse; large spatial walkoff can make the output field spread out in the direction of the spatial walkoff. When we use focused and pulsed sources, both walkoffs exist and the SHG process is very complicated. When the conversion efficiency is high enough that the pump depletion has to be taken into account, the SHG process is even more difficult to deal with. Despite four decades of experience with SHG, calculation of SHG efficiency via analytical method is rather involved even for type I processes unless significant simplifying assumptions are made.

1.2 Former SHG Theories

There were studies of type I SHG efficiency under various approximations. The effect of spatial walkoff and focusing on the conversion efficiency and output SH field profile were already studied carefully for CW Gaussian-beam sources in a series of

papers in the 1960s [10–13]. A classic paper written by Boyd and Kleinman [13] carefully investigated SHG with a continuous-wave laser in the case of no source depletion (low efficiency). Their result for the conversion efficiency is:

$$\eta = \gamma \frac{P_\omega}{b} \int_0^L \int_0^L \frac{\exp\left(i\Delta k(z_1 - z_2)\right) \exp\left(-(z_1 - z_2)^2 / l_S^2\right) dz_1 dz_2}{(1 - i\tau(z_1))(1 + i\tau(z_2))} \tag{1.9}$$

Here $\gamma = \frac{4\kappa^2 n_2}{\lambda_1 c \epsilon_0 n_1} = \frac{\omega_2^2 d_{eff}^2}{n_1 n_2 \lambda_0 c^3 \epsilon_0}$ is the coupling coefficient; λ_0 is the fundamental wavelength in vacuum; P_ω is the fundamental power; $b = 2\pi n_1 w_0^2 / \lambda_0$ is the confocal parameter (depth of focus) of the Gaussian beam; $\tau(z) = 2(z - z_0)/b$ is a function of z, and z_0 is the beam waist position, assuming the crystal region is from $z = 0$ to $z = L$.

Based on the above equation, they gave simple formulas for the conversion efficiency valid for different parameter regions (e. g., strong vs. weak focusing, strong vs. weak spatial walk-off). This is very helpful for estimating efficiency and understanding the physics in continuous-wave SHG. However, as short pulse lasers replace CW lasers in much nonlinear optics research, the two basic assumptions of [13] (CW source and low efficiency) are generally no longer true.

The effect of GVM and temporal walkoff for pulsed plane-wave sources was also studied in early papers [14–17]; its effect on autocorrelation measurements of ultrashort pulses [18] and on pulse shaping using quasi-phase-matched gratings [19] has also been analyzed. A paper from our group [20] studied the $860nm \Rightarrow 430nm$ SHG in a 3mm $KNbO_3$ crystal with non-critical phase matching, and worked out the focusing dependence of type I SHG with short pulse sources and large temporal walkoff, but without spatial walkoff and without pump depletion:

$$\eta = \gamma \frac{U_\omega}{t_p} l_T \arctan(\frac{L}{b}) = \gamma \frac{U_\omega}{\beta} \arctan(\frac{L}{b}) \tag{1.10}$$

It indicates that in the absence of spatial walkoff, the efficiency will increase monotonically with tighter focusing and approach an upper limit. Considering Equation 1.6, it also indicates that in the limit of large temporal walkoff the conversion efficiency only depends on the pulse energy and crystal length, but doesn't depend

on the pulse duration or peak intensity. This is an interesting phenomenon which seems to contradict the belief in the CW case. In a recent paper [21], the authors studied the same SHG process in a 10mm $KNbO_3$ crystal ($12ps$ temporal walkoff), and observed that a 120fs source and a 2ps source result in similar efficiency with the same pulse energy although the peak intensity of the 2ps pulses is 20 times lower than the 120fs pulses. This is an evidence which strongly supports the above theory. Since the spatial walkoff was not included in this theory, it's only valid for the case of non-critical phase matching or nearly plane-wave sources.

Our group continued the work on SHG with large walkoff. In Ref. [22], we studied the temperature rise in $KNbO_3$ SHG and its effect on the phase matching condition, which must be accounted for to optimize the conversion efficiency. In Ref. [23], we studied the SHG in periodically poled lithium niobate (PPLN) waveguides. We found a strong efficiency saturation at about 60%. Simulations indicate that a large nonlinear phase modulation (NPM) may account for the saturation, and the source of the NPM is most likely to be a cascaded SHG process involving a higher-order spatial mode of the SH field in the waveguide.

SHG in thick crystals were also studied by other groups at the same time. In Ref. [21,24], non-critical phase matching SHG in a 10mm $KNbO_3$ crystal was studied. They measured the SHG efficiency and beam quality as a function of the crystal position relative to the focusing lens [24], and found that the optimal distance becomes larger under higher input powers. They also compared the SHG behavior with a 2ps laser source and a 120fs source [21]. They observed that they yield similar efficiencies as we mentioned, and they both have efficiency saturation and decline under high powers. But the difference is that the 2ps source has an oscillatory decline of efficiency, while the 120fs source has a smoother and slower decline. They explained this phenomenon with strong depletion and pump phase modulation in the SHG process.

The temperature rise, efficiency saturation and decline in $KNbO_3$ is mainly due to the blue-induced IR absorption [25], which doesn't affect the crystals we are going to study: BBO and LBO.

1.3 Our Research

Our research objective is to study type I SHG in long crystals using focused femtosecond laser sources, where the temporal walkoff, spatial walkoff and pump depletion are all important. While trying to achieve efficiency as high as possible in our bulk crystals, we also want to reveal the relationship between the conversion efficiency and the input parameters of the SHG process.

Here we present a theory which for the first time can give analytical predictions of type I SHG efficiency for short pulse sources with simultaneous focusing, spatial walkoff and temporal walkoff. Within the nondepleted pump approximation, our theory may be considered as an extension of Boyd & Kleinman's theory [13] to include both space and time coordinates. However, our theory is valid not only for a nondepleted pump as Boyd & Kleinman's theory [13], but is also approximately valid well into the depleted pump regime.

In order to validate our theory, we will first compare our theory with a SHG numerical model. Numerical models only need basic differential equations to work in many cases, can give very accurate results and can be very versatile. Analytical models always have some limitations because for a complicated process, approximations have to be made to derive an understandable analytical result. But analytical models have the advantage of providing greater insight, revealing the relationship between the parameters and predicting scaling rules.

We will also compare the theoretical predictions with experimental results. We performed experiments in which we measured the SHG efficiency in two nonlinear crystals (BBO and LBO) under different focusing conditions and different input

powers. The experiments are performed under conditions when both spatial and temporal walkoffs are important and with a conversion efficiency as high as 60%.

The remainder of Part I of the thesis is structured as follows. Our theory of type I SHG with pulsed sources is derived in Chapter 2. Chapter 3 discusses how to evaluate the efficiency numerically using the theoretical equations and displays some theoretical results which shows how the efficiency changes with different parameters. Chapter 4 compares the results of theoretical models (ours and Boyd&Kleinman's [13]) with those of the nonlinear optics solver SNLO from Sandia National Laboratories [26, 27]. Experimental results are presented and compared with the theory in Chapter 5. Chapter 6 is the conclusion of our type I SHG study.

2. TYPE I SHG THEORY

2.1 Deriving the Output Second Harmonic Field

2.1.1 Formal Approach

Here we will derive the second harmonic field at the output end of the nonlinear crystal in ooe type I SHG with no pump depletion (or equivalently, low efficiency)using formal electromagnetics theory. First we review some results from Boyd & Kleinman's theory [10–12] for CW sources and ooe type I SHG. We then show how to extend to the case of pulse sources. We will use the same notation here as in [10–13], i.e. Gaussian units and $e^{-i\omega t}$ convention. At the end of this section we will convert from Gaussian units to MKS units and make a complex conjugate transformation in order to switch to the $e^{+i\omega t}$ convention.

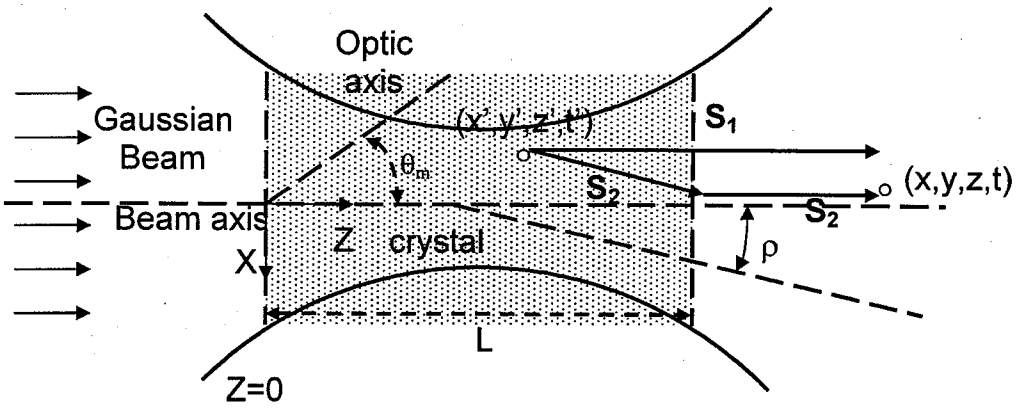

Fig. 2.1. A picture of ooe SHG

Fig. 2.1 is a simple picture of the ooe SHG process we are studying. The input fundamental field (o-wave) propagates along the Z axis and has a Gaussian spatial

profile. Both the wave vector $\vec{k}_1$ and the Poynting vector $\vec{S}_1$ of the fundamental field are along the Z axis. The nonlinear crystal has the length L, and its cross-section is much larger than the input laser beam. z=0 is the input surface and z=L is the output end. We ignore any reflections at the crystal surfaces. The beam axis is normal to the crystal surface. The optic axis is taken to lie in the XZ plane. θ_m is the phase-matching angle. For ooe SHG, the polarization of the input field is taken along Y, and the output SH field is polarized along X. In this paper we will write the fields in scalar form, since we already assumed that they are linearly polarized and we know their polarization. The wave vector of the SH wave $\vec{k}_2$ is also along the Z axis, but the Poynting vector of it $\vec{S}_2$ deviates from the Z axis by the spatial walkoff angle ρ in the XZ plane. In the figure (x', y', z', t') represents a source point of the SH wave in the crystal, and (x, y, z, t) represents an observer point outside the crystal.

In our theory we consider group velocity mismatch between fundamental and second harmonic fields but ignore the fundamental pulse broadening due to material dispersion (or equivalently, ignore the group velocity dispersion (GVD)). This is justified in our experiments, in which we studied SHG of 120fs pulses in an 8mm-long BBO crystal and in a 15mm-long LBO crystal. In both cases broadening of the fundamental pulse due to material dispersion is calculated to be only a few femtoseconds. If much shorter pulses were used for SHG, the effect of GVD would eventually become important. We also neglect any material absorption in the nonlinear crystal.

The SHG theory is based upon the inhomogeneous vector wave equation (in Gaussian units):

$$\nabla \times \nabla \times \vec{E}_2(\vec{r}, \omega) - (\omega/c)^2 \vec{\vec{\epsilon}}_2 \bullet \vec{E}_2(\vec{r}, \omega) = 4\pi(\omega/c)^2 \vec{P}_{NL}(\vec{K}, \omega) e^{i\vec{K}\bullet\vec{r}} \qquad (2.1)$$

Here $\vec{\vec{\epsilon}}_2$ is the dielectric constant tensor at frequency ω. The subscript '2' means second harmonic field. $\vec{P}_{NL}(\vec{K}, \omega)$ is the complex amplitude of the nonlinear plane-wave polarization field at frequency ω and with an arbitrary wave vector $\vec{K}$. The solution of equation 2.1 consists of a forced wave and suitable free waves. The free

waves are chosen to satisfy the boundary conditions of the problem, which in our case is that there is no SH field at the incident plane of the crystal.

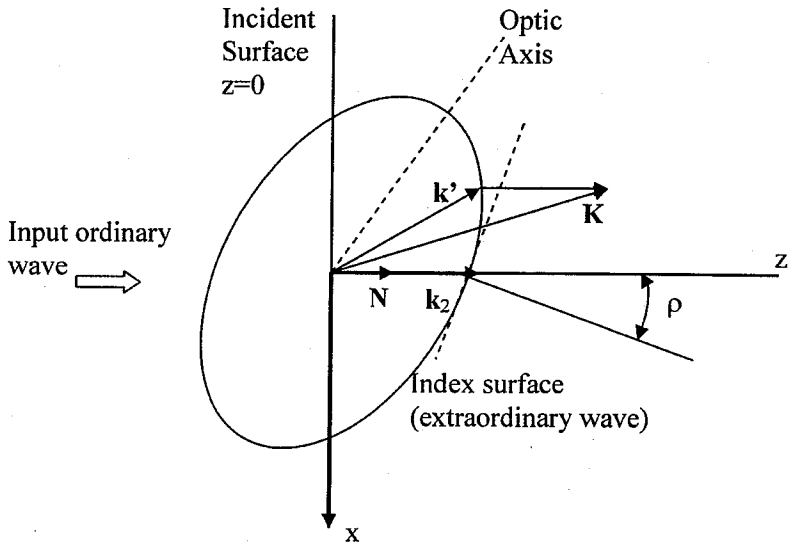

Fig. 2.2. The index surface and the vector mismatch relationship

In Fig. 2.2, we show the elliptical index surface [10] of the SH wave (e wave). The wave vector of the fundamental wave and harmonic wave ($\vec{k}_1$ and $\vec{k}_2$) are both along the z axis, and $\vec{N}$ is the unit vector along z. The walk-off angle ρ is the angle between z axis and the normal to the index surface. $\vec{k}'$ is a vector on the index surface such that $\vec{K} - \vec{k}'$ is parallel to z axis. Ref. [10] shows that without absorption, under nearly matching conditions the growing wave is given by:

$$\vec{E}_2(\vec{r},\omega) = z \cdot g(2i\Psi_K)\vec{\vec{\gamma}} \bullet \vec{P}_{NL}(\vec{K})e^{i\vec{K}\bullet\vec{r}} \tag{2.2}$$

where:

$$\vec{\vec{\gamma}} = 2\pi i(\omega/cn)\vec{U}\vec{U} \tag{2.3}$$

$$2\Psi_K = (\vec{K} - \vec{k}') \bullet \vec{N}z \tag{2.4}$$

$$g(x) = (1 - e^{-x})/x = \int_0^1 e^{-xp}dp \tag{2.5}$$

Here $\vec{U}$ is a unit vector giving the polarization direction of the extraordinary harmonic wave, and n is the matched index. In our experiments $k_2 L$ is over 10^4, so nearly matching condition can still be applied when ΔkL reaches 100. In Equation 2.4 we need the z component of $\vec{K} - \vec{k'}$. To the second order terms of K_x and K_y, we have [11]:

$$2\Psi_K = (K_z - k_2 + \rho K_x + \frac{K_x^2 + K_y^2}{2k_2})z \tag{2.6}$$

The detailed derivation of Equation 2.6 can be found in the appendix. Generally the nonlinear polarization field is not plane-wave, and we will use Fourier transformation to get an integral result:

$$\vec{P}_{NL}(\vec{K}) = (2\pi)^{-3} \int \vec{P}_{NL}(\vec{r'}) e^{-i\vec{K}\bullet\vec{r'}} d\vec{r'} \tag{2.7}$$

$$\vec{E}_2(\vec{r}) = z \int g(2i\Psi_K) \vec{\vec{\gamma}} \bullet \vec{P}_{NL}(\vec{K}) e^{i\vec{K}\bullet\vec{r}} d\vec{K} \tag{2.8}$$

Equation 2.8 comes from Equation 2.2. We can substitute Equation 2.7 into 2.8, and exchange the order of integration. Then we can get an equation in the form:

$$\vec{E}_2(\vec{r}) = \int \vec{\vec{\gamma}} \bullet \vec{P}_{NL}(\vec{r'}) G(\vec{r}, \vec{r'}) d\vec{r'} \tag{2.9}$$

$\vec{r'}$ represents the source point, and $\vec{r}$ represents the observer point. G is called the interior Green's function (since it works when the observer point is inside the crystal). Without absorption the result is [12]:

$$G_\omega(\vec{r}, \vec{r'}) = \frac{1}{2\pi i} \frac{k_2}{Z} e^{ik_2(Z + (X^2+Y^2)/2Z)} \tag{2.10}$$

We added the subscript ω since k_2 is a function of ω. In Equation 2.10:

$$X = x - x' - \rho(z - z') \tag{2.11}$$

$$Y = y - y' \tag{2.12}$$

$$Z = z - z' \geq 0 \tag{2.13}$$

As Ref. [12] shows, the important region is $X^2 + Y^2 << Z^2$. All parts of the wavelet which are not in this region destructively interfere and produce no resultant

field. Thus all the SH energy radiated at the source point flows along the direction of the SH Poynting vector. In this region we have:

$$R = Z + \frac{X^2 + Y^2}{2Z} \approx \sqrt{X^2 + Y^2 + Z^2} \tag{2.14}$$

Now let us consider the pulsed source case, which is our new contribution. We need to expand the above theory by letting $\vec{P}_{NL}$ have a distribution with respect to ω:

$$\vec{P}_{NL}(\vec{K}, \omega) = (2\pi)^{-4} \int \vec{P}_{NL}(\vec{r'}, t') e^{-i\vec{K}\bullet\vec{r'}} e^{i\omega t'} d\vec{r'} dt' \tag{2.15}$$

$$\vec{E}_2(\vec{r}, t) = z \int g(2i\Psi_K) \vec{\bar{\gamma}} \bullet \vec{P}_{NL}(\vec{K}, \omega) e^{i\vec{K}\bullet\vec{r}} e^{-i\omega t} d\vec{K} d\omega \tag{2.16}$$

The source points are $(\vec{r'}, t)$, and the observer points are $(\vec{r}, t)$. The definition of the Green's function then is:

$$\vec{E}_2(\vec{r}, t) = \int \vec{\bar{\gamma}} \bullet \vec{P}_{NL}(\vec{r'}, t') G(\vec{r}, \vec{r'}, t, t') d\vec{r'} dt' \tag{2.17}$$

Using Equation 2.7, 2.8, 2.9 and 2.15, 2.16, 2.17, one can easily derive:

$$G(\vec{r}, \vec{r'}, t, t') = \frac{1}{2\pi} \int G_\omega(\vec{r}, \vec{r'}) e^{-i\omega(t-t')} d\omega \tag{2.18}$$

Using Equation 2.10 and 2.18, we can derive the interior Green's function in the pulsed case:

$$G(\vec{r}, \vec{r'}, t, t') = \frac{1}{(2\pi)^2 i} \int \frac{k_2}{Z} e^{ik_2(Z + (X^2+Y^2)/2Z)} e^{-i\omega(t-t')} d\omega \tag{2.19}$$

To calculate the above integral we will need the following relationships:

$$k_2 = k_{20} + \frac{\partial k_2}{\partial \omega}(\omega - \omega_2) = k_{20} + \frac{1}{V_2}(\omega - \omega_2) \tag{2.20}$$

$$\int e^{-i\omega t} d\omega = 2\pi\delta(t) \tag{2.21}$$

$$\int \omega e^{-i\omega t} d\omega = 2\pi i \delta'(t) \tag{2.22}$$

Here V_2 is the group velocity of the SH wave, and ω_2 is the center frequency of the SH wave. The result of the calculation is:

$$G(\vec{r}, \vec{r'}, t, t') = \frac{1}{2\pi i Z} e^{ik_{20}R} e^{-i\omega_2(t-t')} [k_{20}\delta(t - t' - \frac{R}{V_2}) + \frac{i}{V_2}\delta'(t - t' - \frac{R}{V_2})] \tag{2.23}$$

We write the fields inside the nonlinear crystal as the following (using the same convention as in Ref. [10–13]:

$$E_1(x',y',z',t') = A_1(x',y',z',t')e^{-i(\omega_1 t' - k_1 z')} \tag{2.24}$$

$$E_2(x',y',z',t') = A_2(x',y',z',t')e^{-i(\omega_2 t' - k_2 z')} \tag{2.25}$$

$$P_{NL}(x',y',z',t') = P_2(x',y',z',t')e^{-i(2\omega_1 t' - 2k_1 z')} \tag{2.26}$$

Here we use E to represent the total field and A to represent the complex amplitude free of fast-oscillating terms. ω_1 is the center frequency of the fundamental wave, and k_1 is the wave vector of the fundamental wave inside the crystal at ω_1; $\omega_2 = 2\omega_1$ and k_2 is the wave vector at ω_2. For a CW source, A_1 is independent of t'. The nonlinear polarization field is excited by the fundamental field:

$$\begin{aligned} P_2 &= d_{eff}A_1^2, \ \textit{Gaussian units} \\ P_2 &= \epsilon_0 d_{eff}A_1^2, \ \textit{MKS units} \end{aligned} \tag{2.27}$$

Comparing Equation 2.27 with 1.3, we can see that there is a missing factor of 2. This is because P_{NL} and E_1 defined above are the complex representation of the fields, not the REAL fields. We will use Equation 1.3 to derive Equation 2.27 in the next subsection. For generality, we assume that the input fundamental wave is an elliptical Gaussian beam in space [28], and a linearly chirped Gaussian pulse in time:

$$\begin{aligned} A_1 = \frac{A_0}{\sqrt{(1+i\tau_x(z'))(1+i\tau_y(z'))}} \exp\left(-\frac{x'^2}{w_{0x}^2(1+i\tau_x(z'))}\right) \exp\left(-\frac{y'^2}{w_{0y}^2(1+i\tau_y(z'))}\right) \\ \exp\left(-\frac{2\ln 2(t'-z'/V_1)^2}{t_p^2}\right) \exp\left(i\frac{\alpha \ln 2(t'-z'/V_1)^2}{2t_p^2}\right) \end{aligned} \tag{2.28}$$

$$\tau_x(z') = 2(z'-z_{0x})/b_x \tag{2.29}$$

$$\tau_y(z') = 2(z'-z_{0y})/b_y \tag{2.30}$$

Some explanations of the above equations are as below:

A_0 is a constant. The spatial part of Equation 2.28 represents an elliptical Gaussian beam where w_{0x} and w_{0y} are the radii of the beam waist in the X and Y directions

respectively, and z_{0x} and z_{0y} are the positions of the beam waist for the X and Y directions respectively. The confocal parameters of the Gaussian beam for X and Y directions, which describe how divergent the beam is, are written as $b_x = 2\pi n_1 w_{0x}^2/\lambda_0$ and $b_y = 2\pi n_1 w_{0y}^2/\lambda_0$. We use n_1 and n_2 as the refractive indices of the fundamental and harmonic waves respectively. In Equation 2.28 $\tau_x()$ and $\tau_y()$ are two functions defined in Equations 2.29 and 2.30. They are the longitudinal distance from the source point to the beam waist normalized to the depth of focus.

In the temporal part of Equation 2.28, t_p is the FWHM duration of the pulse in terms of intensity. We assume that the input fundamental spectrum is Gaussian with a quadratic spectral phase: $\exp(-\omega^2 t_0^2/4)\exp(ip\omega^2)$ (t_0 and p are both constant). By Fourier transforming it into the time domain we will have the temporal part in equation 2.28 with $\alpha = 16p/t_0^2$ and $t_p = t_0\sqrt{1+\alpha^2}$. Obviously the phase term represents a linear chirp. The pulse has a time-bandwidth product $\Delta\nu\Delta t$ which is $\sqrt{1+\alpha^2}$ times greater than the time-bandwidth product of a chirp-free Gaussian pulse. Here we ignore higher order chirps. We also ignore GVD for the fundamental field as we mentioned. For the case of no source depletion the fundamental pulse will propagate at its group velocity with a fixed temporal profile.

With Equation 2.27 and 2.28, we can have:

$$\vec{P}_{NL}(\vec{r'},t') = \frac{\vec{P}_0 e^{2ik_1 z'} e^{-i\omega_2 t'} f(t')}{(1+i\tau_x(z'))(1+i\tau_y(z'))} \exp\left(-\frac{2x'^2}{w_{0x}^2(1+i\tau_x(z'))} - \frac{2y'^2}{w_{0y}^2(1+i\tau_y(z'))}\right) \tag{2.31}$$

$$f(t') = \exp\left(-\frac{4\alpha' \ln 2(t'-z'/V_1)^2}{t_p^2}\right) \tag{2.32}$$

Where $\alpha' = 1 - i\alpha/4$. α won't be much bigger than 1 unless the pulse is severely chirped. We can then substitute Equation 2.23 and 2.31 into Equation 2.17 to have:

$$\begin{aligned}\vec{E}_2(\vec{r},t) = \vec{\vec{\gamma}} \bullet \vec{P}_0 \frac{k_{20}}{2\pi i} e^{ik_{20}z} e^{-i\omega_2 t} \int \frac{e^{-i\Delta k z'}}{Z(1+i\tau_x(z'))(1+i\tau_y(z'))} dz' \\ \int\int [f(t-R/V_2) + \frac{i}{k_{20}V_2} f'(t-R/V_2)] \exp\left(i\frac{k_{20}(X^2+Y^2)}{2Z}\right) \\ \exp\left(-\frac{2x'^2}{w_{0x}^2(1+i\tau_x(z'))} - \frac{2y'^2}{w_{0y}^2(1+i\tau_y(z'))}\right) dx'dy'\end{aligned} \tag{2.33}$$

Note that R is a function of x', y' and z'. There are two facts that we can use to simplify the above equation. Using Equation 2.32 we can have:

$$f(t-R/V_2)+\frac{i}{k_{20}V_2}f'(t-R/V_2)=e^{-\frac{4\alpha'\ln 2(t-R/V_2-z'/V_1)^2}{t_p^2}}[1-\frac{i8\alpha'\ln 2}{k_{20}V_2t_p^2}(t-R/V_2-z'/V_1)] \tag{2.34}$$

Temporally the important region is $|t-R/V_2-z'/V_1|<\left|3t_p/\sqrt{4\alpha'\ln 2}\right|$. Outside this region the exponential term becomes very small and the contribution to the integral is negligible. In this important region we claim that $\left|\frac{8\alpha'\ln 2}{k_{20}V_2t_p^2}(t-R/V_2-z'/V_1)\right|<\left|\frac{12\sqrt{\alpha'\ln 2}}{k_{20}V_2t_p}\right|<<1$. For our experiments with 800nm fundamental wavelength and BBO or LBO crystal, $\left|\sqrt{\alpha'}\right|\approx 1.02$, $k_{20}^{-1}\approx 40nm$, $V_2^{-1}\approx 5000fs/mm$, $t_p\approx 100fs$, and calculation shows that $\left|\frac{12\sqrt{\alpha'\ln 2}}{k_{20}V_2t_p}\right|\approx 0.02<<1$. This means that the imaginary part in the middle bracket of Equation 2.34 can be practically ignored, and so the same with the $f'(t-R/V_2)$ term in Equation 2.33. This approximation is more accurate with longer input pulses (larger t_p), and may not be a good approximation for pulses as short as 10fs.

Also, from Equation 2.10 and 2.33, it is clear that R/V_2 describes the time needed for the SH wave packet to travel from the source point to the observer point. From Equation 2.11 and 2.12, X and Y describe the deviation of the wave packet propagation direction from the Poynting vector. As we mentioned above, spatially the important region is $X^2+Y^2<<Z^2$, which means that the wave packets propagate very closely to the Poynting vector direction. All wave packets propagating outside this region destructively interfere and give no contribution. In the important region we make the approximation that when calculating the traveling time of wave packets, we assume that energy propagates strictly along the direction of the Poynting vector. Mathematically it means that we use $R\approx Z$ and $f(t-R/V_2)\approx f(t-Z/V_2)$. With these approximations the temporal part in the integral of Equation 2.33 is de-coupled from x' and y'.

We then can calculate the integral over x' and y' in Equation 2.33 using the following formula [29]:

$$\int_{-\infty}^{+\infty} e^{-iax-ibx^2} dx = \sqrt{\frac{\pi}{ib}} e^{ia^2/4b}, Im(b) < 0 \tag{2.35}$$

The result is:

$$\vec{E}_2(\vec{r},t) = \frac{\vec{\vec{\gamma}} \bullet \vec{P}_0 e^{ik_{20}z} e^{-i\omega_2 t}}{\sqrt{(1+i\tau_x(z))(1+i\tau_y(z))}} \exp\left(-\frac{2y^2}{w_{0y}^2(1+i\tau_y(z))}\right) \int_0^z \frac{e^{-i\Delta kz'} \exp\left(-\frac{2(x-\rho Z)^2}{w_{0x}^2(1+i\tau_x(z))}\right) f(t-z/V_2+\beta z')}{\sqrt{(1+i\tau_x(z'))(1+i\tau_y(z'))}} dz' \tag{2.36}$$

By setting $z = L$, the above Equation can be used to calculate the SH field profile at the output end of the nonlinear crystal. To convert Equation 2.36 to MKS units, first we need to do a complex conjugate transformation. Then, in MKS units, $\vec{U} \bullet \vec{P}_0$ is $\epsilon_0 d_{eff} A_0^2$ from Equation 2.27. The $4\pi/c^2$ in $\vec{\vec{\gamma}}$ (Equation 2.3) should be replaced by μ_0 [30]. After the conversion we will then have:

$$A_2(x,y,L,t) = -i\frac{\kappa A_0^2}{\sqrt{(1-i\tau_x(L))(1-i\tau_y(L))}} \exp\left(-\frac{2y^2}{w_{0y}^2(1-i\tau_y(L))}\right) \int_0^L \frac{e^{-i\Delta kz'} \exp\left(-\frac{2(x-\rho L+\rho z')^2}{w_{0x}^2(1-i\tau_x(L))}\right) \exp\left(-\frac{(4+i\alpha)\ln 2(t-L/V_2+\beta z')^2}{t_p^2}\right)}{\sqrt{(1-i\tau_x(z'))(1-i\tau_y(z'))}} dz' \tag{2.37}$$

Where $\kappa = \omega_1 d_{eff}/n_2 c$ is the same coefficient defined in the line following Equation 1.5. The above equation is the basis of the derivation of the SHG efficiency.

2.1.2 Heuristic approach

Here we will derive Equation 2.37 using a heuristic approach similar as in [13]. The heuristic approach is not as strict as the formal approach but it's both straightforward and insightful. In the end, it will yield the same result as the formal approach. From now on we always use MKS units and the $e^{+i\omega t}$ convention.

The basic idea is that the SH field outside the crystal is the integral of the contributions from all the sources inside the crystal. We redefine the fields inside the nonlinear crystal as the following:

$$E_1(x',y',z',t') = \frac{1}{2}(A_1(x',y',z',t')e^{i(\omega_1 t' - k_1 z')} + c.c) \tag{2.38}$$

$$E_2(x',y',z',t') = \frac{1}{2}(A_2(x',y',z',t')e^{i(\omega_2 t' - k_2 z')} + c.c) \tag{2.39}$$

$$P_{NL}(x',y',z',t') = \frac{1}{2}(P_2(x',y',z',t')e^{i(2\omega_1 t' - 2k_1 z')} + c.c) \tag{2.40}$$

E_1, E_2 and P_{NL} defined above are real fields. We can use Equation 1.3 to get:

$$P_{NL} = 2\epsilon_0 d_{eff} E_1^2 = \frac{\epsilon_0 d_{eff}}{2}(A_1^2(x',y',z',t')e^{2i(\omega_1 t' - k_1 z')} + c.c) \tag{2.41}$$

In the above equation we omitted the DC component of E_1^2. Comparing Equation 2.41 with 2.40, we have:

$$P_2 = \epsilon_0 d_{eff} A_1^2 \tag{2.42}$$

This is the same as Equation 2.27. Considering a CW plane-wave source, it can be shown that the harmonic field amplitude at the output end of the crystal ($z = L$) is (see Equation (3.7) in Ref. [11]):

$$\begin{aligned} A_2(L) &= -\frac{i\omega_2 \mu_0 c}{2n_2}\int_0^L P_2(z')\exp(i\Delta k z')dz' \\ &= -i\kappa\int_0^L A_1^2(z')\exp(i\Delta k z')dz' \end{aligned} \tag{2.43}$$

where n_2 is the refractive index of the SH wave and $\Delta k = k_2 - 2k_1$ is the phase mismatch. Equation 2.43 is valid for CW plane waves. For pulsed Gaussian beam input, things are much more complicated. Here we use an approach, which we term the extended heuristic approach, to derive it.

As we described in the previous section, in Boyd&Kleinman's theory [12] a Green's function was derived for continuous-wave SHG by an arbitrary polarization; the total SH field was obtained by integrating this Green's function over a Gaussian beam. It was shown that the Green's function has the property that energy propagates from the source point to the observer point along the direction of

Poynting vector, as in Fig. 2.1. This means that for a certain observer point, the source points that contribute must lie on the same ray. This method, termed the heuristic approach in Ref. [13], allows us to set up a relationship between the spatial coordinates of source points and the observer point. Because in our case we use pulses instead of a CW source, we have an extra coordinate in the time domain. Therefore, here we extend the heuristic approach to include a short pulse source by assuming that energy propagates from the source point to the observer point both along the ray and at the group velocity. This is justified by comparing the result derived here using the extended heuristic approach, with the formal results derived in the previous secion.

The heuristic approach results in:

$$\begin{aligned} x' &= x - \rho(L - z') = x - \rho L + \rho z' \\ y' &= y \\ t' &= t - (L - z')/V_2 \end{aligned} \tag{2.44}$$

Because the Poynting vector and the wave vector are in different directions for the SH wave, V_2 is not the total energy-flow velocity, but is rather its Z component (in the wave vector direction).

Since Equation 2.43 is valid for CW plane waves, it should also be valid for CW waves which are nearly plane waves except for being finite in the X, Y directions. To include the case that the source is pulsed but the waveform doesn't change in the whole process (ignoring GVD), we just add a temporal coordinate and relate the source points and the observer point with Equation 2.44. By using the extended heuristic approach we can extend Equation 2.43 to get:

$$\begin{aligned} A_2(x, y, L, t) &= -i\kappa \int_0^L A_1^2(x', y', z', t') \exp(i\Delta k z') dz' \\ &= -i\kappa \int_0^L A_1^2(x - \rho L + \rho z', y, z', t - (L - z')/V_2) \exp(i\Delta k z') dz' \end{aligned} \tag{2.45}$$

Since a focused Gaussian beam is not a nearly plane wave, the field propagation from the source points to the observer point must be taken into account. However,

based on Equation 2.45 we can still write down the incremental harmonic field at the source point (before propagation):

$$dA_2(x',y',z',t') = -i\kappa A_1^2(x',y',z',t')\exp(i\Delta k z')dz' \tag{2.46}$$

By properly dealing with field propagation and using the heuristic approach, we will be able to derive $dA_2(x,y,L,t)$ from $dA_2(x',y',z',t')$ and get an integral for $A_2(x,y,L,t)$. How exactly it is done for Gaussian beam will be shown below.

The complex amplitude of the fundamental field is written as [28]:

$$A_1 = \frac{A_0}{\sqrt{(1-i\tau_x(z'))(1-i\tau_y(z'))}}\exp(-\frac{x'^2}{w_{0x}^2(1-i\tau_x(z'))})\exp(-\frac{y'^2}{w_{0y}^2(1-i\tau_y(z'))})$$
$$\exp(-\frac{2\ln 2(t'-z'/V_1)^2}{t_p^2})\exp(-i\frac{\alpha\ln 2(t'-z'/V_1)^2}{2t_p^2}) \tag{2.47}$$

This is just the complex conjugate of Equation 2.28. By using Equation 2.46 we have the incremental harmonic amplitude at the source point:

$$dA_2(x',y',z',t') = \frac{-i\kappa A_0^2\exp(i\Delta k z')}{\sqrt{(1-i\tau_x(z'))(1-i\tau_y(z'))}}\exp(-\frac{(4+i\alpha)\ln 2(t'-z'/V_1)^2}{t_p^2})$$
$$\left[\frac{1}{\sqrt{(1-i\tau_x(z'))(1-i\tau_y(z'))}}\exp(-\frac{2x'^2}{w_{0x}^2(1-i\tau_x(z'))})\exp(-\frac{2y'^2}{w_{0y}^2(1-i\tau_y(z'))})\right]dz' \tag{2.48}$$

To deal with field propagation we need to notice that the part enclosed in the brackets has the form of the amplitude of a Gaussian beam of spot size $w_{0x}/\sqrt{2}$ and $w_{0y}/\sqrt{2}$, the same confocal parameter b_x and b_y as the incident beam, and beam waist position z_{0x} and z_{0y}. It is this part which propagates, because it is known as a solution of the wave equation in the paraxial approximation. These conditions have been assumed by several authors (Ref. [8] Page 94, [13, 31, 32])where the aim was to find the optimal focusing conditions for nonlinear interactions with CW or quasi-CW waves. After the SH field propagates from (x',y',z',t') to (x,y,L,t) we replace $\tau_x(z')$, $\tau_y(z')$ by $\tau_x(L)$, $\tau_y(L)$ in the brackets, and use the extended heuristic

approach (Equation 2.44). Let the observer point be right at the output end of the crystal ($z = L$), the incremental harmonic amplitude at the observer point is:

$$dA_2(x,y,L,t) = \frac{-i\kappa A_0^2 \exp(i\Delta k z') \exp(-\frac{2y^2}{w_{0y}^2(1-i\tau_y(L))})}{\sqrt{(1-i\tau_x(L))(1-i\tau_y(L))(1-i\tau_x(z'))(1-i\tau_y(z'))}}$$
$$\exp(-\frac{2(x-\rho L+\rho z')^2}{w_{0x}^2(1-i\tau_x(L))}) \exp(-\frac{(4+i\alpha)\ln 2(t-L/V_2+\beta z')^2}{t_p^2})dz' \qquad (2.49)$$

The harmonic field can be written as an integral over z':

$$A_2(x,y,L,t) = \frac{-i\kappa A_0^2}{\sqrt{(1-i\tau_x(L))(1-i\tau_y(L))}} \exp(-\frac{2y^2}{w_{0y}^2(1-i\tau_y(L))})$$
$$\int_0^L \frac{\exp(i\Delta k z')}{\sqrt{(1-i\tau_x(z'))(1-i\tau_y(z'))}} \exp(-\frac{2(x-\rho L+\rho z')^2}{w_{0x}^2(1-i\tau_x(L))})$$
$$\exp(-\frac{(4+i\alpha)\ln 2(t-L/V_2+\beta z')^2}{t_p^2})dz' \qquad (2.50)$$

We can see Equation 2.50 is the same as Equation 2.37. Thus we have finished deriving the output SH field at the output end of the crystal using both the formal approach and the heuristic approach.

2.2 Type I SHG Conversion Efficiency

2.2.1 Efficiency with no pump depletion

Since we have the output SH field in the case of no pump depletion (low efficiency limit), we can also calculate the conversion efficiency in this case. We need to multiply $A_2(x,y,L,t)$ with its complex conjugate to get $|A_2|^2$, and integrate it over x, y and t to get the pulse energy. From Equation 2.50, $|A_2|^2$ can be written as a double integral. After some transformations using simple algebra we can get the equations below:

$$|A_2|^2 = \frac{\kappa^2 |A_0|^4}{\sqrt{(1+\tau_x^2(L))(1+\tau_y^2(L))}} \exp(-\frac{4y^2}{w_{0y}^2(1+\tau_y^2(L))})$$
$$\int_0^L \int_0^L \frac{\exp(i\Delta k(z_1-z_2)) \exp(-\frac{(z_1-z_2)^2}{l_{s-T}^2})}{\sqrt{(1-i\tau_x(z_1))(1-i\tau_y(z_1))(1+i\tau_x(z_2))(1+i\tau_y(z_2))}}$$

$$\exp\left(-\frac{4x_{12}^2}{w_{0x}^2(1+\tau_x^2(L))}\right)\exp\left(-\frac{8\ln 2 t_{12}^2}{t_p^2}\right)dz_1dz_2 \tag{2.51}$$

$$x_{12} = x - \rho L + \rho\frac{z_1+z_2}{2} + \frac{i\tau_x(L)\rho(z_1-z_2)}{2} \tag{2.52}$$

$$t_{12} = t - L/V_2 + \beta\frac{z_1+z_2}{2} - \frac{i\alpha\beta(z_1-z_2)}{8} \tag{2.53}$$

$$l_{S-T} = \left[\frac{\rho^2}{w_{0x}^2} + \frac{(\alpha^2+16)\beta^2\ln 2}{8t_p^2}\right]^{-\frac{1}{2}} = \left[l_S^{-2} + (\frac{\alpha^2}{8}+2)\ln 2 l_T^{-2}\right]^{-\frac{1}{2}} \tag{2.54}$$

Defined by Equation 2.54, l_{S-T} is what we call the generalized space-time walkoff length. l_S is the spatial walkoff length defined in Equation 1.8, and l_T is the temporal walkoff length defined in Equation 1.6. In an SHG process with pulse sources, normally both temporal walkoff and spatial walkoff exist. As shown in Equation 2.54, the generalized walkoff length l_{S-T} represents a combination of both walkoff effects. It plays an important role in determining the conversion efficiency, as we will see in the equations later. The pulse energy U_2 of the harmonic wave can be acquired by an integral of field intensity over time and over the XY plane at $z = L$:

$$U_2 = \frac{1}{2}\epsilon_0 c n_2 \int_{-\infty}^{\infty}dx\int_{-\infty}^{\infty}dy\int_{-\infty}^{\infty}dt\,|A_2(x,y,L,t)|^2 \tag{2.55}$$

Mathematically it can be proven that $\int_{-\infty}^{\infty}\exp\left(-\frac{(x+C)^2}{a^2}\right)dx = \sqrt{\pi}\,|a|$ when a is real and C is any complex constant inside the integral. We can then substitute Equation 2.51 into 2.55 and the integrals of x, y and t parts are all simple Gaussian integrals. The formula for U_2 is:

$$\begin{aligned} U_2 = {} & \epsilon_0 c n_2 \frac{\pi^{\frac{3}{2}}\kappa^2|A_0|^4}{16\sqrt{2\ln 2}} w_{0x}w_{0y}t_p \\ & \int_0^L\int_0^L \frac{\exp\left(i\Delta k(z_1-z_2)\right)\exp\left(-(z_1-z_2)^2/l_{S-T}^2\right)dz_1dz_2}{\sqrt{(1-i\tau_x(z_1))(1-i\tau_y(z_1))(1+i\tau_x(z_2))(1+i\tau_y(z_2))}} \end{aligned} \tag{2.56}$$

The fundamental pulse energy can be calculated from Equation 2.47:

$$U_1(0) = \epsilon_0 c n_1 |A_0|^2 \frac{\pi^{\frac{3}{2}}}{8\sqrt{2\ln 2}} w_{0x}w_{0y}t_p \tag{2.57}$$

This is the energy of the input pulse, which remains constant throughout the SHG process as long as we assume no pump depletion. From Equation 2.57 and 2.56 we have the conversion efficiency in the case of no source depletion:

$$\eta = \frac{U_2}{U_1} = \sqrt{\frac{2\ln 2}{\pi}} \frac{\gamma}{\sqrt{b_x b_y}} \frac{U_1}{t_p} \int_0^L \int_0^L \frac{\exp\left(i\Delta k(z_1 - z_2)\right) \exp\left(-(z_1 - z_2)^2 / l_{S-T}^2\right) dz_1 dz_2}{\sqrt{(1 - i\tau_x(z_1))(1 - i\tau_y(z_1))(1 + i\tau_x(z_2))(1 + i\tau_y(z_2))}} \tag{2.58}$$

$\gamma = \frac{\omega_2^2 d_{eff}^2}{n_1 n_2 \lambda_0 c^3 \epsilon_0}$ is the coupling coefficient we defined following Equation 1.9. We call this method to calculate the efficiency "the double-integral method" or "the full method" (in comparison with the asymptotic method we will intoduce later).

To compare our result with Boyd&Kleinman's theory (Equation 1.9), we need to reduce Equation 2.58 to the case of CW source and round Gaussian beam. For a round Gaussian beam we have $b_x = b_y = b$, $z_{0x} = z_{0y} = z_0$ and $\tau_x(z') = \tau_y(z') = \tau(z') = 2(z' - z_0)/b$, and so Equation 2.58 reduces to:

$$\eta = \sqrt{\frac{2\ln 2}{\pi}} \frac{\gamma}{b} \frac{U_1}{t_p} \int_0^L \int_0^L \frac{\exp\left(i\Delta k(z_1 - z_2)\right) \exp\left(-(z_1 - z_2)^2 / l_{S-T}^2\right) dz_1 dz_2}{(1 - i\tau(z_1))(1 + i\tau(z_2))} \tag{2.59}$$

To reduce from Gaussian pulses to the CW case we need to define an effective average power for a single input pulse. First we define an effective pulse duration:

$$\Delta t_{eff} = \frac{\left[\int dt I(t)\right]^2}{\int I^2(t)} \tag{2.60}$$

The physical significance of Δt_{eff} is: the generated second harmonic energy by the Gaussian input pulse is the same as that which would be generated by a square input pulse with duration Δt_{eff} at peak power $P_\omega = U_1 / \Delta t_{eff}$. For Gaussian pulses, we have from Equation 2.47:

$$\Delta t_{eff} = \sqrt{\frac{\pi}{2\ln 2}} t_p \tag{2.61}$$

$$P_\omega = \sqrt{\frac{2\ln 2}{\pi}} \frac{U_1}{t_p} \tag{2.62}$$

P_ω is then the effective average power for a Gaussian pulse. For CW sources there is no temporal walkoff, which means $l_T = \infty$ and $l_{S-T} = l_S$. Equation 2.59 becomes:

$$\eta = \frac{\gamma}{b} P_\omega \int_0^L \int_0^L \frac{\exp\left(i\Delta k(z_1 - z_2)\right) \exp\left(-(z_1 - z_2)^2/l_S^2\right) dz_1 dz_2}{(1 - i\tau(z_1))(1 + i\tau(z_2))} \tag{2.63}$$

We can see that Equation 2.63 is exactly the same as Equation 1.9. This proves that our theory reduces to Boyd&Kleinman's theory [13] for CW round Gaussian beams.

In Equation 2.58, normally the double integral can only be calculated numerically, but in the special case of $\Delta k = 0$ (phase matching condition) and $l_{S-T} << L << b_x \& b_y$ (strong walk-off and weak focusing), it can be calculated analytically. In that case the laser beam size is almost constant through the crystal, which means that $\tau_x(z)$ and $\tau_y(z)$ are both constant for $0 < z < L$. In Equation 2.58 we then have $\tau_x(z_1) = \tau_x(z_2) = \tau_x$, $\tau_y(z_1) = \tau_y(z_2) = \tau_y$, where τ_x and τ_y are both constants only depending on the offset of the beam waist from the center of the crystal. Hence they are constant for the integral. The double integral then only has a Gaussian term and it can be calculated when $l_{S-T} << L$. The result is:

$$\eta = \frac{U_2}{U_1} = \sqrt{2\ln 2} \frac{\gamma U_1}{t_p} \frac{l_{S-T} L}{\sqrt{b_x b_y (1 + \tau_x^2)(1 + \tau_y^2)}} \tag{2.64}$$

Note that in this case the harmonic pulse energy or efficiency is a linear function of crystal length. We can use this result to obtain a solution for arbitrary focusing (weak focusing not required) as long as the strong walk-off condition is maintained. When $l_{S-T} << b_x \& b_y$ and $l_{S-T} << L$, we can divide the crystal into small sections with length Δl ($l_{S-T} << \Delta l << b_x \& b_y$), use Equation 2.64 for the harmonic energy generated in each section, and add them up to get the total output energy. The result can be written as a 1-D integral:

$$\eta_a = \frac{U_2}{U_1} = \sqrt{2\ln 2} \frac{\gamma U_1}{t_p} l_{S-T} \int_0^L \frac{dz}{\sqrt{b_x b_y (1 + \tau_x^2(z))(1 + \tau_y^2(z))}} \tag{2.65}$$

We call this "the asymptotic method", which is why we use the subscript 'a'. When the fundamental beam is round, we have $w_{0x} = w_{0y} = w_0$, $b_x = b_y = b$,

$z_{0x} = z_{0y} = z_0$, $\tau_x(z) = \tau_y(z) = \tau(z) = 2(z - z_0)/b$. The integral can be calculated easily:

$$\eta_a = \frac{U_2}{U_1} = \sqrt{2\ln 2}\frac{\gamma U_1 l_{S-T}}{2t_p}\left[\arctan(\frac{2(L-z_0)}{b}) - \arctan(\frac{-2z_0}{b})\right] \tag{2.66}$$

For a round Gaussian input with no depletion, the best conversion efficiency occurs when the beam waist is at the crystal center ($z_0 = L/2$). Use this condition in Equation 2.66, we get:

$$\eta_{amax} = \frac{U_2}{U_1} = \sqrt{2\ln 2}\frac{\gamma U_1 l_{S-T}}{t_p}\arctan(\frac{L}{b}) \tag{2.67}$$

Note that l_{S-T} and b both change with the beam waist size (focusing condition), unless there is no spatial walk-off (non-critical phase matching). In the special case of no spatial walk-off ($l_S = \infty$), from Equation 2.54 we have $l_{S-T} = l_T/\sqrt{2\ln 2}$, and so Equation 2.67 becomes:

$$\eta_{amax} = \frac{U_2}{U_1} = \frac{\gamma U_1 l_T}{t_p}\arctan(\frac{L}{b}) \tag{2.68}$$

We can see that this equation is the same as Equation 1.10. This means that for round beams with no spatial walkoff, the asympotic method here reduces to Weiner&Kan'an's theory in 1998.

Equation 2.68 indicates that in the case of round Gaussian beam input and no spatial walkoff, the efficiency increases monotonically with tighter focusing and approaches an upper limit. However, this is not true if we calculate the efficiency using the full method. According to the full method, the efficiency will still drop if the focusing becomes tighter than an optimal value. We will come back to this difference in the next chapter.

2.2.2 Our treatment of efficiency including pump depletion

We have derived the formula for the type I SHG efficiency under the no source depletion approximation. We already have a relationship between the harmonic pulse

energy, fundamental pulse energy and the crystal length in that region, which we can write in the following form:

$$U_2 = U_1^2 F(L) \tag{2.69}$$

$F(L)$ is a function of crystal length L. The function is also related to the laser field profile and material properties. In our theory $F(L)$ is just the right side of Equation 2.58 without U_1^2. From Equation 2.69 we can derive a differential relationship:

$$\frac{dU_2}{dz} = U_1^2 F'(z) \tag{2.70}$$

Here $F'(z)$ is derivative of $F(z)$ with respect to z, and U_1 is a constant due to the no depletion approximation. It shows that the increasing rate of the harmonic energy over a small segment of crystal is proportional to the square of fundamental pulse energy and $F'(z)$. Physically $F'(z)$ should be determined by the field boundary conditions (field spatial and temporal profile on the boundaries) of each dz slab we are studying. Equation 2.70 was derived from the no pump depletion case. However, we can approximately treat pump depletion if we assume Equation 2.70 remains unchanged with the same $F'(z)$ as in the no-source-depletion approximation. This is equivalent to ignoring the change of boundary conditions for the dz slab when there is source depletion, which includes the nonlinear reshaping of the fundamental spatial and temporal field profile and the co-existence of the harmonic field with the fundamental field at the slab boundary. The strong walkoff in our experiments can separate the fundamental field and the generated harmonic field, which may improve the validity of this approximation relative to the weak walkoff case. One might expect this approximation to fail under very heavy pump depletion, since the nonlinear process will deplete the stronger part of the fundamental field more than the weaker part and reshape the field profile. We will discuss how well this approximation works with increasing pump depletion in the later chapters when we compare our theory with a numerical model and experimental results.

With this approximation we use the following coupled equations to deal with pump depletion:

$$\begin{aligned} \frac{dU_2}{dz} &= U_1^2 F'(z) \\ \frac{dU_1}{dz} &= -\frac{dU_2}{dz} \end{aligned} \tag{2.71}$$

The first equation is the same as Equation 2.70 with the same $F'(z)$, but here U_1 is no longer a constant. The second equation comes from energy conservation. We can substitute the second equation into the first one and get a single differential equation of $U_1(z)$:

$$\frac{1}{U_1^2}\frac{dU_1}{dz} = -F'(z) \tag{2.72}$$

Both sides can be easily integrated and we have the output fundamental pulse energy at $z = L$:

$$\frac{1}{U_1(L)} - \frac{1}{U_1(0)} = F(L) \tag{2.73}$$

From energy conservation $U_2(L) = U_1(0) - U_1(L)$, so the conversion efficiency after a crystal of length L is:

$$\begin{aligned} \eta = \frac{U_2(L)}{U_1(0)} &= 1 - \frac{1}{1 + U_1(0)F(L)} = 1 - \frac{1}{1+\eta_{nd}} \\ \Rightarrow \frac{1}{1-\eta} &= 1 + \eta_{nd} \end{aligned} \tag{2.74}$$

η now is the efficiency including source depletion. $U_1(0)$ is the input fundamental pulse energy. $U_1(0)F(L)$ is the efficiency we would get if assuming no source depletion, and we can call it η_{nd}. η_{nd} corresponds to the equations we derived in the previous section. Normally when we work in the depletion region, if we try to calculate the efficiency assuming no source depletion, we will get a result over 100%, which is physically meaningless. Equation 2.74 always gives a conversion efficiency between 0 and 1. When η or $\eta_{nd} << 1$, we will have $\eta = \eta_{nd}$, which means that SHG is in the non-depletion region and our results in the previous section can be used directly. Note that in Equation 2.74, η increases monotonically with η_{nd}. This means that in this theory the optimal SHG condition (focusing, phase mismatch,

etc.) is the same whether source depletion is considered or not. For example, for a round beam where the beam waist position is the same for X and Y directions, the optimal beam waist position always remains at the crystal center with or without pump depletion in this theory. The issue of the optimal beam waist position with pump depletion will be further discussed in the later chapters.

Under this same approximation, we can now easily transform formulas derived in the non-depletion region for use in the depletion region. From Equation 2.58, the full method for type I SHG efficiency including pump depletion will be:

$$\frac{1}{1-\eta} = 1 + \sqrt{\frac{2\ln 2}{\pi}} \frac{\gamma}{\sqrt{b_x b_y}} \frac{U_1}{t_p} \int_0^L \int_0^L \frac{\exp\left(i\Delta k(z_1 - z_2)\right) \exp\left(-(z_1 - z_2)^2 / l_{S-T}^2\right) dz_1 dz_2}{\sqrt{(1 - i\tau_x(z_1))(1 - i\tau_y(z_1))(1 + i\tau_x(z_2))(1 + i\tau_y(z_2))}} \tag{2.75}$$

The full method for round beam inputs is:

$$\frac{1}{1-\eta} = 1 + \sqrt{\frac{2\ln 2}{\pi}} \frac{\gamma}{b} \frac{U_1}{t_p} \int_0^L \int_0^L \frac{\exp\left(i\Delta k(z_1 - z_2)\right) \exp\left(-(z_1 - z_2)^2 / l_{S-T}^2\right) dz_1 dz_2}{(1 - i\tau(z_1))(1 + i\tau(z_2))} \tag{2.76}$$

From Equation 2.65, the asymptotic method for elliptical beam input including pump depletion is:

$$\frac{1}{1-\eta_a} = 1 + \sqrt{2\ln 2} \frac{\gamma U_1}{t_p} l_{S-T} \int_0^L \frac{dz}{\sqrt{b_x b_y (1 + \tau_x^2(z))(1 + \tau_y^2(z))}} \tag{2.77}$$

The asymptotic method for round beam input is:

$$\frac{1}{1-\eta_a} = 1 + \sqrt{2\ln 2} \frac{\gamma U_1 l_{S-T}}{2t_p} \left[\arctan\left(\frac{2(L - z_0)}{b}\right) - \arctan\left(\frac{-2z_0}{b}\right) \right] \tag{2.78}$$

When the beam waist of the round beam is at the crystal center, it reduces to:

$$\frac{1}{1-\eta_{amax}} = 1 + \sqrt{2\ln 2} \frac{\gamma U_1 l_{S-T}}{t_p} \arctan\left(\frac{L}{b}\right) \tag{2.79}$$

Equation 2.75 and 2.77 are the basis of our theoretical calculation of SHG efficiency with simultaneous spatial walkoff, temporal walkoff and pump depletion.

3. THE THEORETICAL STUDY OF SHG BEHAVIOR

3.1 The dependence of SHG efficiency on the beam waist position

In this chapter we will use our theory to study the type I SHG process and discuss how the conversion efficiency depends on different parameters. In our experiments the input laser beam has an elliptical cross-section, so Equations 2.75 and 2.77 are the basis of our study. Before doing the numerical calculations we define some dimensionless parameters: $q = w_{0x}/w_{0y} = \sqrt{b_x/b_y}$ represents the ellipticity of the fundamental beam; $\sigma = L/l_{S-T}$ is a measure of the crystal length relative to the generalized walk-off length; $\mu = L/b_x$ is a comparison between the crystal length and the confocal parameter; $\Delta\phi = \Delta kL$ is the total phase mismatch over the crystal; $f_0 = 2(L/2 - z_{0x})/b_x$ is the distance between the crystal center and x beam waist position normalized to x depth of focus; $f_d = 2(z_{0x} - z_{0y})/b_x$ is the distance between the beam waist positions in x and y directions normalized to x depth of focus (positive means that x beam waist is closer to the output end). For convenience we list all these dimensionless parameters in Table. 3.1 below.

Simple algebra shows that $\tau_y(z) = q^2(\tau_x(z) + f_d)$ for any z. We will transform the equations we derived to use these dimensionless parameters. Let $\tau_x(z_1) = \tau_{x1}$ and $\tau_x(z_2) = \tau_{x2}$ in Equation 2.75, and Equation 2.75 can be transformed into:

$$\frac{1}{1-\eta} = 1 + \sqrt{\frac{2\ln 2}{\pi}}\frac{\gamma U_1}{t_p}\frac{qL}{4\mu} \int_{f_0-\mu}^{f_0+\mu}\int_{f_0-\mu}^{f_0+\mu} \frac{\exp\left(i\Delta\phi(\tau_{x1}-\tau_{x2})/2\mu\right)\exp\left(-\sigma^2(\tau_{x1}-\tau_{x2})^2/4\mu^2\right)d\tau_{x1}d\tau_{x2}}{\sqrt{(1-i\tau_{x1})(1-iq^2(\tau_{x1}+f_d))(1+i\tau_{x2})(1+iq^2(\tau_{x2}+f_d))}} \quad (3.1)$$

Let $\tau_x(z) = \tau_x$ in Equation 2.77, and Equation 2.77 can be transformed into:

$$\frac{1}{1-\eta_a} = 1 + \sqrt{2\ln 2}\frac{\gamma U_1}{t_p} l_{S-T}\frac{q}{2}\int_{f_0-\mu}^{f_0+\mu} \frac{d\tau_x}{\sqrt{(1+\tau_x^2)(1+q^4(\tau_x+f_d)^2)}} \quad (3.2)$$

Table 3.1
The definitions of dimensionless notations

Notation	Expression	Physical meaning
σ	L/l_{S-T}	crystal length normalized to the walkoff length
μ	L/b_x	crystal length normalized to x depth of focus
$\Delta\phi$	ΔkL	total phase-mismatch across the crystal
q	w_{0x}/w_{0y} or $\sqrt{b_x/b_y}$	ellipticity of the fundamental beam
f_0	$2(L/2 - z_{0x})/b_x$	the longitudinal distance between the crystal center and x beam waist normalized to x depth of focus
f_d	$2(z_{0x} - z_{0y})/b_x$	the longitudinal distance between x and y beam waists normalized to x depth of focus
$\tau_x(z)$	$2(z - z_{0x})/b_x$	the longitudinal distance between an arbitrary z position and x beam waist normalized to x depth of focus
$\tau_y(z)$	$2(z - z_{0y})/b_y$	the longitudinal distance between an arbitrary z position and y beam waist normalized to y depth of focus

Again the subscript "a" means the asymptotic method. The integrals in the above equations use all dimensionless parameters. If we assume that the beam waist is at the crystal center ($f_0 = 0$), the integral in Equation 3.1 and 3.2 would be from $-\mu$ to $+\mu$. We extract part of Equation 3.1 and define it as h:

$$h = \frac{q}{4\mu}\int_{f_0-\mu}^{f_0+\mu}\int_{f_0-\mu}^{f_0+\mu}\frac{\exp\left(i\Delta\phi(\tau_{x1}-\tau_{x2})/2\mu\right)\exp\left(-\sigma^2(\tau_{x1}-\tau_{x2})^2/4\mu^2\right)d\tau_{x1}d\tau_{x2}}{\sqrt{(1-i\tau_{x1})(1-iq^2(\tau_{x1}+f_d))(1+i\tau_{x2})(1+iq^2(\tau_{x2}+f_d))}} \tag{3.3}$$

h is the part of Equation 3.1 which solely determines the dependence of the conversion efficiency on phase-mismatch, beam size and beam waist positions in the nonlinear crystal. h is a function of σ, μ, $\Delta\phi$, q, f_0 and f_d, but it's not connected to the input pulse energy U_1. Note that η increases monotonically with h, and in the non-depletion approximation the efficiency η is proportional to h. For a round beam $q = 1$, $f_d = 0$, we have:

$$h = \frac{1}{4\mu}\int_{f_0-\mu}^{f_0+\mu}\int_{f_0-\mu}^{f_0+\mu}\frac{\exp\left(i\Delta\phi(\tau_{x1}-\tau_{x2})/2\mu\right)\exp\left(-\sigma^2(\tau_{x1}-\tau_{x2})^2/4\mu^2\right)d\tau_{x1}d\tau_{x2}}{(1-i\tau_{x1})(1+i\tau_{x2})} \tag{3.4}$$

In this section we are interested in the dependence of efficiency on the longitudinal beam waist position, or equivalently, the dependence of h on f_0 in our theory. For a round beam it may be obvious that the optimal beam waist position is at the crystal center ($f_0 = 0$) due to symmetry. Here we will use Equation 3.4 to demonstrate it. The calculated results are shown in Fig. 3.1.

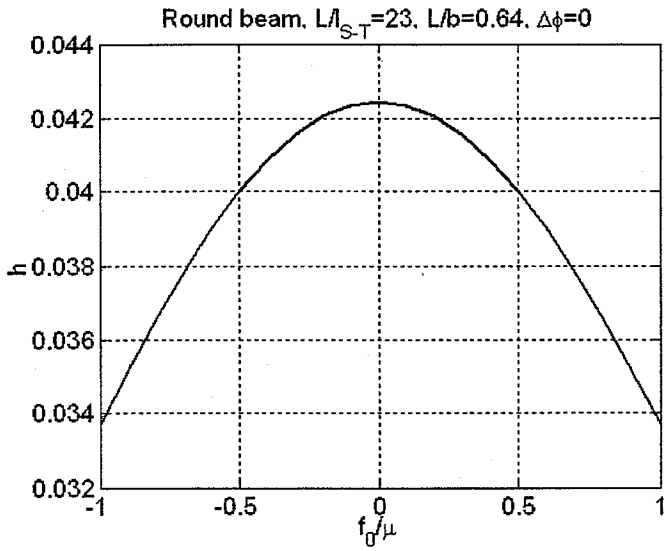

Fig. 3.1. The dependence of SHG efficiency on fundamental beam waist position (round beam)

In Fig. 3.1, when $f_0/\mu = -1 \Rightarrow z_0 = L$, the beam waist is on the output end of the crystal; when $f_0/\mu = 1 \Rightarrow z_0 = 0$, the beam waist is on the input plane of the crystal. We can see that the optimal efficiency happens when $f_0 = 0 \Rightarrow z_0 = L/2$, or the optimal beam waist position is at the crystal center. In Fig. 3.1, L/l_{S-T} and L/b are from one of our experiments with an 8mm BBO crystal, and we assumed the phase matching condition $\Delta\phi = 0$. We also did calculations with other L/l_{S-T}, L/b and $\Delta\phi$ values, and they showed that the optimal beam waist position is always at the crystal center for a round fundamental beam. This is also true for a special kind of elliptical beams with $f_d = 0$ (the longitudinal X and Y beam waist positions are the same although the X and Y beam waist sizes are different).

Generally elliptical input beams have different X and Y beam waist positions. In that case, f_0 by definition denotes the X beam waist position with respect to the crystal center, and f_d denotes the distance between X and Y beam waists. Note that X and Y beam waists don't affect the efficiency in a symmetrical way, because X direction is the direction of the spatial walkoff, and there is no spatial walkoff in the Y direction (see Fig. 2.1). The optimal beam waist position (optimal f_0) generally depends on the X and Y beam waist sizes (w_{0x} and w_{0y}, or equivalently, μ and q). It also depends on f_d. We don't have the dependence of f_0 on μ, q and f_d in an analytical form, but for specific μ, q and f_d we can calculate the h vs. f_0 curve using Equation 3.3 and find the optimal f_0 numerically. It is reasonable to think that the crystal center should be somewhere between the X and Y beam waists to maximize the efficiency, which means that the optimal f_0 should be between 0 and $-f_d$. This is confirmed by our calculations shown in Fig. 3.2.

Fig. 3.2 is also calculated based on the parameters from our experiments with the 8mm BBO assuming the phase matching condition. F is the focal length of the lens we used to focus the fundamental beam into the crystal in the experiments. In all the plots f_d is 2.2 (also from experiments). The optimal f_0 in all plots satisfies that f_0/f_d is between 0 and -1. In Fig. 3.2, the optimal f_0/f_d is about -0.1 for 140mm lens, -0.2 for 100mm lens, and -0.4 for 65mm lens. One phenomenon is that

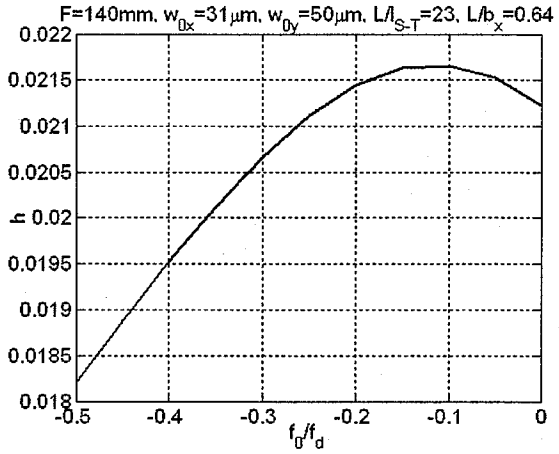

(a)

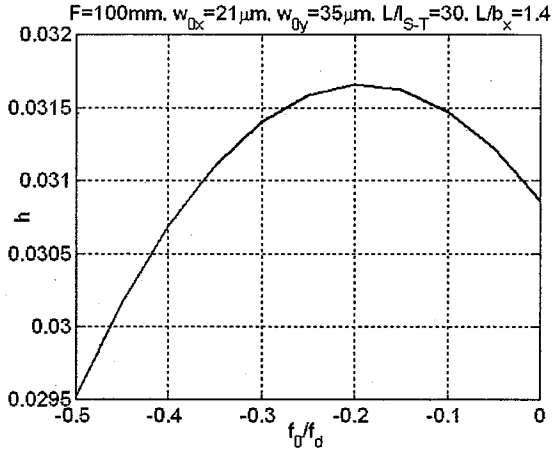

(b)

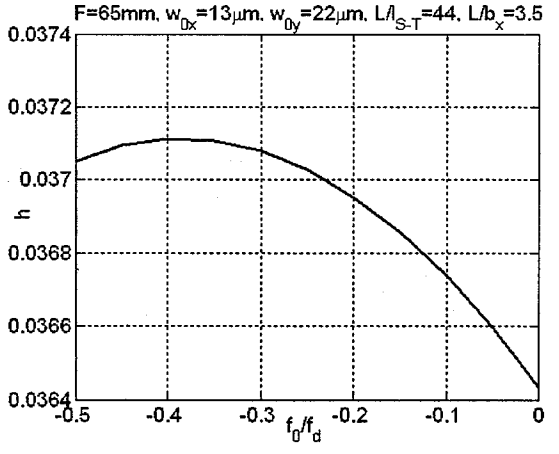

(c)

Fig. 3.2. The dependence of SHG efficiency on fundamental beam waist position (elliptical beam)

with looser focusing, the optimal f_0/f_d is closer to 0. Another phenomenon is that with tighter focusing, the dependence of efficiency on f_0 becomes weaker. As we can see in Fig. 3.2, when f_0/f_d changes from 0 to -0.5, the relative change of h is about 18% for 140mm lens, 7% for 100mm lens, and only 1.9% for 65mm lens. Physically it is because under tight focusing, the SHG process is highly localized and most of the SH energy is generated in a small spatial range, and so when the beam waist moves away from the optimal point the efficiency doesn't change very much.

Based on what we have shown in this section, for a round input beam or elliptical input beams with $f_d = 0$, we should set $f_0 = 0$ when calculating the optimal efficiency. For elliptical input beams with $f_d \neq 0$, the optimal f_0 depends on the beam shape and can only be determined numerically. We must find the optimal f_0 first to calculate the optimal efficiency. However, if the focusing is very tight, the efficiency depends very weakly on the beam waist position and then $f_0 = 0$ can be assumed to calculate an approximate optimal efficiency.

3.2 The dependence of SHG efficiency on the phase mismatch

In this section we will study the dependence of efficiency on the phase mismatch, or equivalently, the dependence of h on $\Delta\phi = \Delta kL$. Here we assume a round fundamental beam and that the beam waist is at the crystal center like in Ref. [13]. We also did calculations using an elliptical beam (q=0.6) and found that there is no fundamental difference.

In Boyd&Kleinman's theory [13] it was shown that the optimal Δk is no longer 0 for focused Gaussian beams (Equation 1.9), which is different from the case of plane-wave sources (Equation 1.4). This is because for focused input beams the wave vectors of the interacting waves have an angular distribution (with respect to θ for example), so vector phase matching ($\vec{k_1}(+\theta) + \vec{k_1}(-\theta) = \vec{k_2}(0)$) can happen when the scalar phase matching ($2k_1 = k_2$) is not satisfied. It was also shown in Ref. [13] that the efficiency η vs. $\Delta\phi$ behavior changes with different L/b values. When L/b is

small (loose focusing), η vs. $\Delta\phi$ curve still looks like a $sinc^2$ function similar to the case for the plane-wave sources, but the central peak is a little away from $\Delta\phi = 0$ point. When L/b is big (tight focusing), the curve becomes very asymmetrical.

In our theory for focused and pulsed sources, the η vs. $\Delta\phi$ curve depends on two parameters: L/l_{S-T} and L/b, which we defined as σ and μ above. Calculating h vs. $\Delta\phi$ curve for different L/l_{S-T} and L/b values, we found that there are basically three regions, as we show in Fig. 3.3.

In Region 1 we have $L/l_{S-T} < 1$ and $L/b < 1$(weak walk-off and weak focusing). The h vs. $\Delta\phi$ curve has an oscillating feature similar to a $sinc^2$ function and is basically symmetrical (but with the central peak occurring for some $\Delta\phi < 0$). This is similar as the loose focusng case in Boyd&Kleinman's theory we mentioned above. An example is shown in Fig. 3.3(a). Region 2 is characterized by $L/b >> 1$ and $L/b > L/l_{S-T}$ (strong focusing and the walk-off length is longer than the confocal parameter). In this region the curves still have an oscillating feature but it is far from symmetrical, as shown in Fig. 3.3(b). In the sense that the curve is asymmetrical and still oscillating, this region is similar to the tight focusing case in Boyd&Kleinman's theory we mentioned. In Fig. 3.3(b) the maximum point is at the positive side but very close to 0. In Region 3 we have $L/l_{S-T} >> 1$ and $L/l_{S-T} > L/b$ (strong walk-off and the confocal parameter is longer than the walk-off length). In this region the curves look like a single wide peak with no oscillation, as in Fig. 3.3(c). This is a new phenomenon which we didn't see in Boyd&Kleinman's theory. In this region the optimal efficiency takes place for $\Delta k < 0$, however, the efficiency at 0 is still very close to the optimal efficiency.

In a later chapter, we will see that our experiments were designed to have large walkoffs to test the new parameter range covered by our theory comparing with previous theories. Thus our experiments turn out to be all in Region 3. We can assume $\Delta\phi = 0$ in predicting the optimal efficiencies for our experiments, since the error arising from this approximation should be very small.

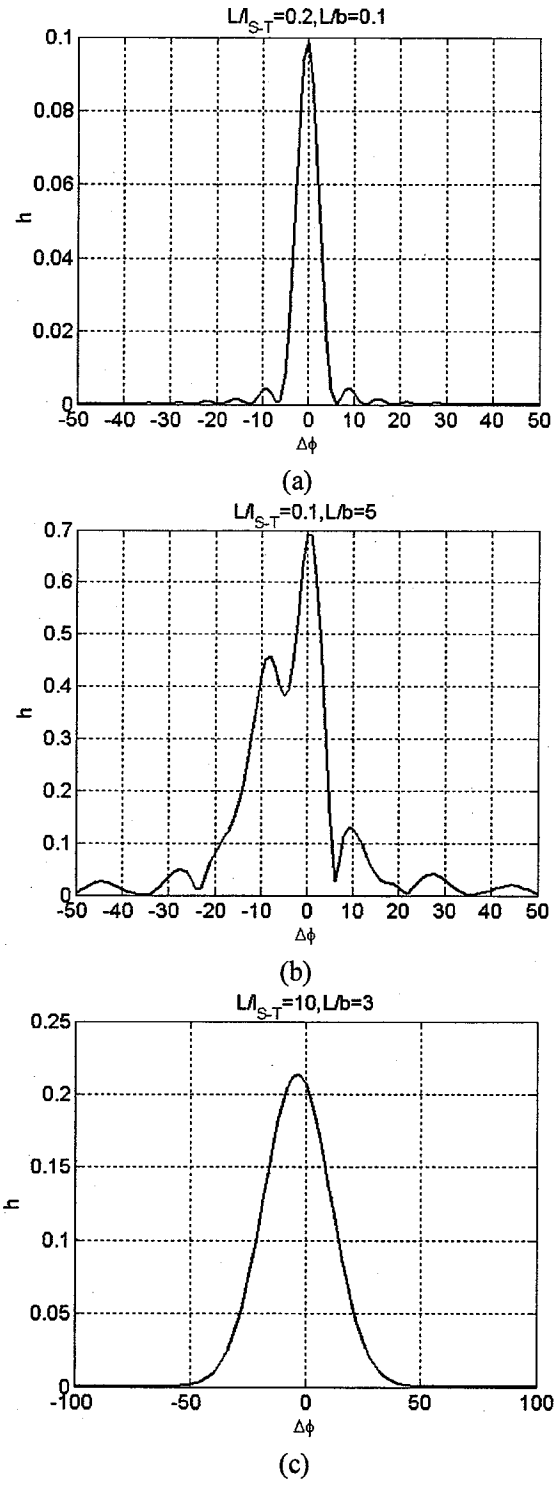

Fig. 3.3. The dependence of SHG efficiency on the total phase mismatch

3.3 The dependence of SHG efficiency on the focusing

In this section we will study the dependence of SHG efficiency on the focusing. There are several ways to describe the focusing condition. Here we use the parameters we defined with the confocal parameters: $\mu = L/b_x$ and $q = \sqrt{b_x/b_y}$. Another equivalent way is to use the beam waist sizes: w_{0x} and $q = w_{0x}/w_{0y}$, which we will use in the later chapters.

First we will study the focusing dependence of SHG efficiency using Equation 3.4 assuming round beams ($q = 1$, $f_d = 0$), phase matching ($\Delta k = 0$) and optimal beam waist position ($f_0 = 0$). Basically we wish to calculate h vs. μ curves. Based on Equation 3.4, it is clear that how σ and μ are related (or equivalently, how l_{S-T} and b are related) is the key factor that determines the shape of the curve. From Equation 2.54, we have:

$$\sigma = \sqrt{A^2 + 4B^2\mu} \tag{3.5}$$

$$A = \sqrt{\frac{(\alpha^2+16)\ln 2}{8}}\frac{\beta L}{t_p} \tag{3.6}$$

$$B = \rho\sqrt{k_1 L}/2 \tag{3.7}$$

The parameter 'A' represents the temporal walk-off effect (β is the GVM) and 'B' represents the spatial walk-off effect (ρ is the walkoff angle). In CW case, Boyd&Kleinman's theory [13] also used a 'B' parameter in the studying of focusing dependence, which is exactly the same as our 'B'. Here the 'A' and 'B' parameters come naturally from the definition of the generalized walk-off length. Note that neither 'A' nor 'B' depends on focusing conditions or spatial beam profile.

Based on Equation 3.4, with our assumptions $\Delta k = 0$ and $f_0 = 0$, we can further define a function $h_m(A, B, \mu)$:

$$h_m(A, B, \mu) = \frac{1}{4\mu}\int_{-\mu}^{+\mu}\int_{-\mu}^{+\mu}\frac{\exp\left(-\sigma^2(\tau_{x1}-\tau_{x2})^2/4\mu^2\right)d\tau_{x1}d\tau_{x2}}{(1-i\tau_{x1})(1+i\tau_{x2})} \tag{3.8}$$

This function can be viewed as an extension of $h_m(B, L/b)$ in Boyd&Kleinman's theory [13]. It determines the focusing dependence of the SHG efficiency assuming

round input Gaussian beam, perfect phase matching and that the input beam waist is at the crystal center (optimal position). Some $h_m(A, B, L/b)$ vs. L/b curves are shown in Fig. 3.4 for several different A & B values.

In Fig. 3.4, three subfigures were calculated using different A values. There are six curves in each subfigure, and they correspond to different B values. The B values are 0, 1, 2, 4, 8 and 16 in each subfigure, from the highest curve to the lowest curve respectively. Some features of the figures are: larger A (larger temporal walk-off) decreases efficiency and causes the optimal L/b to be larger (tighter focusing); larger B (larger spatial walk-off) decreases efficiency and causes the optimal L/b to be smaller (looser focusing). In the limit of $B >> A$ and $B >> 1$ (weak temporal walkoff and strong spatial walkoff), it seems that the optimal L/b approaches a value 1.4. This is consistent with the result in Boyd&Kleinman's theory [13], which shows that in the limit of large B, the optimal L/b is approximately 1.39. It is worth mention that in the case of non-critical phase matching (B=0), the asymptotic method (Equation 2.79) and our previous study [20] suggested that the efficiency will approach an upper limit with very tight focusing. However this is not true based on our full theory (Equation 2.76 and 3.1). This is demonstrated in Fig. 3.4. Even if B=0 (no spatial walk-off), the efficiency curve still has a peak and then goes down with tighter focusing. This is because the asymptotic method and our previous theory in Ref. [20] were derived under the assumption $l_{S-T} < b$, which is inevitably violated with very strong focusing and B=0. However, the asymptotic method still works almost just as well as the full theory in most cases, as we will see in the later chapters. In our experiments, for the 8mm BBO crystal we have A=13, B=10.5, and L/b_x goes from 0.6 to 25 (varies with focusing); for the 15mm LBO we have A=15, B=3, and L/b_x goes from 1.2 to 50.

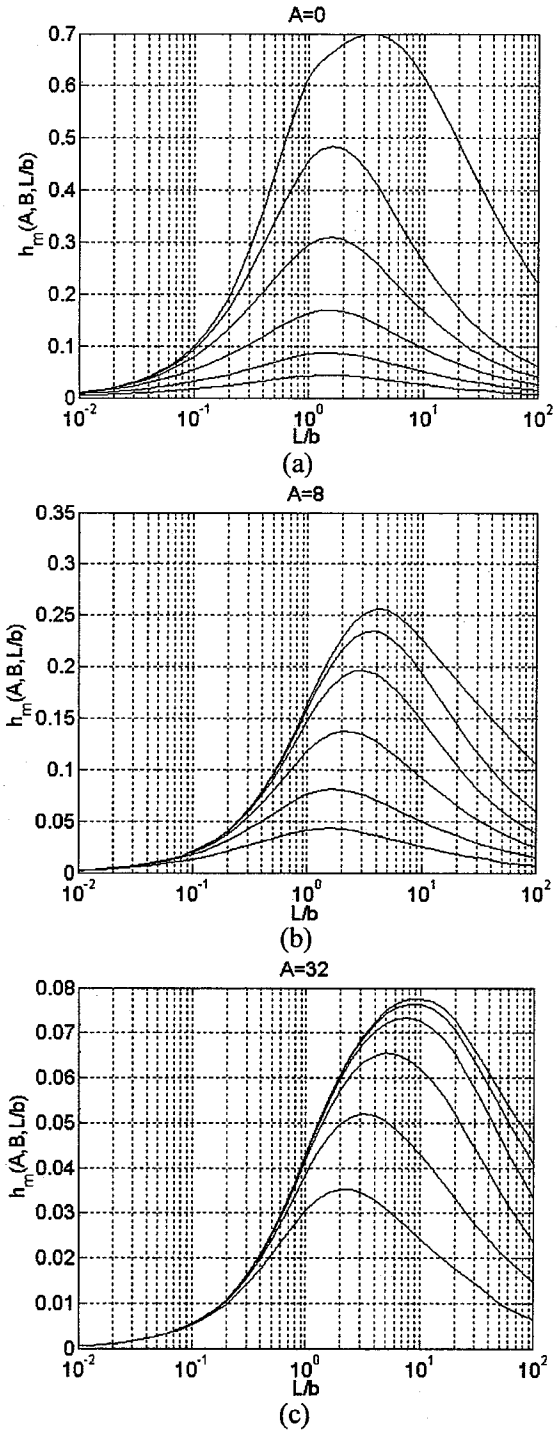

Fig. 3.4. The dependence of SHG efficiency on L/b (round beam, centered). B values are 0, 1, 2, 4, 8 and 16 in each figure, from the highest curve to the lowest curve respectively.

3.4 The dependence of SHG efficiency on the beam shape

In this section we will study the dependence of efficiency on the input beam shape. Two parameters that determine the beam shape are the ellipticity q and the longitudinal distance between the X and Y beam waists f_d.

First we will consider elliptical input beams with the same X and Y beam waist positions ($f_d = 0$) and study how the ellipticity $q = w_{0x}/w_{0y}$ affects the focusing dependence. As we mentioned before, the optimal beam waist position in this case is still the crystal center ($f_0 = 0$). Again we assume $\Delta k = 0$. Using A=13 and B=10.5 (which are for an 8mm BBO and 120fs input pulses in our experiments), We calculated the h vs. L/b_x curves for different q values (Equation 3.3). The results are shown in Fig. 3.5.

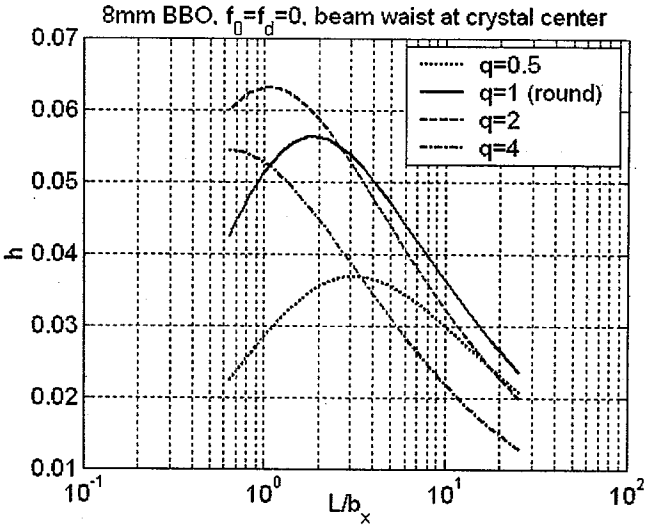

Fig. 3.5. The dependence of SHG efficiency on the ellipticity of the input beam

As we can see in Fig. 3.5, larger q makes the optimal L/b_x smaller (looser focusing). q can also affect the optimal efficiency. From Fig. 3.5, the peaks of $q = 0.5$ and $q = 4$ curves are lower than that of a round beam ($q = 1$), but the

peak of $q = 2$ curve is higher than that of a round beam. This interesting fact shows that an input beam with proper ellipticity can yield more SHG efficiency than round input beams. We would like to mention that in Ref. [33], the authors also pointed out that an elliptical beam can substantially increase the conversion efficiency in parametric oscillators.

Now we consider elliptical input beams with different X and Y beam waist positions ($f_d \neq 0$) and study how f_d affects the focusing dependence of the efficiency. We need to calculate the optimal efficiency for different L/b_x values. As we demonstrated in the first section, we must determine the optimal beam waist position f_0 for different L/b_x first. We don't have the optimal f_0 vs. L/b_x relationship in an analytical form, but we can construct an approximate relationship if we know the optimal f_0 at some L/b_x points. Here for a non-zero f_d and a fixed q, at several L/b_x points, we numerically calculated the h vs. f_0 curve and determined the optimal f_0. And by using linear interpolation we can have an approximate optimal f_0 at any L/b_x. Then we can calculate the optimal h vs. L/b_x curve. Some results are shown in Fig. 3.6.

The two subfigures in Fig. 3.6 are calculated with two different q values. In each subfigure there is a focusing dependence curve with non-zero f_d in comparison with the curve with zero f_d. We found that switching the sign of f_d (which does an mirror reflecting operation to the fundamental beam with respect to the center plane of the crystal) yields exactly the same curve, so the sign of f_d doesn't matter. As we can see from Fig. 3.6, comparing with the case of $f_d = 0$, a non-zero f_d lowers the peak of the curve and moves the peak to larger L/b_x side (tighter focusing).

In this chapter we have studied the dependence of SHG efficiency on phase mismatch, focusing, input beam shape and position according to our theory. We will compare our theory with a well-known numerical model in the next chapters.

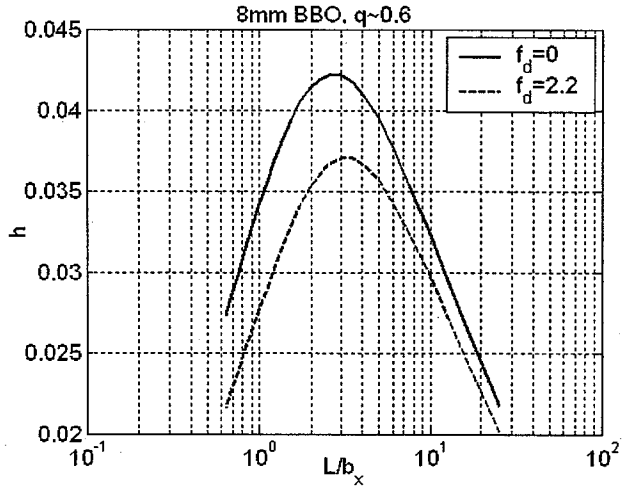

Fig. 3.6. The dependence of SHG efficiency on f_d

4. THE COMPARISON BETWEEN THEORETICAL AND NUMERICAL MODELS

4.1 The theoretical models and SNLO for thick crystals

To our knowledge our theory is the first theoretical model which can deal with type I SHG processes with simultaneous spatial walkoff, temporal walkoff and pump depletion. However, some numerical models already exist which can deal with those processes as well. Numerical models can be more versatile and accurate comparing with theoretical models, and they only need basic wave equations to work. Theoretical models always have approximations made to simplify the physical process so that the final results are understandable. On the other hand, theoretical models are more intuitive than numerical models and can reveal the relationships between parameters which were hidden behind the basic physics. In this chapter we will compare the results of our theory with a well-known three-wave mixing numerical model for different crystals.

As we mentioned in the introduction chapter, a software code named SNLO developed by Sandia National Laboratories [26, 27] includes a numerical model which can deal with short pulse mixing of round Gaussian beams. With the same inputs for a type I SHG process, we compared the results of our theory (Equation 3.1 and 3.2) with those of the numerical model. The inputs we used are: fundamental wavelength 800nm, harmonic wavelength 400nm; FWHM input pulse duration 100fs; refractive index 1.66, fundamental group velocity index 1.6845, harmonic group velocity index 1.7426 (corresponding to 193fs/mm GVM); fundamental walkoff angle 0 since it's o-wave, harmonic walkoff angle 67.7 mrad since it's e-wave; $d_{eff} = 2pm/V$; crystal length 8mm; $\Delta k = 0$. Spreading of the input fundamental pulse due to group veloc-

ity dispersion, loss and surface reflections, and other nonlinear factors such as the Kerr effect and two-photon absorption are all set to zero. The material properties are in fact from our BBO crystal, calculated from the nonlinear coefficients from Ref. [34] and Sellmeier equations from Ref. [35]. The SNLO code has been carefully benchmarked in the literature in OPO studies under loose focusing conditions [26]. Although we were unable to find studies in the literature testing SNLO under focusing as tight as in our experiments, with a proper grid and step size it should provide useful results with which to compare our theory.

Assuming that the beam waist of the round Gaussian beam is at the crystal center, we calculated the conversion efficiency for different beam waist sizes and different input pulse energy. The results are shown in Fig. 4.1. The X-axis in the figures are the e^{-2} intensity beam radius).

The curves refered to as "full theory" are calculated using Equation 3.1, and the curves refered to as "asymptotic method" are calculated using Equation 3.2. As we can see, when the input pulse energy is low (0.5nJ and 1nJ figures), the SHG is in the low pump depletion region, and SNLO results fit our theory perfectly. This is an evidence that our theory is accurate in the non-depletion region. In Fig. 4.1(b), the best efficiency is already over 30%.

In Fig. 4.1(c, d), the SHG is in the depletion region. We can see that our theory overestimated the efficiency comparing with SNLO in that region. It is because in our treatment of the pump depletion, we ignored the nonlinear reshaping of the fundamental field. The nonlinear reshaping flattens the fundamental field, and the flattened field yields smaller efficiency comparing with a Gaussian field with the same total energy. So ignoring the nonlinear reshaping will obviously result in overestimating the efficiency. As a result, in Fig. 4.1(c), we see that the shape of the curves still fit quite well, but our theoretical results are generally a few percent higher than SNLO's results. In Fig. 4.1(c), the efficiencies are already close or higher than 50%. In Fig. 4.1(d), the differences become much larger because higher pulse

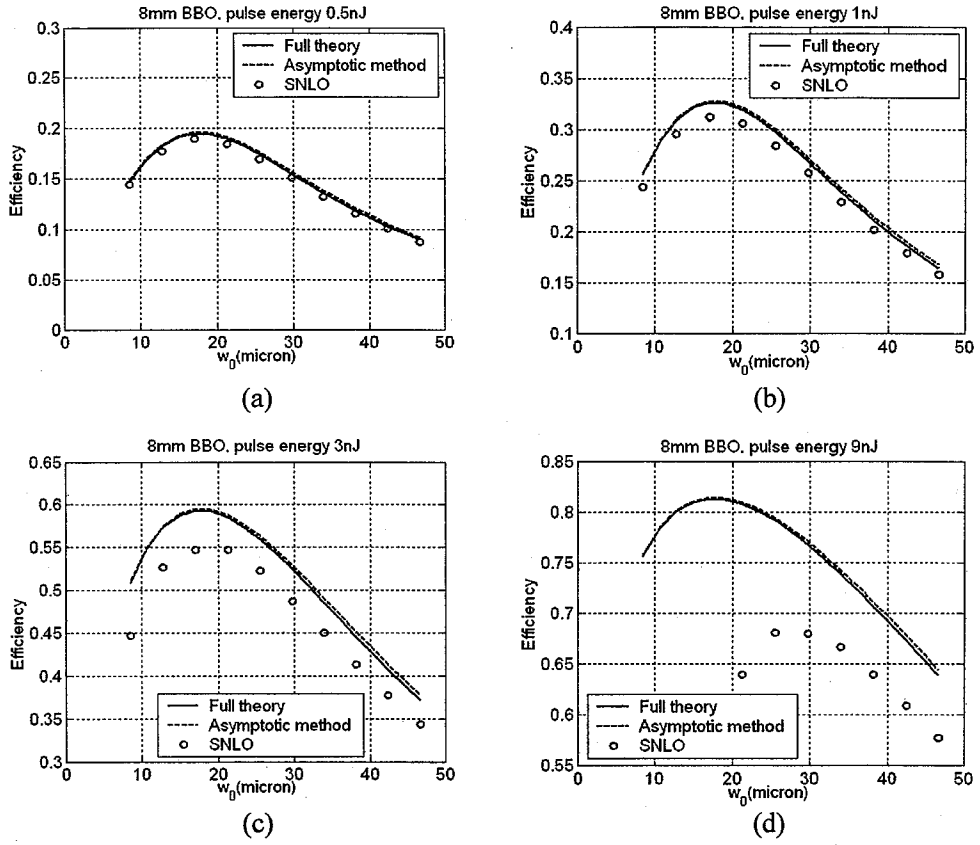

Fig. 4.1. The comparison between our theory and SNLO for 8mm BBO

energy makes the nonlinear reshaping of the pump field happen much faster, and so ignoring it is no longer acceptable.

We also did a comparison with the parameters of our LBO crystal. The inputs are: refractive index 1.60, fundamental group velocity index 1.6315, harmonic group velocity index 1.6686 (corresponding to GVM 124fs/mm); fundamental walkoff angle 0, harmonic walkoff angle 16.6 mrad; $d_{eff} = 0.723pm/V$; crystal length 15mm. The LBO properties are calculated from the nonlinear coefficients from [34] and Sellmeier equations from [36]. All other inputs are the same as the previous calculation. The results are in Fig. 4.2.

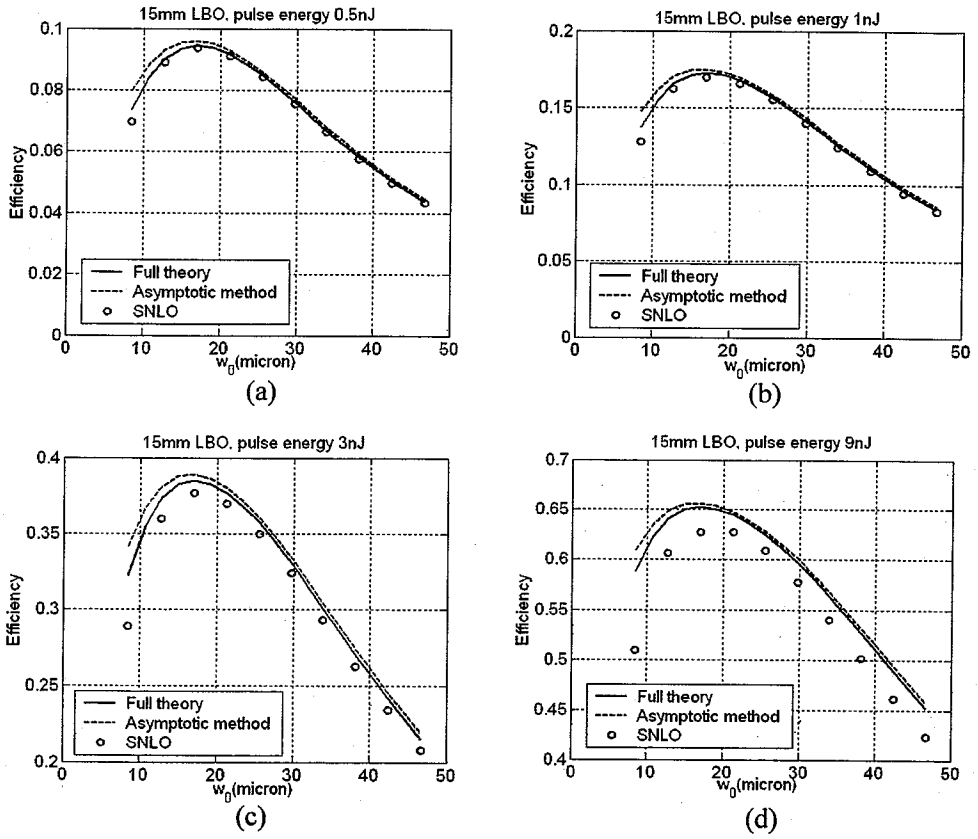

Fig. 4.2. The comparison between our theory and SNLO for 15mm LBO

Fig. 4.2 basically reveals the same phenomena in Fig. 4.1, but for the LBO the curves still fit quite well even for 9nJ pulse energy (the efficiency is as high as 60%). This is because LBO has a much smaller nonlinearity than BBO, and so the nonlinear reshaping of the pump field happens much more slowly for the same pulse energy.

Since our theory is an extension of Boyd&Kleinman's theory [13], we decided to compare the calculated efficiency of a CW Gaussian input using Boyd&Kleinman's theory and SNLO. The results are shown in Fig. 4.3 for both crystals. Basically

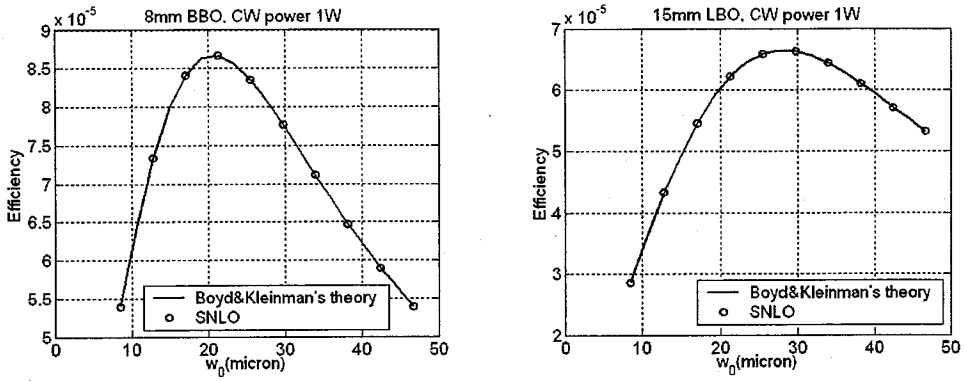

Fig. 4.3. The comparison between Boyd&Kleinman's theory and SNLO

they fit perfectly as well. This is a strong evidence that both models are accurate in the non-depletion region.

4.2 The shift of the optimal beam waist position predicted by SNLO

We further use SNLO to calculate the optimal beam waist position for different pulse energies. We know that for a round input beam and with no pump depletion, the optimal beam waist is at the crystal center, which is a fact in both our theory and Boyd&Kleinman's theory. As we mentioned, in our theory the optimal beam waist position is always at the crystal center for a round input beam regardless of the depletion, which is a result of ignoring the nonlinear reshaping of the pump field caused by depletion. Here we use SNLO to study how the optimal beam waist changes with the input pulse energy if the nonlinear reshaping is taken into account. We still assume that the input is a round Gaussian beam, and the beam waist diameter is $35\mu m$ (the corresponding e^{-2} beam radius is $29.7\mu m$) in an 8mm BBO crystal. The results are shown in Fig. 4.4.

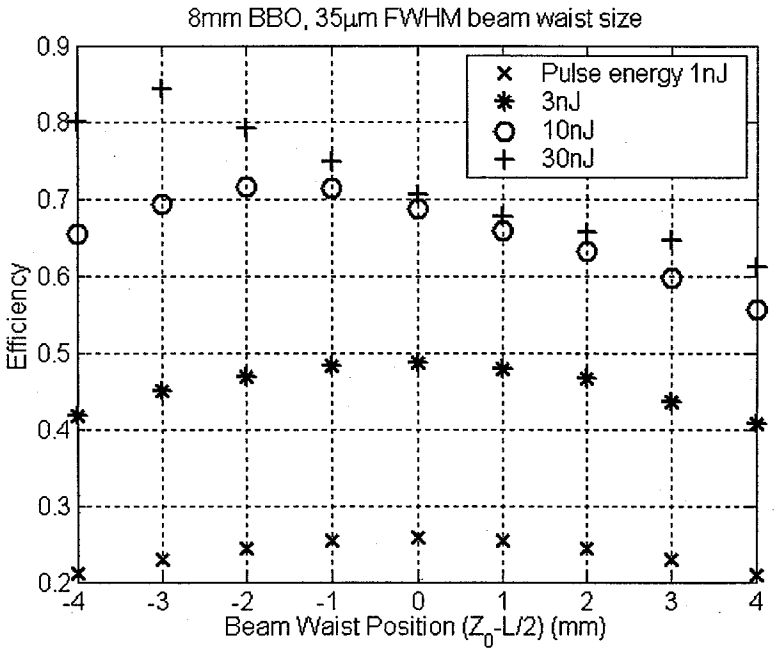

Fig. 4.4. The optimal beam waist position under different pulse energies

In Fig. 4.4, the beam waist is at the crystal center when $(z_0 - L/2) = 0$, at the input end when $(z_0 - L/2) = -4mm$, at the output end when $(z_0 - L/2) = 4mm$. For 1nJ and 3nJ input pulse energies, the optimal beam waist positions appear to be at the crystal center, or at least very close to it. For 3nJ pulse energy the efficiency is already near 50%. For higher input pulse energies, the optimal beam waist position moves to the input end of the crystal. For 10nJ it's somewhere between -1 and -2mm; for 30nJ it's near -3mm (only 1mm away from the input end). This is understandable because, to achieve better efficiency, the high peak intensity at the beam waist is better to be utilized before the nonlinear reshaping happens (which flattens the field profile and reduces the peak intensity). So the optimal beam waist should be expected to move to the input side for higher input pulse energy.

Based on the above comparisons, we have seen that our theory and SNLO agree extremely well in the non-depletion region. In the depletion region they still agree

quite well with efficiencies up to 50%. Further pump depletion will enlarge the discrepancies because our treatment in the depletion region ignores the nonlinear reshaping of the pump field. In the next section we will compare our theoretical results and experimental data for the 8mm BBO and 15mm LBO. Since we used elliptical beams in our experiments, it's not possible to use SNLO to simulate the experimental results.

5. THE COMPARISON OF OUR THEORY AND EXPERIMENTAL RESULTS

5.1 Description of the experiments

In this chapter we will compare the predictions of our theory with our experimental results using long crystals. The experimental setup is shown in Fig. 5.1.

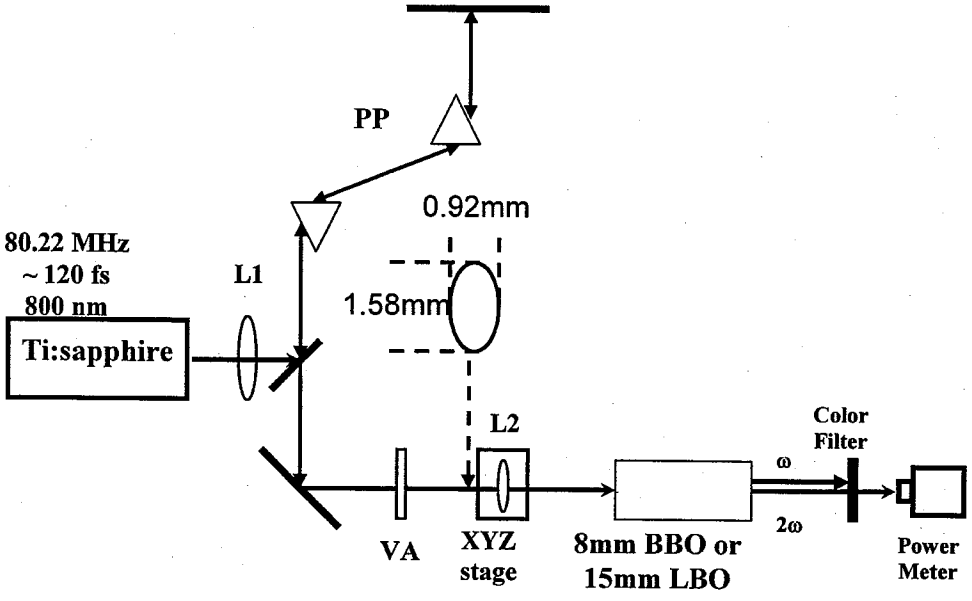

Fig. 5.1. The experimental setup

The input is from a mode-locked Ti:Sapphire Laser (Spectra Physics Tsunami) with center wavelength 800nm (near IR) and repetition rate 80 MHz. The lens L1 is a long-focal-length lens that we use to control the beam size. The prism

pair is for dispersion compensation. The optimized pulse has a duration (t_p in the theory) of 122fs FWHM, estimated from autocorrelation measurements assuming the deconvolution factor 1.44. The variable attenuator is to control the input power. The best input power we could get was a little over 900mW. The lens L2 is the input lens which focuses the fundamental beam into the crystal. We measured the beam profile at different locations and its propagation matches that of an elliptical Gaussian beam. Right before the input lens, the FWHM beam width in intensity is 0.919mm in the horizontal (y) direction, and 1.58mm in the vertical (x) direction; the horizontal beam waist is 1.022m before the lens and the vertical beam waist is 1.086m before the lens. Knowing the focal length of the input lens and the beam profile, we then can calculate the e^{-2} intensity beam waist radius, beam waist position and depth of focus in both x and y directions after focusing by considering the transformation of Gaussian beam through lens L2. The lenses we used as L2 in the experiments have 8 different focal lengths: 25mm, 31mm, 36mm, 50mm, 65mm, 80mm, 100mm and 140mm. The calculated results are listed in Table 5.1.

Table 5.1
The beam waist sizes and positions in air after focusing

$F(mm)$	$w_{0x}(\mu m)$	$w_{0y}(\mu m)$	$b_x(mm)$	$b_y(mm)$	$(z_{0x}-z_{0y})/b_x$	$(z_{0x}-z_{0y})/b_y$
25	4.91	8.34	0.189	0.546	1.0975	0.3799
31	6.12	10.38	0.294	0.846	1.0987	0.3818
36	7.14	12.10	0.400	1.150	1.0996	0.3835
50	10.06	16.95	0.795	2.256	1.1021	0.3881
65	13.28	22.26	1.385	3.892	1.1047	0.3931
80	16.60	27.66	2.164	6.009	1.1071	0.3984
100	21.18	35.04	3.523	9.643	1.1100	0.4056
140	30.96	50.39	7.528	19.94	1.1148	0.4209

In Table 5.1 F is the focal length of the input lens L2. The other parameters are the beam waist radii, confocal parameters and beam waist positions which were defined following Equation 2.28. After entering the crystal the Gaussian beam waist size remains unchanged, but the position of the waist will be shifted by an amount proportional to the refractive index. And so in the crystals, b_x and b_y values in Table 5.1 should be multiplied by the refractive index of the crystal, but all the other values remain the same. The nonlinear crystal is either an 8mm BBO crystal or 15mm LBO crystal (provided by U-Oplaz, formerly known as CASIX). They are cut for type I SHG at 800nm. For BBO, $\theta = 29.18^o$, $\phi = 90^o$ (in the conventional coordinate system as in [34]), $n = 1.66$, $\rho = 3.9^o$, $d_{eff} = 2pm/V$ [34], $\beta = 193fs/mm$; For LBO, $\theta = 90^o$, $\phi = 31.7^o$, $n = 1.61$, $\rho = 0.95^o$, $d_{eff} = 0.723pm/V$ [34], $\beta = 124fs/mm$. The walkoff angle, refractive index, and GVM are calculated from the Sellmeier equations [35, 36]. The generated SH light has a wavelength centered near 400nm (blue). Both crystals are AR-coated at 400nm and 800nm on both ends. The blue output power was detected after a color filter. Within the accuracy of our measurements, we did not observe any linear or nonlinear absorption in the crystals.

5.2 The focusing dependence of the optimal efficiencies

We need to theoretically calculate the optimal efficiency we can get from the crystals under certain input power and certain focusing, and then compare the theoretical predictions with the optimal efficiencies in experiments. In the theoretical calculation, we set $\Delta k = 0$. As we mentioned in Chapter 3, for an elliptical input beam, to calculate the optimal efficiency we must determine the optimal beam waist position first. For a round beam we know that it's the crystal center in our theory ($f_0 = 0$), but for elliptical beams the theoretical optimal beam waist position (optimal f_0) depends on the focusing and the distance between the x and y beam waists (f_d) (see Equation 3.1). We took into account the focusing dependence of the optimal f_0 in a way similar as what we did when calculating Fig. 3.6. From Table 5.1 we can see

that $(z_{0x}-z_{0y})/b_x = f_d/2$ is almost constant at 1.1. Setting $f_d = 2.2$ in Equation 3.1, we numerically calculated the efficiency vs. f_0 curve for each lens we used, and from these curves we get the optimal f_0 for each lens. Then we construct an approximate function describing the dependence of the optimal f_0 on the lens focal length, so that we can calculate the approximate optimal value of f_0 for any lens with the focal length F between 25mm and 140mm. We included this dependence in our program, and in this way we can calculate a continuous curve of optimal efficiency vs. F (or the beam waist radius w_{0x} in crystal, equivalently). The approximate optimal f_0 vs. F functions are: for BBO, if $F < 80mm$, $f_0/f_d = -0.3$; f_0/f_d goes from -0.3 to -0.2 linearly with respect to F as F goes from 80mm to 100mm; f_0/f_d goes from -0.2 to -0.1 linearly with respect to F as F goes from 100mm to 140mm. For LBO, if $F < 80mm$, $f_0/f_d = -0.4$; f_0/f_d goes from -0.4 to -0.3 linearly with respect to F as F goes from 80mm to 100mm; f_0/f_d goes from -0.3 to -0.2 linearly with respect to F as F goes from 100mm to 140mm. With the above approximate optimal f_0 vs. F functions, the calculated optimal efficiencies are within 0.1% to the real optimum in our theory, which we think is good enough.

First we did an experiment with the 140mm focal-length lens and the BBO crystal. We optimized the SHG efficiency under a relatively low input power (250mW) by tuning the prism pair, the position of the input lens and the orientation of the crystal. We then fixed the position of the input lens and crystal and increased the input power. We found that the conversion efficiency first increased, reached a maximum of 43% at around 600mW input power, and then dropped under higher input powers. No power loss was observed in the experiments even when the input power is 900mW (The total output power of the IR and blue pulses are within 2% difference from the input power, which is within the measurement error range). Fig. 5.2 shows the efficiency vs. input power data for this measurement.

We also found that the drop in efficiency at high input power is related to the change of the optimal beam waist position (or optimal input lens position in experiments) with input power. If we optimized the output power at a relatively low

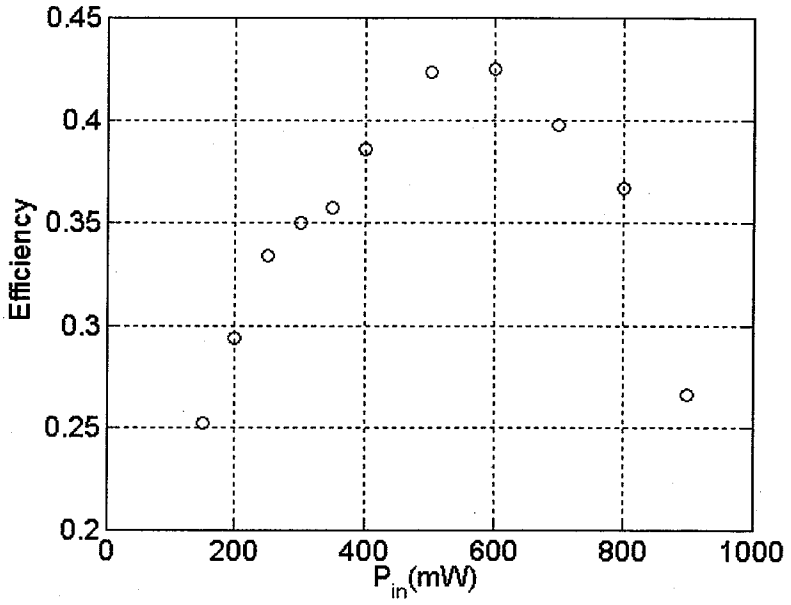

Fig. 5.2. The efficiency saturation when all conditions are optimized under low input power

input power (such as 150mW), we found that for both the LBO and BBO crystal, the distance between the input lens and the crystal must be increased at higher powers to maintain optimal output, which means that the optimal beam waist position moves to the input end of the crystal at higher powers. This is consistent with the numerical results in the previous chapter (Fig. 4.4). The shift of the optimal beam waist position is only an issue beyond 600mW input power in our case, and can be ignored otherwise (the optimal beam waist position remains unchanged). Experimentally this phenomenon is more serious when the input lens has a longer focal length (larger beam size in crystal), which indicates that it may have some dependence on the confocal parameter of the Gaussian beam in the crystal. Also, this effect is more serious for BBO than for LBO, which could be related either to the fact that the LBO crystal is longer or to its different material properties. For 8mm BBO with a 140mm input lens (the longest input focal length we used in the

experiments), the distance between the lens and the crystal has to be increased by 4.8mm ($0.38b_x$) to achieve optimal efficiency under 900mW input power compared to the optimum distance at low input power. From what we showed previously, under low input powers the optimal X beam waist satisfies $f_0 = -0.22$ for 140mm lens. Based on the data in Table. 5.1 (note that the 'b' values in crystals should be multiplied by n=1.66), the X beam waist is 1.4mm away from the crystal center when it's optimized under low powers. This means that the optimal beam waist position at 900mW could be 3.4mm away from the crystal center and only 0.6mm away from the input end of the crystal. For LBO, this phenomenon was only obvious with the 100mm and 140mm lenses and >700mW input power. With the 140mm input lens, the optimal position of the input lens at 900mW input power has a 4.5mm ($0.37b_x$) difference from that at low input powers.

In the following experiments, at high input power (700mW and above), we always adjusted the distance between the lens and the crystal to keep optimal output. Thus from now on, our data points always represent the experimentally optimized output power with a certain lens at a certain input power.

Fig. 5.3 shows the optimal efficiencies for BBO with different focused beam sizes at fixed input powers. The solid curves (full theory) are calculated using Equation 3.1; the dash curves (asymptotic method) are calculated using Equation 3.2. The little circles are the data points. As we can see, the shape of the data points and our theoretical curves are very close under low input power (low pump depletion). The discrepancies increase as the input power increases, which is expected due to the nonlinear reshaping of the pump field. We can also notice the resemblance between Fig. 5.3 and Fig. 4.1, when SHG evolves from the non-depletion region to the depletion region. In Fig. 5.3, for the input powers of 150mW, 300mW 600mW and 900mW, the pulse energies are 1.9nJ, 3.8nJ, 7.5nJ and 11.3nJ respectively. The difference between Fig. 5.3 and Fig. 4.1 is that in Fig. 4.1 the beam waist position is fixed, but in Fig. 5.3(d) the beam waist positions were adjusted to give

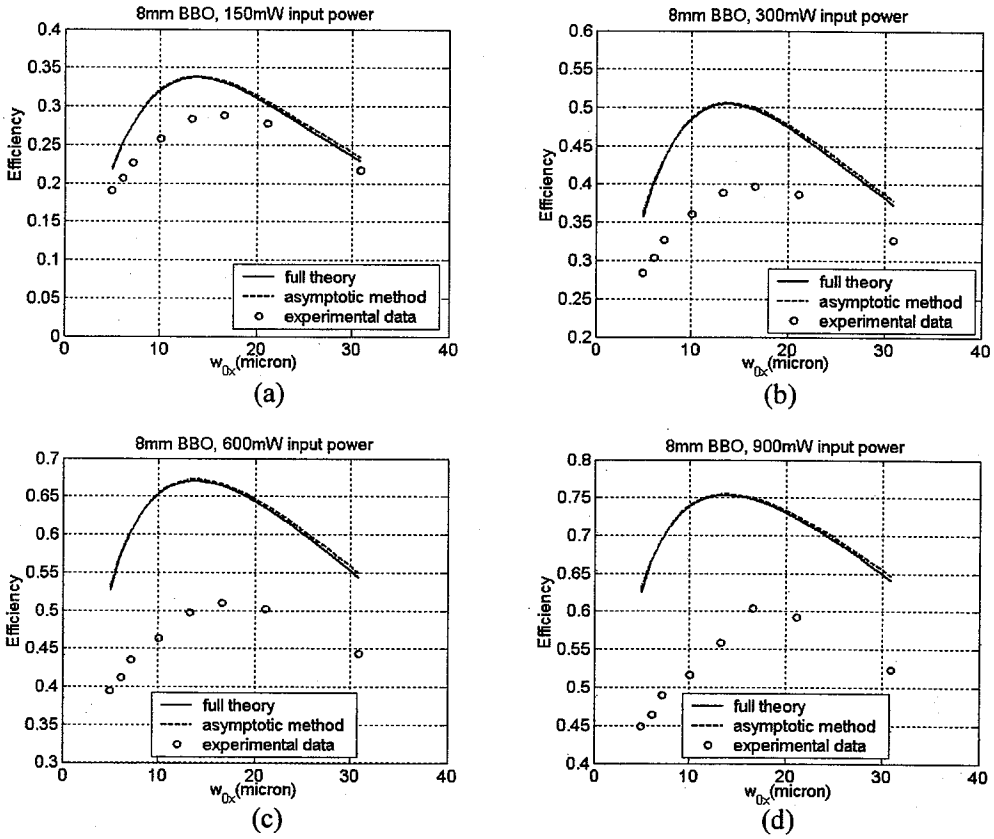

Fig. 5.3. The focusing dependence of optimal efficiencies for 8mm BBO

experimentally optimized efficiency. The best efficiency we achieved with BBO was a little over 60% with 80mm input lens and 900mW (maximum) input power.

Fig. 5.4 shows the focusing dependence for LBO crystal. Again we can see that the shape of the data points and the theoretical curves are very close under low input power. We can also see the resemblance between Fig. 5.4 and Fig. 4.2. The comments in the previous paragraph also apply here. The best efficiency we achieved with LBO was 54% with the 80mm input lens at 900mW input power.

In Fig. 5.3, Fig. 5.4, Fig.4.1 and Fig. 4.2 we can also see that the asymptotic method actually gives results very close to those of the full method. The asymp-

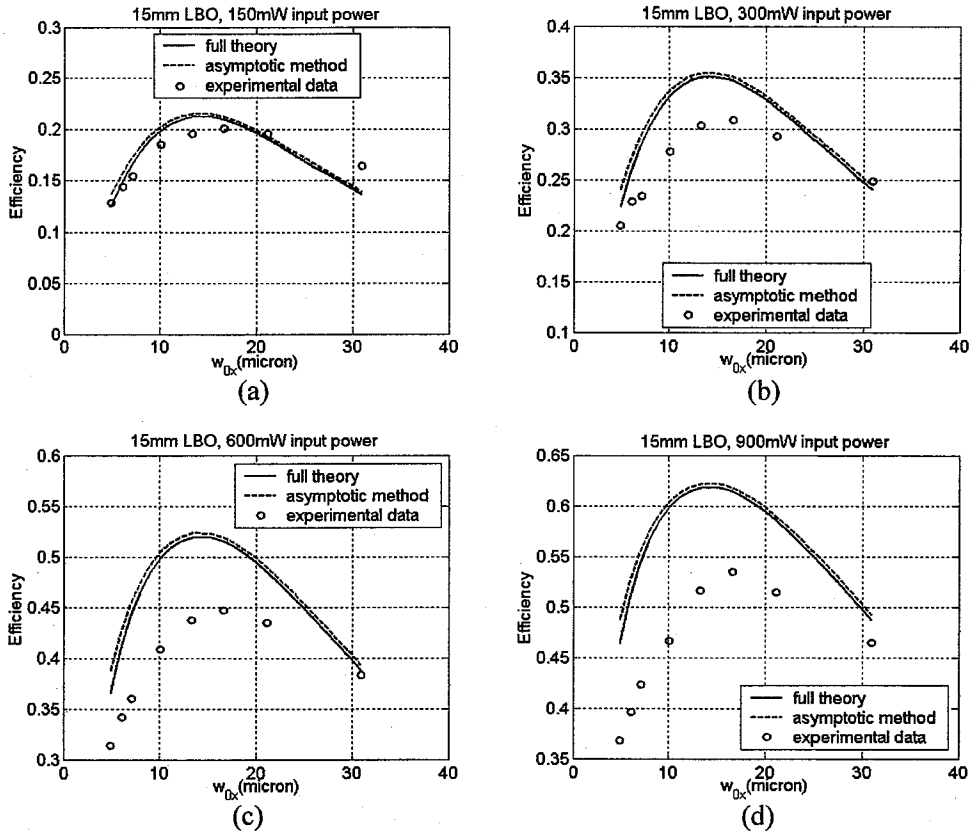

Fig. 5.4. The focusing dependence of optimal efficiencies for 15mm LBO

totic method was derived based on the assumption $l_{S-T} << b_x$, b_y and L, so we expected it to work just as well as the full theory with relatively loose focusing (b_x and $b_y >> l_{S-T}$) and sufficiently long crystals ($L >> l_{S-T}$). In Fig. 4.4(a) and (b), the asymptotic method deviates from the full theory more than in Fig. 4.1 and 4.2 because one of the assumptions $L >> l_{S-T}$ for the asymptotic method is no longer well satisfied when L is only 1mm (L/l_{S-T} ranges from 2.7 to 8 in Fig. 4.4(a) and (b), while in Fig. 4.1 and 4.2 those numbers should be multiplied by 8). However, the $l_{S-T} << b$ assumption seems to be less strict. In Fig. 5.3, b_x/l_{S-T} ranges from 4 (25mm input lens) to 32 (140mm input lens); in Fig. 5.4, b_x/l_{S-T} ranges from

0.9 (25mm input lens) to 13 (140mm input lens). Even though the $l_{S-T} << b$ assumption is no longer well satisfied for the short focal-length lenses, the asymptotic method still seems to be quite close to the full method in that region. It gives almost the same results as those of the full method for BBO in Fig. 5.3, and only has a small deviation for LBO with short focal-length input lenses in Fig. 5.4. Considering that it's much easier to calculate, the asymptotic method could be a better way to estimate type I SHG efficiency in many cases.

5.3 The power dependence of the optimal efficiencies

For a CW plane-wave source, when the phase matching condition is satisfied, Equation 1.5 gives how the efficiency depends on the input power. We list it again here:

$$\eta = \tanh^2(\kappa |A_0| L) \tag{5.1}$$

From this formula we know that when the efficiency is low (no pump depletion), it is proportional to the input power since $\tanh(x) \approx x$ when x is small. That's what we can expect from a second-order process. As the input power increases, there is more pump depletion, and the efficiency will approach 100% following a squared hyperbolic tangent curve.

Our treatment of the pump depletion gives Equation 2.74, which we also show again here:

$$\eta = 1 - \frac{1}{1 + U_1(0)F(L)} = 1 - \frac{1}{1 + \eta_{nd}} \tag{5.2}$$

Where η_{nd} is the efficiency without considering pump depletion and so it is proportional to the input power (or pulse energy in the equation). For CW plane-wave sources, from Equation 5.1, we have:

$$\eta_{nd} = \kappa^2 |A_0|^2 L^2 \tag{5.3}$$

We can use a little algebra to transform Equation 5.1, and express η in terms of η_{nd} from Equation 5.3:

$$\eta = 1 - \frac{1}{1 + \sinh^2(\sqrt{\eta_{nd}})} \tag{5.4}$$

Comparing Equation 5.4 with Equation 5.2, note that $\sinh^2(\sqrt{\eta_{nd}}) > \eta_{nd}$, we see that our treatment of the pump depletion underestimated the efficiency in the depletion region for CW plane-wave sources. The reason is that for CW fields with the phase matching condition, the existence of the SH field can enhance the up-conversion. In our treatment, as we mentioned in Chapter 2, the boundary condition in the depletion region is taken to be the same as in the non-depletion region, so the co-existence of SH field is ignored. That's why our theory underestimated the efficiency in the depletion region in this case.

For focused and pulsed sources, an important phenomenon is the nonlinear reshaping of the fundamental field. As we discussed in the previous chapter, because the stronger parts of the field deplete more than the weaker parts, the fundamental field will become flatter in the SHG process. The flattened field results in lower efficiency than a Gaussian field with the same energy. Because we ignored the nonlinear reshaping when deriving Equation 5.2 in Chapter 2, we can expect that our treatment of the pump depletion will overestimate the efficiency for focused and pulsed sources, which we have seen in Fig. 4.1, 4.2, 5.3 and 5.4. The experimental power dependence data of the optimal efficiencies are shown in Fig. 5.5 along with our theoretical curves.

Fig. 5.5 shows the power dependence of the optimal SHG efficiency for both crystals with the 80mm input lens (the lens which gives the highest efficiency). The solid curves are calculated from the full method. The little circles are the data points. We didn't show the results of the asymptotic method this time because they would be almost identical to those of the full method. Fig. 5.5(a) and (c) show the dependence of the optimal blue power vs. input power, and Fig. 5.5(b) and (d) show the optimal efficiency vs. input power. We multiplied the theoretical

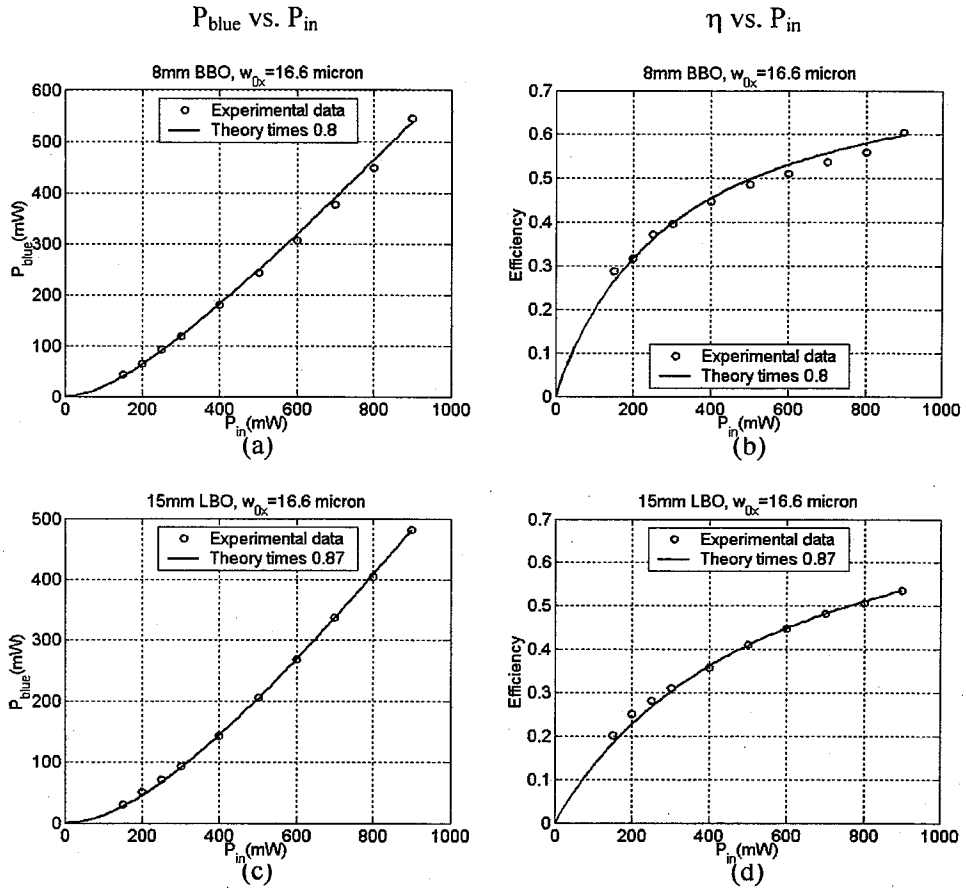

Fig. 5.5. The power dependence of optimal efficiencies for both crystals

results by a numerical factor to fit the data, because as shown in Fig. 5.3 and 5.4, our experimental results are generally lower than our theoretical results. For similar pulse energies the discrepancies in Fig. 5.3 and 5.4 are larger than in Fig. 4.1 and 4.2 where SNLO was compared with our theory. This could be due to certain non-ideal conditions in our experiments such as unaccounted pulse chirp, which can downgrade the experimental efficiency.

However, we can still see from Fig. 5.5 that the power dependences of the optimal blue power and efficiency do seem to follow a similar scaling rule in the depletion

region as our theory indicated. Furthermore, there is no sign of a rollover with increasing power. This is in contrast to Fig. 5.2, where the beam waist position was only optimized at low input powers.

6. SUMMARY OF TYPE I SHG STUDY

We have developed a novel theory which for the first time can give the efficiency of type I second harmonic generation with simultaneous temporal walkoff, spatial walkoff and pump depletion in an analytical form. Within the no pump depletion approximation, our theory may be considered as a generalization of Boyd&Kleinman's theory [13], which is a well known treatment of second harmonic generation with continuous-wave Gaussian beams. We further show how to extend into the depleted pump regime, within the approximation that the pump spatial and temporal profile remains Gaussian. We have compared the results of our theoretical model and those of a numerical solver (SNLO), and found that our theory and SNLO fit perfectly in the non-depletion region, but have discrepancies in the deep depletion region when the efficiency is well over 50%, because our treatment in the depletion region ignored the nonlinear reshaping of the pump field due to depletion. We also performed experiments with two long SHG crystals (8mm BBO and 15mm LBO) and a 120fs laser source. In the experiments both spatial and temporal walkoff are important, and the pump depletion is important with high efficiencies. The data generally support our theoretical results, especially for relatively weak pump depletion. In the deep depletion region we see discrepancies similar to what we saw in the comparison with SNLO, which can also be explained by the nonlinear reshaping. The experimental power dependence of the optimal efficiencies in the depletion region seems to follow a similar scaling rule as predicted by our theory. Our theory provides an effective tool to predict the type I SHG efficiency under many conditions not previously described via an analytical formulation and improves our understanding of the SHG process itself.

7. PART II: INTRODUCTION TO TYPE II SHG STUDY

7.1 The Basics of Type II SHG

The remaining part of the document is concerned about our study of type II SHG. In type II SHG, two fundamental fields with perpendicular polarizations interact with each other to generate the SH field. The relationship between the second order polarization field and the fundamental fields are:

$$P_{2x} = 4\epsilon_0 d_{eff} E_{1x} E_{1y} \tag{7.1}$$

One can compare Equation 7.1 with Equation 1.3 to see the difference. In the above equation the polarization field only needs to be along one of the fundamental field directions. In a uniaxial nonlinear crystal, one of the fundamental fields is an e-wave and the other is an o-wave, and the output SH field can be either o or e wave, depending on the crystal and geometry. The scalar phase matching condition for type II SHG is $k_{2o} = k_{1e} + k_{1o}$ for an oeo process or $k_{2e} = k_{1e} + k_{1o}$ for an oee process. Note that k_{1e} and k_{2e} change with the propagation direction in the crystal while k_{1o} and k_{2o} don't.

For pulsed sources, in type II SHG, GVM exists between any two of the three interacting waves. The GVM between the fundamental o-wave and e-wave leads to temporal walkoff between them, which limits their interaction length and puts constraint on the SH efficiency. Also, it's impossible to achieve non-critical phase matching (NCPM) in type II SHG for most commonly used crystals, since their type II SHG d_{eff} vanishes when the phase-matching angle reaches 90 degrees. So spatial walkoff is bound to exist in type II SHG as well. The two fundamental waves will only overlap and cause type II SHG in a limited range and then get separated in space or time due to the walkoff effects. Because of the above reasons, type II SHG normally

has much lower conversion efficiency compared with type I SHG, and increasing the length of the crystal doesn't help after it reaches the interaction length. That's why type II SHG was not as popular as type I SHG.

However, the GVM in type II SHG can be useful for wavelength conversion in optical pulse shaping. In Ref. [37–40], the pulse walkoff was used for shaping in difference frequency generation. It was also used to generate compressed second-harmonic pulses [41].

7.2 Wavelength Conversion in Optical Pulse Shaping and Our Research

Femtosecond pulse shaping using spatial light modulators(SLM) [42] is a technique now widely used within the field of ultrafast optics. SLMs are well developed for the visible and near-IR light, but are generally difficult to acquire for shorter and longer wavelengths. Although there has been progress in developing new SLM devices (e.g., MEMS arrays that have been used down to 400 nm [43]), there is still interest in developing technologies for frequency converting waveforms in the visible or near-IR into new wavelength ranges. Such waveform transfer was first demonstrated in experiment where shaped near-IR pulses were used to excite photoconductive antennas for shaping and enhancement of ultrafast THz transients [44]. Recently several groups have performed experiments demonstrating waveform transfer to longer wavelengths via difference frequency generation (DFG) [37–40]. To generate controllable waveform at shorter wavelengths, the use of phase-shaped input waveforms from a Ti:sapphire laser during second harmonic generation (SHG) was reported [45], but the scheme did not allow general control of the output waveform. Phase shaping of waveforms from a femtosecond fiber laser has also been used for coherent control of the nonlinear polarization spectrum in SHG, resulting in a novel spectral phase correlator functionality with applications to waveform recognition for ultrafast optical communications [46]. In this document we demonstrate for

the first time to our knowledge a SHG waveform transfer scheme allowing general intensity and phase control of the output second harmonic waveform.

Our idea is that in type II SHG, we make one of the input waves a relatively long waveform by using a pulse shaper, while keeping the other input wave a single short pulse (called the reference pulse). Because of the GVM between the two input waves, while they are traveling through the crystal, the reference pulse will scan through the long waveform and generate SH wave at the same time. SHG of different parts of the input waveform happens at different longitudinal locations in the crystal. The nonlinear polarization in space is a scaled version of the input temporal profile (assuming a δ pulse reference), and the output SH field in time is a scaled version of the nonlinear polarization in space. As a result the output SH wave should have a temporal waveform which is a scaled version of the input fundamental waveform. And so the GVM in type II SHG is used to transfer a waveform from a fundamental wave to the SH wave.

It is worth mentioning that other groups did pulse shaping in type I SHG using modulated quasi-phase-matching (QPM) gratings in PPLN [47]. In that case, different contributions to SH field arise at different longitudinal locations of the modulated grating, and each such contribution gives rise to different slices of the SH temporal waveform, with a scaling factor that depends on GVM between the fundamental and SH fields. Our work is similar in the sense that different contributions to the SH waveform also arise at different longitudinal locations of the crystal. However, instead of controlling it with a fixed QPM grating, we control it optically through the interaction between a short reference pulse and a shaped waveform.

We have studied this waveform transfer technique using theoretical analysis and simulations. The results show that the SH waveform can be a temporally magnified or compressed version of the fundamental waveform depending on whether the fundamental waveform or the reference pulse is the faster wave in the nonlinear media. We have also performed experiments using the type II SHG in a LBO crystal at 805nm wavelength. The SLM we used to generate the shaped fundamental waveform is a

512-element liquid crystal modulator (LCM) array [48]. The experimental results agree with our theoretical results very well. We have also demonstrated experimentally that this technique can not only transfer the intensity profile of a waveform, but also its phase profile.

The remainder of type II SHG part is structured as follows. The theoretical analysis and simulations of waveform transfer using type II SHG are presented in Chapter 8. The experimental results are presented in Chapter 9. Chapter 10 will be the conclusion of our type II SHG study.

8. THE THEORETICAL STUDY OF WAVEFORM TRANSFER IN TYPE II SHG

8.1 Theoretical Analysis

In our experiments, we use a mode-locked Ti:sapphire laser with about 133fs pulses and 805nm center wavelength as the source. For this wavelength, among single crystals, LBO seems to be the most suitable for the experiment since it has the smallest spatial walkoff. The following theoretical calculations are all for LBO, but they can be applied to other crystals easily.

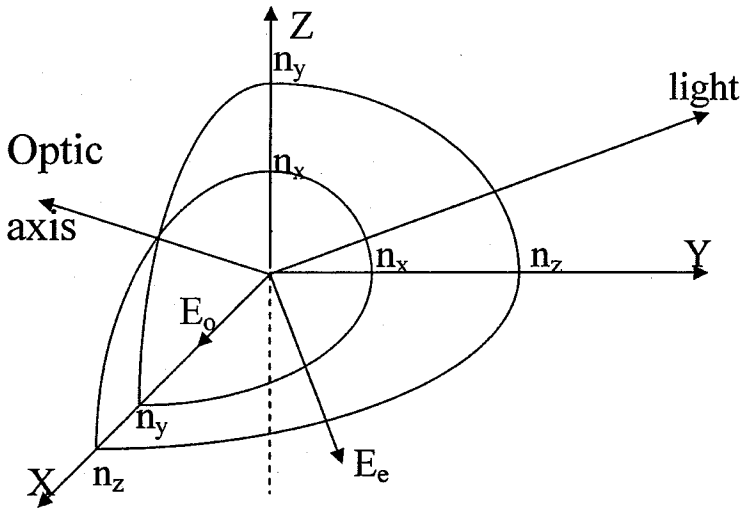

Fig. 8.1. The refractive index of LBO and type II SHG in the YZ plane

LBO is a negative biaxial crystal, and Fig. 8.1 shows a diagram of the refractive index in LBO [9]. As we can see, the index profile in LBO is considerably more

complicated than in uniaxial crystals. But here we are only studying the SHG in YZ plane, so it's still analogous to the SHG in uniaxial crystals. For light propagating in an arbitrary direction (in Fig.8.1 the arrow 'light', which is also the wave vector direction), traditionally we define θ as the angle between the direction and Z axis, and ϕ as the angle between the projection of the direction in the XY plane and the X axis. Type II SHG at 800nm happens in the YZ plane, which means that the wave vectors of the three waves must have $\phi = 90^o$. In YZ plane the o-wave has a polarization along X direction and the refractive index $n_o = n_x$. The polarization of the e-wave is in the YZ plane, and its refractive index varies with θ. When $\theta = 0$, $n_e = n_y$; When $\theta = 90^o$, $n_e = n_z$. For an arbitrary θ, it is calculated by the following equation:

$$n_e(\theta) = \frac{n_y\sqrt{1+\tan^2\theta}}{\sqrt{1+(n_y/n_z)^2\tan^2\theta}} \tag{8.1}$$

The SHG process we are studying is an oeo process, which means the output SH wave will be an o-wave. Because only the energy flow of e-wave has a different direction from its wave vector, the only spatial walkoff is from the fundamental e-wave. Our LBO crystal was cut for type II SHG at 800nm with $\theta = 76.88^o$ and $\phi = 90^o$. The spatial walkoff angle of the fundamental e-wave is $\rho = 0.24^o$. The temporal walkoff exists between any two waves. Based on the dispersion equations of LBO [36], we also calculated the group velocity of the three waves:

$$\begin{aligned}
\frac{1}{V_{go}(805nm)} &= 5289fs/mm \\
\frac{1}{V_{ge}(805nm)} &= 5435fs/mm \\
\frac{1}{V_{go}(402.5nm)} &= 5472fs/mm
\end{aligned} \tag{8.2}$$

We can see that the red o-wave is the fastest and the blue o-wave is the slowest. Now we start from the general wave equation in a medium with no loss:

$$(\nabla^2 - \frac{1}{c^2}\frac{\partial^2}{\partial t^2})\vec{E}(\vec{r},t) = \mu_0\frac{\partial^2}{\partial t^2}\vec{P}(\vec{r},t) \tag{8.3}$$

In a nonlinear crystal, the polarization field P can be divided into a linear component P^L and a nonlinear component P^{NL}. In LBO, considering the nonlinear polarization to the second order, we have [49]:

$$\begin{pmatrix} P_x^L \\ P_y^L \\ P_z^L \end{pmatrix} = \epsilon_0 \begin{pmatrix} n_x^2 - 1 & 0 & 0 \\ 0 & n_y^2 - 1 & 0 \\ 0 & 0 & n_z^2 - 1 \end{pmatrix} \begin{pmatrix} E_x \\ E_y \\ E_z \end{pmatrix} \tag{8.4}$$

$$\begin{pmatrix} P_x^{NL} \\ P_y^{NL} \\ P_z^{NL} \end{pmatrix} = 2\epsilon_0 \begin{pmatrix} 0 & 0 & 0 & 0 & 0 & d_{15} \\ d_{31} & d_{33} & d_{32} & 0 & 0 & 0 \\ 0 & 0 & 0 & d_{24} & 0 & 0 \end{pmatrix} \begin{pmatrix} E_x^2 \\ E_y^2 \\ E_z^2 \\ 2E_yE_z \\ 2E_xE_z \\ 2E_xE_y \end{pmatrix} \tag{8.5}$$

Now we consider the special case of the type II SHG in LBO described above. Assuming plane waves, from Fig. 8.1, we can write down the expressions of the three waves as below:

$$\vec{E}_o = \hat{x}\tilde{E}_o(u,t) = \hat{x}\tilde{A}_o(u,t)e^{i(\omega_0 t - k_o u)} \tag{8.6}$$

$$\vec{E}_e = (\hat{y}\cos\theta - \hat{z}\sin\theta)\tilde{E}_e(u,t) = (\hat{y}\cos\theta - \hat{z}\sin\theta)\tilde{A}_e(u,t)e^{i(\omega_0 t - k_e u)} \tag{8.7}$$

$$\vec{E}_2 = \hat{x}\tilde{E}_2(u,t) = \hat{x}\tilde{A}_2(u,t)e^{i(2\omega_0 t - k_2 u)} \tag{8.8}$$

The subscript 'o', 'e' and '2' represent the red o-wave, red e-wave and SH wave, respectively. "u" is the direction of propagation, which has the same direction of the wave vectors. The above equations of polarization field and electric field can be used in Equation 8.3, and then the components in different directions or with different frequencies can be separated. The final result will be a group of coupled equations. However, if we assume no pump depletion, which means that the conversion efficiency is low and the SH process doesn't influence the fundamental waves, the coupled equations will be decoupled and the result is more suitable for numerical simulation. The non-depletion assumption is valid in both our simulations and experiments, since the efficiencies are below 1% in either case, as we will see later.

In the oeo process we are studying, we only need to consider the second-order nonlinear polarization field in X direction. The equation is:

$$P_x^{NL} = 4\epsilon_0 d_{eff} \tilde{E}_o \tilde{E}_e \tag{8.9}$$

$$d_{eff} = d_{31} cos\theta \tag{8.10}$$

Note that $d_{31} = d_{15}$ due to Kleinman symmetry [7], Equation 8.10 can be derived from the Equation 8.5. Equation 8.9 is in the time domain. Since we use broadband sources, it is more suitable to work in the frequency domain. Assuming d_{eff} is constant, the Fourier transform of Equation 8.9 is:

$$P_x^{NL}(u,\omega) = 4\epsilon_0 d_{eff} \int_{-\infty}^{\infty} \tilde{E}_o(u,\omega-\omega')\tilde{E}_e(\omega')d\omega' \tag{8.11}$$

The above equation is the nonlinear polarization field at the second harmonic frequency. The linear polarization field at the SH frequency is:

$$P_x^L(u,\omega) = \epsilon_0 \chi(\omega)\tilde{E}_2(u,\omega) = \epsilon_0(n_x^2(\omega)-1)\tilde{E}_2(u,\omega) \tag{8.12}$$

Convert Equation 8.3 into the frequency domain, using the plane wave assumption and the above two equations, we can have an equation of the SH field:

$$(\frac{\partial^2}{\partial u^2} + \frac{\omega^2}{c^2})\tilde{E}_2(u,\omega) = \frac{\omega^2}{c^2}[4d_{eff}\int_{-\infty}^{\infty} \tilde{E}_o(u,\omega-\omega')\tilde{E}_e(\omega')d\omega' - (n_x^2(\omega)-1)\tilde{E}_2(u,\omega)] \tag{8.13}$$

Now we make the substitution:

$$\tilde{E}_m(u,\omega) = \tilde{A}_m(u,\omega)e^{-ik_m(\omega)u} \tag{8.14}$$

Where the 'm' is a general subscript which can be replaced by 'o', 'e' or '2'. Thus $\tilde{A}_m(u,\omega)$ is the field spectrum taking out the propagation effect in the material. Based on non-depletion assumption, $\tilde{A}_o(\omega)$ and $\tilde{A}_e(\omega)$ are also independent of u. The Fourier transforms we will use are:

$$\begin{aligned} A_m(u,t) &= \int \tilde{A}_m(u,\omega)e^{i\omega t}d\omega \\ \tilde{A}_m(u,\omega) &= \frac{1}{2\pi}\int A_m(u,t)e^{-i\omega t}dt \end{aligned} \tag{8.15}$$

$A_o(t)$ and $A_e(t)$ are the input temporal waveform of the fundamental o-wave and e-wave respectively. $A_2(t)$ would be the generated SH waveform before the GVD is taken into account.

Use Equation 8.14 in Equation 8.13, and neglecting the term $\frac{\partial^2}{\partial u^2}\tilde{A}_2(u,\omega)$ (slow-varying approximation), we finally have:

$$\frac{\partial}{\partial u}\tilde{A}_2(u,\omega) = -2id_{eff}(\frac{\omega}{c})^2\frac{e^{ik_2(\omega)u}}{k_2(\omega)}\int_{-\infty}^{\infty}\tilde{A}_o(u,\omega-\omega')e^{-ik_o(\omega-\omega')u}\tilde{A}_e(\omega')e^{-ik_e(\omega')u}d\omega' \tag{8.16}$$

The above equation is easy to solve numerically as long as we know the spectrum of the input waves and the material dispersion ($k_m(\omega)$ functions), and it is the equation we used for numerical simulation.

Analytical results can be obtained when one of the fundamental inputs is a short pulse compared with the other input, and so it can be treated as a temporal δ function. We first consider the case that the fundamental o-wave is a very short pulse and let $\tilde{A}_o \equiv 1$ in Equation 8.16, the integral would be:

$$\int_{-\infty}^{\infty}\tilde{A}_e(\omega')e^{-i(k_o(\omega-\omega')+k_e(\omega'))u}d\omega' \tag{8.17}$$

Ignoring GVD, we can have:

$$\begin{aligned} k_o(\omega-\omega') &= k_o + \frac{1}{V_o}(\omega-\omega'-\omega_1) \\ k_e(\omega') &= k_e + \frac{1}{V_e}(\omega'-\omega_1) \\ k_2(\omega) &= k_2 + \frac{1}{V_2}(\omega-\omega_2) \end{aligned} \tag{8.18}$$

Where k_o, k_e and k_2 are the wave vectors of the three waves at center frequencies $\omega_o = \omega_1$, $\omega_e = \omega_1$ and $\omega_2 = 2\omega_1$ respectively. V denotes the group velocity, and we define the GVM between any two waves as:

$$\beta_{pq} = \frac{1}{V_p} - \frac{1}{V_q} \tag{8.19}$$

Where 'p' and 'q' can be 'o', 'e' or '2'. Use Equation 8.18 and 8.19 in Equation 8.17, the integral can be calculated as:

$$e^{-iu(k_o+k_e+\frac{1}{V_o}(\omega-2\omega_1)+\beta_{oe}\omega_1)}\int\tilde{A}_e(\omega')e^{iu\beta_{oe}\omega}d\omega'$$

$$= A_e(\beta_{oe}u)e^{-iu(k_o+k_e+\frac{1}{V_o}(\omega-\omega_2)+\beta_{oe}\omega_1)} \tag{8.20}$$

We have used the Fourier transformation Equation 8.15. Bring the above result into Equation 8.16 and assume the phase matching condition at center frequencies $k_2 = k_o + k_e$, we can have:

$$\frac{\partial}{\partial u}\tilde{A}_2(u,\omega) = -2i(\frac{\omega}{c})^2\frac{d_{eff}}{k_2(\omega)}A_e(\beta_{oe}u)e^{iu(\beta_{2o}(\omega-\omega_2)-\beta_{oe}\omega_1)} \tag{8.21}$$

And so:

$$\tilde{A}_2(z,\omega) = -2i(\frac{\omega}{c})^2\frac{d_{eff}}{k_2(\omega)}\int_o^z A_e(\beta_{oe}u)e^{iu(\beta_{2o}(\omega-\omega_2)-\beta_{oe}\omega_1)}du \tag{8.22}$$

Here we assume that the crystal is from 0 to z. If the crystal is longer than the interaction length of type II SHG, the integral would be the same as if the boundaries are infinity, then we can use the Fourier transform equation again to get the output SH spectrum:

$$\tilde{A}_2(\omega) = -i(\frac{\omega}{c})^2\frac{d_{eff}}{k_2(\omega)}\frac{4\pi}{\beta_{oe}}\tilde{A}_e(\frac{\beta_{2o}}{\beta_{eo}}(\omega-\omega_2)+\omega_1) \tag{8.23}$$

Note that $\tilde{A}_e(\omega)$ is centered at ω_1, $\tilde{A}_2(\omega)$ is obviously centered at ω_2. We can use Fourier transform again to calculate the temporal field of the output SH wave without GVD:

$$A_2(t) = -id_{eff}\frac{4\pi}{\beta_{oe}c}\int\frac{\omega}{n_2(\omega)}\tilde{A}_e(\frac{\beta_{2o}}{\beta_{eo}}(\omega-\omega_2)+\omega_1)e^{i\omega t}d\omega \tag{8.24}$$

Assuming that $\omega/n_2(\omega) \approx \omega_2/n_2$ is almost constant within the SH spectrum, we can take this term out of the integral and have the SH field:

$$A_2(t) = -id_{eff}\frac{4\pi}{\beta_{oe}c}\frac{\omega_2}{n_2}A_e(\frac{\beta_{eo}}{\beta_{2o}}t)e^{-i\frac{\beta_{eo}}{\beta_{2o}}\omega_1 t}e^{i\omega_2 t} \tag{8.25}$$

We define:

$$A_m(t) = a_m(t)e^{i\omega_m t} \tag{8.26}$$

$a_m(t)$ is then the complex amplitude envelope function. Again 'm' is the general subscript. From Equation 8.25 we have:

$$a_2(t) = -id_{eff}\frac{4\pi}{\beta_{oe}c}\frac{\omega_2}{n_2}a_e(\frac{\beta_{eo}}{\beta_{2o}}t) \tag{8.27}$$

It clearly shows that the output SH waveform is a scaled version of the input waveform. In our case, from Equation 8.2, $\beta_{eo} = 146fs/mm$, $\beta_{2o} = 183fs/mm$ and $\frac{\beta_{eo}}{\beta_{2o}} = 0.8$. So the SH waveform is a magnified version of the input waveform, and the magnification factor is 1.25.

Similarly, if the fundamental e-wave is a δ function, we will have:

$$a_2(t) = -id_{eff}\frac{4\pi}{\beta_{eo}c}\frac{\omega_2}{n_2}a_o(\frac{\beta_{oe}}{\beta_{2e}}t) \tag{8.28}$$

Since $\beta_{oe} = -146fs/mm$, $\beta_{2e} = 37fs/mm$ and $\frac{\beta_{oe}}{\beta_{2e}} = -4$, the SH waveform is a compressed and temporally reversed version of the input waveform, and the compression factor is 0.25.

The physical picture of this waveform transfer technique is: due to the temporal walkoff between the input waveform and the short pulse (called the reference pulse), SHG of different part of the waveform happens at different locations of the crystal. The nonlinear polarization in space is a scaled version of the input temporal profile (assuming a δ pulse reference), and the output SH field in time is a scaled version of the nonlinear polarization in space. And this makes the SH output have temporal features directly scaled to the input waveform. Simple pictures of both the magnification and compression cases are shown in Fig. 8.2.

From Fig. 8.2 and our analysis, it is also clear that the duration of the waveform which can be transfered is related to the crystal length, i. e., the temporal walkoff in the crystal must be long enough for the reference pulse to interact with the whole waveform. Assuming that the reference pulse enters the crystal at a fixed time, the input waveform must enter the crystal within a certain time window to interact with the reference pulse before one of them leaves the crystal. We call this time window the "interaction window". The length of the interaction window is the total temporal walkoff between the two fundamental inputs in the crystal, which is the GVM times the crystal length. For example, in our experiments we use an $L = 10mm$ LBO crystal, and the length of the interaction window is $146fs/mm \times 10mm = 1.46ps$.

If the inputs are focused beams instead of nearly plane waves, another factor which can limit the interaction window is the spatial walkoff between the inputs.

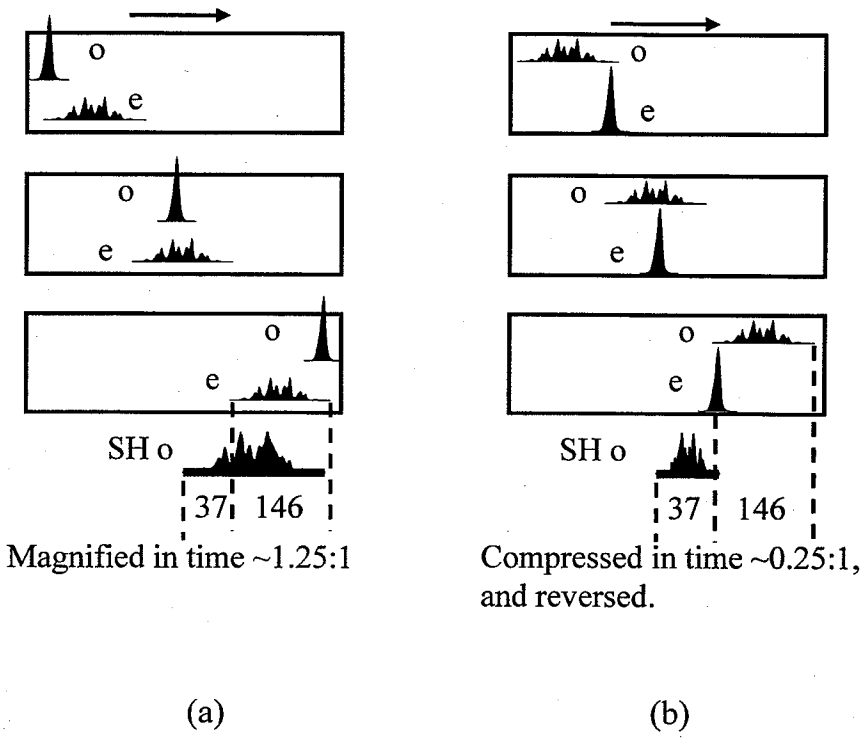

Fig. 8.2. The picture of waveform transfer in type II SHG

To utilize the full length of the crystal, the input beam size must be large enough, otherwise the interaction window is reduced. For example, in our experiments the beam diameter must be larger than $L \tan \rho = 42 \mu m$.

8.2 Simulation Results

We already have the theoretical results when the reference pulse is a δ pulse. But this condition is not true in our experiments. We did numerical simulations using Equation 8.16 for conditions similar to those in our experiments. In the simulation, we assume 100fs duration for a single fundamental pulse, and the center frequency of the fundamental inputs is 805nm. For a beam radius of about $20 \mu m$ and pulse

energy of 10nJ, the average electric field is about $100V/\mu m$. For LBO in this case, $d_{eff} = 0.152pm/V$. And we still use the dispersion relations of LBO in [36]. We also assume that the crystal is long enough to complete the waveform transfer. The simulation results are shown in Fig. 8.3:

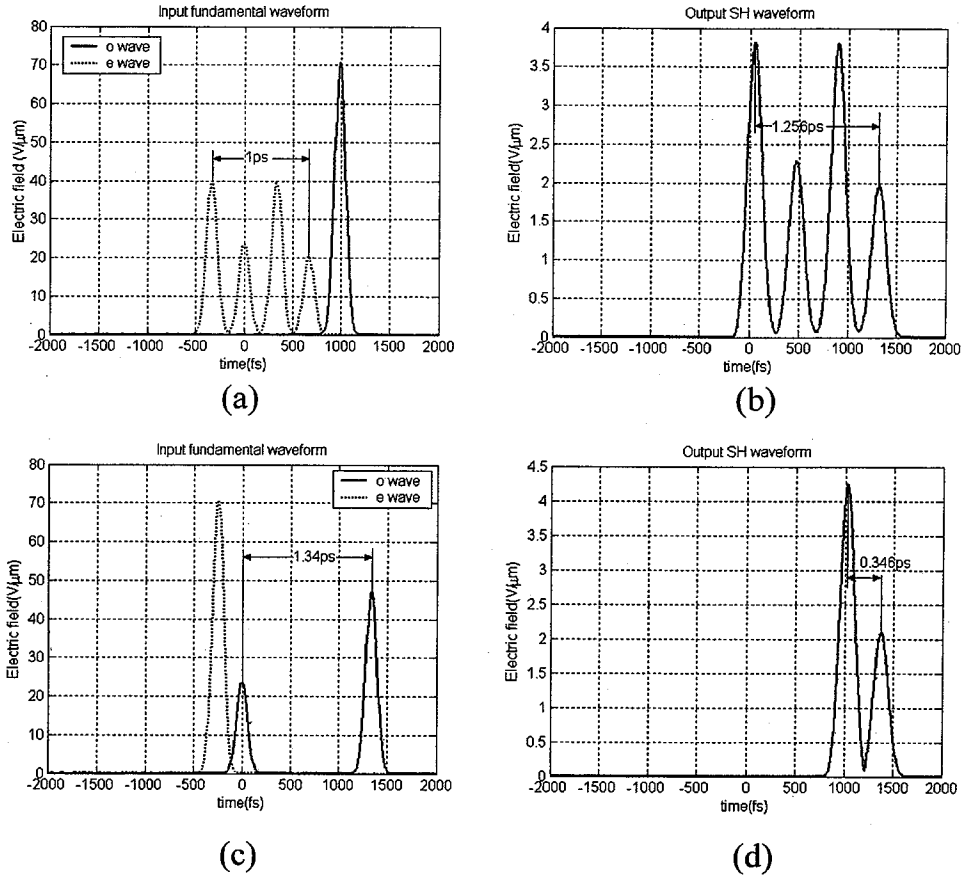

Fig. 8.3. The simulation results of waveform transfer in type II SHG

In Fig. 8.3, subfigures (a, b) is a group and (c, d) is another group. In Fig. 8.3(a), the fundamental o-wave is the reference pulse and the fundamental e-wave has a long waveform. The interval between the leftmost peak and rightmost peak in the input waveform is 1ps. In Fig. 8.3(b), we can see that the output SH wave-

form is a magnified version of the input waveform, as we expected from our simple theoretical analysis in the previous section. The interval between the leftmost peak and rightmost peak in the output waveform is 1.256ps, which matches the predicted magnification factor of 1.25 in the previous section. In this simulation the crystal is assumed to be 10mm long and so the interaction window is about 1.5ps.

In Fig. 8.3(c), the fundamental e-wave is the reference pulse and the fundamental o-wave has a long double-peak waveform. The interval between the left peak and right peak in the input waveform is 1.34ps. In Fig. 8.3(d), the output SH waveform is a compressed and reversed version of the input waveform, which agrees with our expectation. The interval between the left peak and right peak in the output waveform is 0.346ps. Note that 0.346/1.34=0.258, this also proves the predicted compression factor of 0.25. In this simulation the crystal is assumed to be 12mm long and so the interaction window is about 1.75ps.

There are two more things which are worth mentioning in Fig. 8.3. First, the Y axis in the figures represents the electric field, and so the intensity waveform is proportional to its squared value. We can see that the conversion efficiencies in both simulations are below 1%, which validates the non-depletion assumption.

Second, one might also notice that although the interval between the pulses in the waveform is stretched or compressed as predicted, the individual pulse isn't stretched or compressed according to the predicted scaling factors. This is because the reference pulse isn't an ideal δ function in time. If the reference pulse is a δ function, we can expect that the output SH waveform to be an exact scaled version of the input waveform, including the individual pulse durations. But here the reference pulse has the same spectrum and duration as an individual pulse in the waveform. The type II SHG between the reference pulse and an individual pulse in the waveform is symmetrical, and the duration of the output SH pulse cannot be predicted by those scaling factors calculated from group velocities. This is also true in our experiments, since our waveform and reference come from the same source laser.

It is also the reason why we didn't use the 4-peak waveform in Fig. 8.3(a) to do waveform-compression simulation. Because if we did, the interval between the pulses in the SH waveform will be so small that all four pulses merge into one broad peak, which is not a good demonstration.

In this chapter we have studied the waveform transfer from near IR light to blue light using theoretical analysis and simulations. In the next chapter we will present the experimental results.

9. EXPERIMENTS OF WAVEFORM TRANSFER BY TYPE II SHG

9.1 The experimental setup and nonuniform efficiency profile in the interaction window

We have done experiments to demonstrate the waveform transfer from near IR light to blue light through type II SHG. The experimental setup is shown in Fig. 9.1:

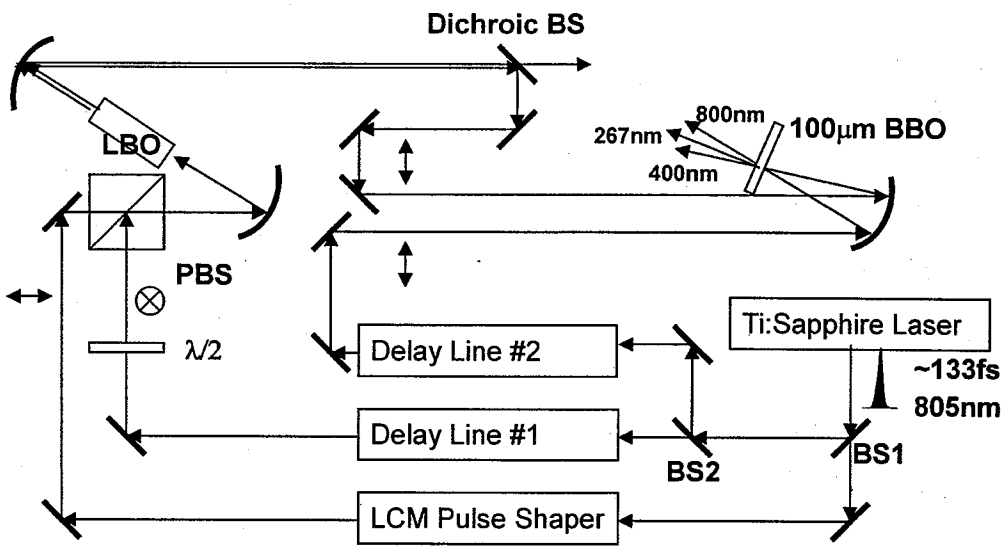

Fig. 9.1. The experimental setup of type II SHG experiments

The source laser is a mode-locked Ti:Sapphire laser. The output pulse has a FWHM intensity duration of 133fs (estimated with the deconvolution factor 1.44), a center wavelength of 805nm and the repetition rate of 88MHz. It's horizontally

polarized. It's split into three arms by two beam splitters (BS). One arm goes through a Fourier-transform pulse shaper with a 512-element liquid crystal modulator (LCM) [42,48]. The pulse shaper can program the near IR waveform and this arm serves as the waveform input of type II SHG. The other two arms have a delay line each. The one that goes through delay line #1 is the reference pulse input of type II SHG. The other that goes through delay line #2 is used for cross-correlation measurements with the output blue waveform.

The polarization of the reference pulse from delay line #1 is rotated 90^o by a half-wave plate and recombined with the pulse shaper output by a polarization beam splitter (PBS). Ideally the pulse shaper output and the reference beam should be collinear after the PBS. They are focused into a 10mm LBO crystal by a spherical mirror with 225mm focal length. Another spherical mirror with 37.5mm focal length collects and collimates the output waves from the LBO. The output blue light is separated from the residal IR light by two dichroic beam splitters. It is then guided to an intensity cross-correlator. There the blue light and the IR pulse from delay line #2 can interact through sum-frequency generation (SFG) in a $100\mu m$ BBO crystal. The generated UV signal at about 267nm is measured by a photo-multiplier tube (PMT, model 1P28A from Hamamatsu Inc.).

As we mentioned before, the 10mm LBO crystal was cut for type II SHG at 800nm with $\theta = 76.88^o$ and $\phi = 90^o$. The polarizations of the reference pulse and the pulse shaper output are perpendicular to each other when entering the crystal as described. While one of them is an o-wave in crystal, the other must be an e-wave. We can switch o-wave and e-wave by using another half-wave plate right after the PBS.

Our calculation in the previous chapter shows that the length of the interaction window for a 10mm LBO is 1.46ps. Inside this window the fundamental waveform can interact with the reference pulse. However, type II SHG of different parts of the waveform happens at different locations in the crystal depending on the relative time delay between the waveform part the reference. If we want the output SH waveform

to be an exact scaled version of the input waveform, the SHG conversion efficiencies at different locations of the crystal must be the same. But this is not true in our experiments. Letting both e-wave and o-wave be single pulses, we measured the SHG efficiencies vs. the delay of the o-wave (or the time when the o-wave pulse enters the crystal). The results are shown in Fig. 9.2:

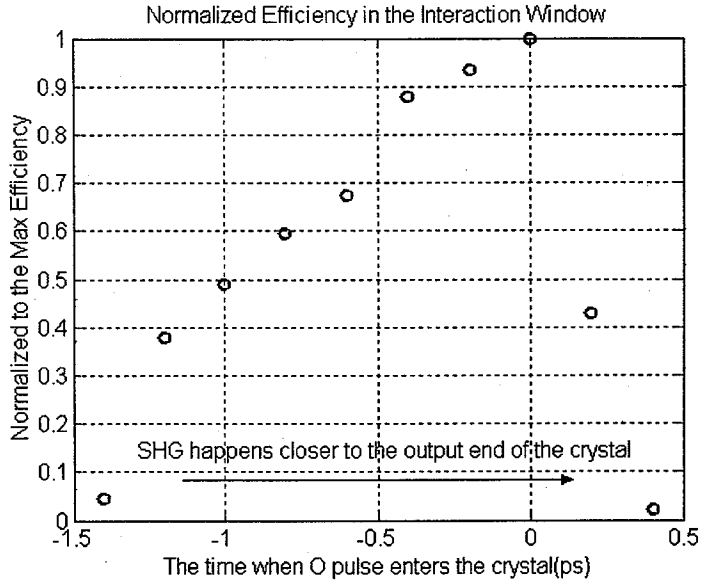

Fig. 9.2. The change of type II SHG efficiency in the interaction window

In Fig. 9.2, the Y axis is the measured efficiency normalized to the max efficiency we had. The max efficiency is 1.3×10^{-4} when o-wave and e-wave pulses each have 38mW average power. The X axis is the relative time when the o-pulse enters the crystal, and the later the time is, the closer to the output end of the crystal SHG happens. We can see that the SHG has the max efficiency when it happens near the output end of the crystal in our case, and it drops to about 40% of the max efficiency when SHG happens near the input end of the crystal. We can also see that the interaction window is indeed approximately 1.5ps long, and the efficiency

drops quickly outside the window, because it means that part of the input pulses is outside the crystal when SHG should happen.

This nonuniform efficiency in the crystal can be attributed to two reasons. First, we use focused beams in our experiments, and so the beam area changes in the crystal due to diffraction. When the beam becomes larger both the field intensity and SHG efficiency drops. Assuming Gaussian beams, we estimated that the confocal parameter ($b = 2\pi n w_0^2/\lambda$) of the beam in the crystal is about 8.5mm, which is a little less than the crystal length. This means that the beam area could be doubled during the propagation in the crystal, which will cause the efficiency to drop by 50%. The second reason is the spatial walkoff between the fundamental o and e waves. The spatial walkoff angle here is 0.24^o, and the total walkoff in a 10mm crystal is $42\mu m$. The e^{-2} intensity beam waist diameter is estimated to be $54\mu m$, and so the spatial walkoff can reduce the spatial overlap between the two input beams and reduce the efficiency as well.

Therefore, in our experiments, the output SH waveform is not only transferred from the input waveform, but also modulated by the nonuniform efficiency profile in the interaction window. If the fundamental inputs were from amplified systems, there would be no need to focus in order to boost the efficiency. Unfocused beams can be considered as nearly plane waves, so both the diffraction and spatial walkoff can be ignored. In that case the efficiency profile in the interaction window would be expected to be uniform. On the other hand, if one wishes to generate a desired waveform at the SH wavelength, it should be possible to take into account the nonuniform efficiency profile when programming the fundamental waveform.

If we were using an amplified system with the same average power (38mW per input pulse) and 1kHz repetition rate, the pulse energy would be 10^5 higher. In that case we can simply use flat mirrors instead of the spherical mirrors in the setup Fig. 9.1. Assuming that we control the beam size so that the e^{-2} input beam radius is 1mm, from our experimental efficiency 1.3×10^{-4} and focused beam radius $27\mu m$, we can estimate the efficiency with amplified pulses to be roughly 1%. With the

1mm beam radius, the confocal parameter of the Gaussian beam would be about 12 meters, while the crystal is only 10mm long and the total spatial walkoff is only $42\mu m$. So the beam diffraction and spatial walkoff could be totally ignored, and we can expect a uniform efficiency of 1% in the interaction window as long as the two inputs are aligned well. It should be reasonable to get several tens of percent efficiency by slight focusing and using higher pulse energies, since some amplified systems can give $1mJ$ pulse energy which is much higher than we assumed ($38\mu J$).

9.2 Experimental waveform transfer results

First, we can demonstrate the magnification and compression effect of this waveform transfer technique without actually using a long waveform input. As we pointed out, when the input o-wave is a δ pulse, the input e-waveform is transferred and the magnification factor is 1.25; when the input e-wave is a δ pulse, the input o-waveform is transferred and the compression factor is -0.25 (negative means temporal reversion). Another way to inspect this phenomenon is: if both inputs are single pulses, then the time when the SH pulse leaves the crystal is related to the times when the two input pulses enter the crystal by a linear equation, and the corresponding linear factors should be the above magnification and compression factors. Assuming that the fundamental o-pulse enters the crystal at t_o and the fundamental e-pulse enters at t_e, they will meet in the crystal at length l_1 and time t_1, which are calculated from their group velocities:

$$l_1 = (t_o - t_e)(\frac{1}{V_e} - \frac{1}{V_o})^{-1} = \frac{t_o - t_e}{\beta_{eo}} \tag{9.1}$$

$$\begin{aligned} t_1 &= t_e + \frac{l_1}{V_e} = t_o + \frac{l_1}{V_o} \\ &= \frac{t_o}{V_e \beta_{eo}} - \frac{t_e}{V_o \beta_{eo}} \end{aligned} \tag{9.2}$$

The SH pulse is generated when the two inputs meet, and travels at its own group velocity V_2. The time when the SH pulse leaves the crystal is:

$$t_2 = t_1 + \frac{L - l_1}{V_2} = \frac{\beta_{2o}}{\beta_{eo}} t_e + \frac{\beta_{e2}}{\beta_{eo}} t_o + \frac{L}{V_2} \tag{9.3}$$

L is the crystal length. The two linear factors here $\frac{\beta_{2o}}{\beta_{eo}}$ and $\frac{\beta_{e2}}{\beta_{eo}}$ are the same as what we can derive from Equation 8.27 and 8.28. Note that there is always $\frac{\beta_{2o}}{\beta_{eo}} + \frac{\beta_{e2}}{\beta_{eo}} = \frac{\beta_{eo}}{\beta_{eo}} = 1$. If the fundamental o-pulse is faster than the e-pulse in the crystal, there must be $t_o > t_e$ or they won't interact. For the type II SHG we are studying, ignoring the constant time delay $\frac{L}{V_2}$, we can have:

$$t_2 = 1.25 t_e - 0.25 t_o \tag{9.4}$$

From this relationship, if we temporally delay the input e-pulse, the SH pulse will also be delayed, and the amount of its delay is 1.25 times of the e-pulse delay; if we temporally delay the input o-pulse, the SH pulse will actually appear earlier in time, which is a negative delay 0.25 times of the o-pulse delay. This is a seemingly strange phenomenon. It is due to the fact that the fundamental o-pulse has the fastest speed in the crystal. Although delaying it causes the SH pulse to be generated later in crystal, it's also generated closer to the output end of the crystal, so in the end the SH pulse leaves the crystal earlier!

If we delay both input pulses by the same amount of time, according to Equation 9.4 the SH pulse should also be delayed by the same time, which is physically obvious from causality. The causality also requires that the sum of the two linear factors (including sign) to be 1, which is automatically satisfied by Equation 9.3. We have demonstrated Equation 9.4 in an experiment. While changing the delay of one of the input pulses, we observe the peak delay of the SH pulse. The results are shown in Fig. 9.3, which undoubtedly proved our analysis.

Now we demonstrate the waveform transfer technique using a long waveform input and a short pulse input. Fig. 9.4 shows some experimental results which demonstrate the waveform transfer from near IR wavelength to blue wavelength.

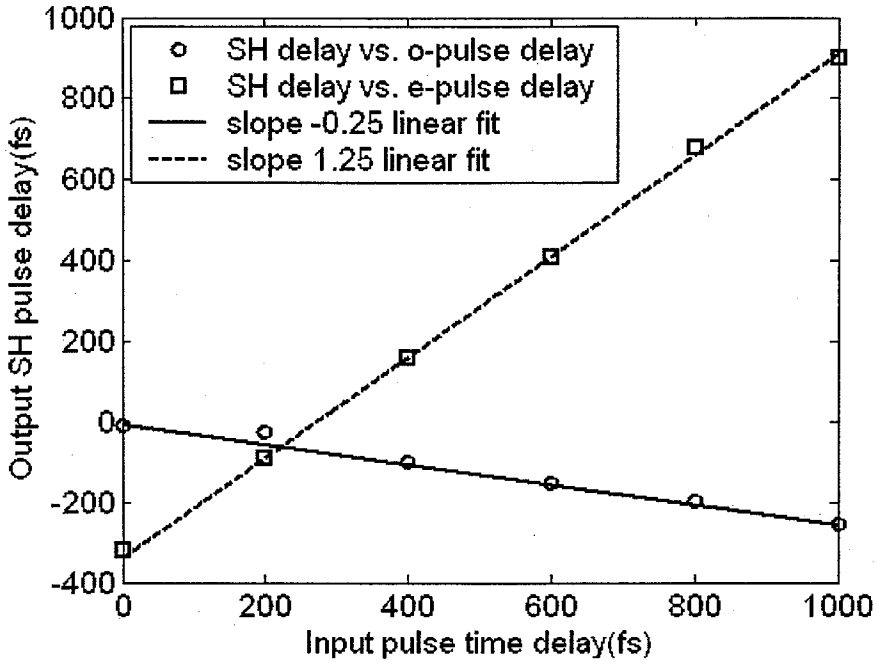

Fig. 9.3. The dependence of the SH pulse delay on the two input pulse delays.

In Fig. 9.4(a), the fundamental waveform (top figure) mainly consists of two asymmetrical pulses, and the interval between the peaks is 980fs. The phase array on the 512-pixel LCM we used to generate this waveform is the superposition of two phase arrays: one is a (0 π 0 π...) periodic phase array with 8-pixel bin size; the other is a linear phase array with $\frac{\pi}{8}$/pixel slope. In the magnification configuration (middle figure), the output SH waveform also has two asymmetrical pulses; the order of the high peak and low peak remains the same. The interval between the peaks is 1.22ps in the SH waveform. The magnification factor 1.22/0.98=1.245 matches the predicted value of 1.25 very well. In the compression configuration (bottom figure), there are two asymmetrical pulses, but the interval between them has been compressed so much that part of them has merged. We can still see that the order of the high peak and low peak is reversed as predicted. The interval between the peaks

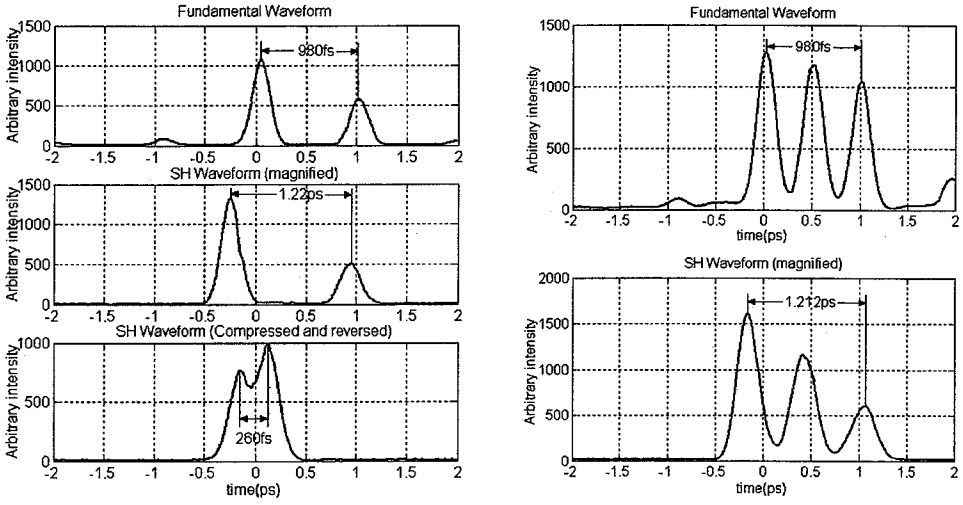

(a) (b)

Fig. 9.4. The waveform transfer experiments: magnified or compressed

is 260fs. The compression factor 26/98=0.265 also matches the predicted value of 0.25 very well.

We can also see the modulation effect of the nonuniform efficiency profile in the interaction window from Fig. 9.4(a). In the fundamental waveform, the ratio of the two peak heights is about 2:1. In the magnification configuration, the fundamental waveform is e-wave in the crystal, which propagates slower than the reference pulse. And so the transfer of the earlier (higher) pulse happens closer to the output end of the crystal. Based on Fig. 9.2, it got higher efficiency than the later (lower) pulse. As a result, we see that in the middle figure, the ratio of the peak heights is increased to about 2.7:1. In the compression configuration, the roles of the fundamental o-wave and e-wave are switched and so the opposite happens. As a result, in the bottom figure, the ratio of the peak heights is decreased to about 1.3:1.

In Fig. 9.4(b), the fundamental waveform (top figure) mainly consists of three pulses with decreasing heights in time. The interval between the leftmost peak and rightmost peak is 980fs. The phase array on the LCM is again the superposition of two phase arrays: one is a (0 0.635π 0 0.635π...) periodic phase array with 8-pixel bin size; the other is a linear phase array with $\frac{\pi}{8}$/pixel slope. The output SH waveform using the magnification configuration is shown in the bottom figure. The three pulses are still in decreasing order in time, and the interval between the leftmost and rightmost peaks is 1.212ps. The magnification factor is 1.212/0.98=1.24, which also matches the predicted 1.25 very well. We can also see the modulation effect of the nonuniform efficiency profile, which increases the relative differences of peak heights in this case. We didn't use the compression configuration here because the three pulses would merge into one broad peak in the output.

It is worth mentioning that in Fig. 9.4, the small ripples in the fundamental waveforms no longer show up in the output SH waveforms because they are out of the interaction window. This means that this waveform transfer technique also has the function of a temporal filter.

In the above experiments, the main part of the fundamental waveform is within the interaction window. If the fundamental waveform is longer than the interaction window, it is not possible to transfer the whole waveform. On the other hand, we can selectively transfer part of the waveform by tuning the relative delay between the fundamental waveform and the reference pulse, thus moving the temporal region of the interaction window. An experimental demonstration is shown in Fig. 9.5.

In Fig. 9.5, the top figure is the fundamental waveform. Obviously it's longer than the interaction window (1.5ps). The phase array on the LCM is a periodic array with repeating period of ($00\pi0\pi\pi\pi$), and the bin size is two pixels. We use the magnification configuration here. By controlling the delay of the reference pulse, we can control the temporal region of the interaction window in the fundamental waveform. In the middle figure, the interaction window is approximately -1.2ps to 0.3ps, and we can see that the three pulses at -1.1ps, -0.6ps and 0ps in the

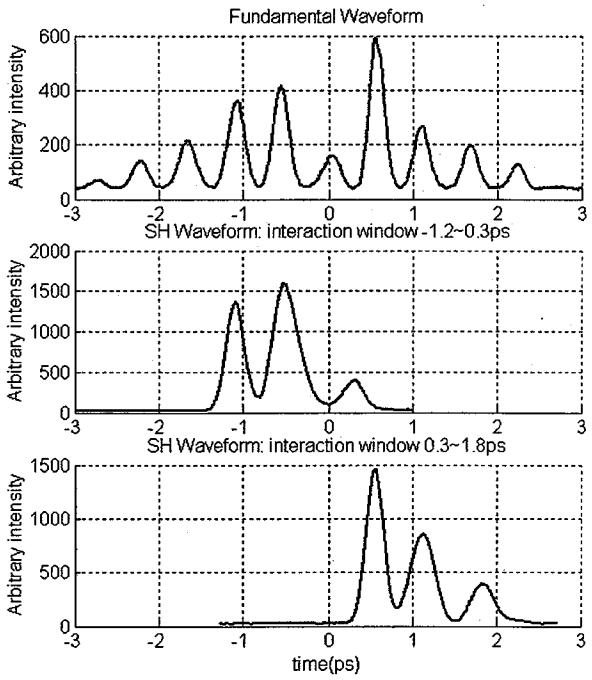

Fig. 9.5. The waveform transfer experiments: Selectable interaction window

fundamental waveform are transferred to the output SH waveform. In the bottom figure, the interaction window is approximately 0.3ps to 1.8ps, and the three pulses at 0.5ps, 1.1ps and 1.7ps are transferred. Thus the selectable interaction window is successfully demonstrated.

We have demonstrated that type II SHG can transfer the temporal intensity profile from the fundamental wavelength to the SH wavelength. Based on Equation 8.27 and 8.28, presumably it should be able to transfer the phase profile as well. Those two equations showed that if the reference pulse is a temporal δ function, the temporal phase profile of the fundamental waveform will also be copied to the output SH waveform, satisfying the same magnification or compression factor as the intensity profile. In our experiments, the reference pulse cannot be treated as a δ

function, and so the phase profile of the fundamental waveform is averaged over the reference pulse when it's transferred to the SH output.

We have designed an experiment to demonstrate that a linear chirp can be transferred from the fundamental waveform to the SH waveform. The idea is: we can use the LCM pulse shaper to add an up chirp or down chirp to broaden the fundamental e-pulse while keeping the fundamental o-pulse unaffected. In that sense the o-pulse is the reference here and this is still the magnification configuration. We can control the amount of up chirp and down chirp so that the broadened pulses have approximately the same duration in both cases. After type II SHG with the reference pulse, the output SH pulses should also have similar intensity durations in both cases, but we need to prove that they carry up chirp or down chirp according to the chirped fundamental pulses. To demonstrate it, we let the SH pulse go through a normal dispersive media which will add an up chirp to the pulse due to normal dispersion. If the SH pulse is originally down chirped, the dispersive media could compress the pulse and make it shorter; if the SH pulse is originally up chirped, the dispersive media will further broaden the pulse. If we observe these phenomena, they are a strong evidence that the phase profiles of the fundamental waveform are also transferred to the SH waveform.

In the experiments, we combined two prisms to be the dispersive media. The media is LaSFN9 glass, and the thickness is 26mm. The total linear dispersion (or quadratic spectral phase) added by the glass at 400nm wavelength is calculated to be $\frac{d^2\phi}{d\omega^2} = -1.63 \times 10^4 fs^2$ (up chirp). The quadratic spectral phase added by the LCM at 800nm is calculated to be $\frac{d^2\phi}{d\omega^2} = \pm 9.05 \times 10^3 fs^2$ (positive means down chirp). The bandwidth of the source laser is 4.6THz. The phase transfer here cannot be determined by Equation 8.27 or 8.28 because our reference is not narrow comparing with the waveform. We did numerical simulations and it shows that the spectral quadratic phase in the SHG output is about 1.6 times of the fundamental chirp. So we have $9.059 \times 10^3 fs^2 \times 1.6 = 1.45 \times 10^3 fs^2$, which roughly meets the calculated glass dispersion. The experimental results are shown in Fig. 9.6.

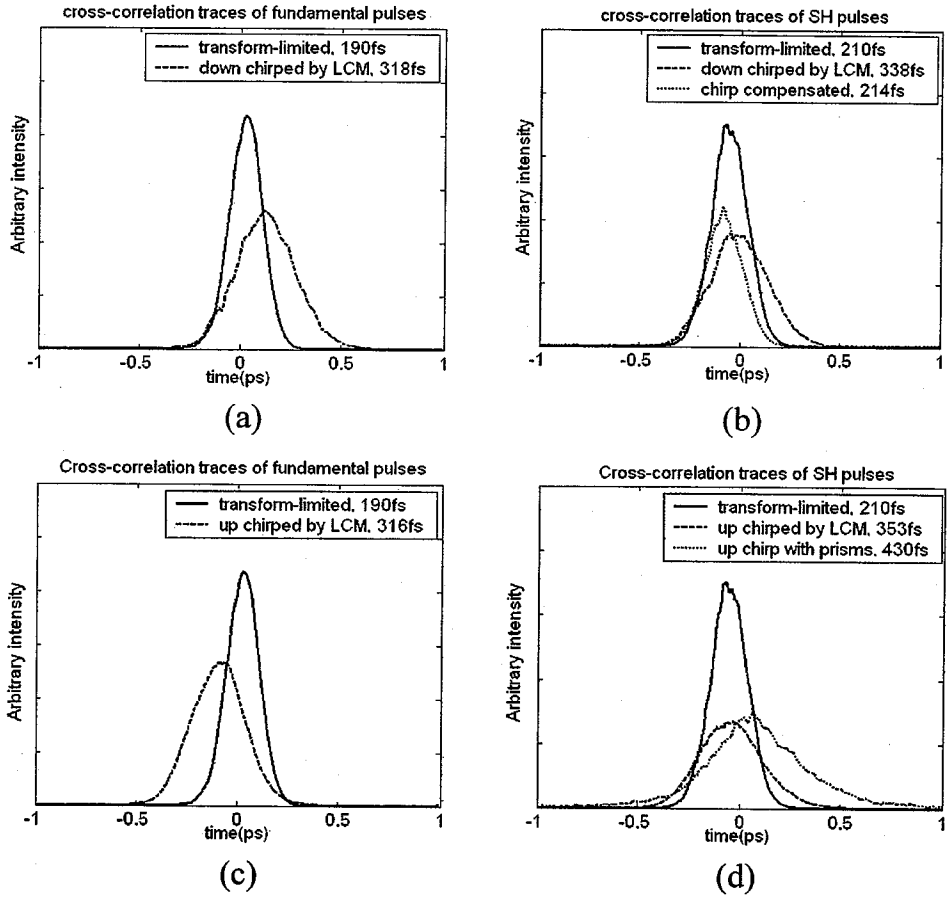

Fig. 9.6. The waveform transfer experiments: Phase transfer

In Fig. 9.6(a), we show the cross-correlation traces of the transform-limited (solid line) and the down chirped (dashed line) fundamental pulse. The numbers shown in the figures are all the FWHM width of the traces. The fundamental pulse is obviously broadened by the chirp. In Fig. 9.6(b), three traces of the SH pulse are shown. The solid curve is the trace of the SH pulse generated by the transform-limited fundamental pulse (no prism glass), and the width is 210fs. The dashed curve is generated by the down chirped fundamental pulse (no prism glass), and it's broadened to 338fs. The dotted curve is the trace of the SH pulse generated by the down chirped fundamental pulse but after it passes the prism glass, and we can see that it's compressed to 214fs, almost as short as the transform-limited trace. This clearly proves that the SH pulse generated by the down chirped fundamental pulse is also down chirped.

Fig. 9.6(c, d) show an experiment in which the fundamental pulse is up chirped. They are in comparison with Fig. 9.6(a, b). In Fig. 9.6(c), we see that the up chirped fundamental pulse has approximately the same duration as the down chirped pulse in Fig. 9.6(a). In Fig. 9.6(d), the trace of the SH pulse generated by the up chirped fundamental pulse (no prism glass) has a width of 353fs, which is very close to the 338fs trace in Fig. 9.6(b). However, after it passes the prism glass the trace is further broadened instead of compressed. Comparing the two experiments in Fig. 9.6, we can conclude that the linear chirp in the fundamental waveform was transferred to the SH waveform by type II SHG. It's an evidence that the phase profile of the waveform can also be transferred by this technique.

10. CONCLUSION OF TYPE II SHG STUDY

We have demonstrated both theoretically and experimentally the waveform transfer from 800nm light to 400nm light by type II SHG in a LBO crystal. We have shown that the SH waveform can be a magnified or compressed version of the fundamental waveform depending on the configuration. The interaction window in our experiments was about 1.5ps, but it can be extended by using longer crystals or crystals with larger GVMs. Theoretical and experimental studies indicate that this method can transfer not only the intensity profiles of a waveform, but also the phase profiles. We consider type II SHG as a novel and promising method to generate programmable waveforms down to the UV range, especially for amplified systems.

LIST OF REFERENCES

LIST OF REFERENCES

[1] P. A. Franken, A. E. Hill, C. W. Peters, and G. Weinreich. Generation of optical harmonics. *Phys. Rev. Letters 7*, page 118, 1961.

[2] E. P. Ippen and C. V. Shank. *Ultrashort Light Pulses.* Second edition, 1984.

[3] R. Trebino and D. J. Kane. Using phase retrieval to measure the intensity and phase of ultrashort pulses: frequency-resolved optical gating. *Journal Opt. Soc. Am. A. 10*, pages 1101–1111, 1999.

[4] S. A. Akhmanov and R. V. Khokhlov. *Problems of Nonlinear Optics.* Viniti, Moscow, 1964.

[5] N. Bloembergen. *Nonlinear Optics.* Benjamin, New York, 1965.

[6] F. Zernicke and J. E. Midwinter. *Applied Nonlinear Optics.* Wiley, New York, 1973.

[7] D. A. Kleinman. *Phys. Rev. 126*, pages 1977–1979, 1962.

[8] R. W. Boyd. *Nonlinear Optics.* 1992.

[9] V. G. Dmitriev, G. G. Gurzadyan, and D. N. Nikogosyan. *Handbook of Nonlinear Optical Crystals.* Second edition, 1997.

[10] D. A. Kleinman. Theory of second harmonic generation of light. *Phys. Rev. 128*, page 1761, 1962.

[11] G. D. Boyd, A. Ashkin, J. M. Dziedzic, and D. A. Kleinman. Second-harmonic generation of light with double refraction. *Phys. Rev. 137(4A)*, page 1305, 1965.

[12] D. A. Kleinman, A. Ashkin, , and G. D. Boyd. Second-harmonic generation of light by focused laser beams. *Phys. Rev. 145*, page 338, 1966.

[13] G. D. Boyd and D. A. Kleinman. Parametric interaction of focused gaussian light beams. *Journal of Applied Physics 39(8)*, page 3597, 1968.

[14] S. A. Akhmanov, A. P. Sukhorukov, , and A. S. Chirkin. Nonstationary phenomena and space-time analogy in nonlinear optics. *Sov. Phys. JETP 28*, page 748, 1968.

[15] R. C. Miller. Second harmonic generation with a broadband optical maser. *Phys. Lett. A 26*, page 177, 1968.

[16] J. Comly and E. Garmire. Second harmonic generation from short pulses. *Appl. Phys. Lett. 12*, page 7, 1968.

[17] W. H. Glenn. Second-harmonic generation by picosecond optical pulses. *IEEE J. Quantum Electron. QE-5*, page 284, 1969.

[18] A. M. Weiner. Effect of group-velocity mismatch on the measurement of ultrashort optical pulses via 2nd harmonic-generation. *IEEE J. Quantum Electron. 19(8)*, pages 1276–1283, 1983.

[19] G. Imeshev, M. A. Arbore, S. Kasriel, , and M. M. Fejer. Pulse shaping and compression by second-harmonic generation with quasi-phase-matching gratings in the presence of arbitrary dispersion. *J Opt. Soc. Am. B 17(8)*, pages 1420–1437, 2000.

[20] A. M. Weiner, A. M. Kan'an, and D. E. Leaird. High efficiency blue generation by frequency doubling of femtosecond pulses in a thick nonlinear crystal. *Opt. Lett. 23(18)*, pages 1441–1443, 1998.

[21] Y. Q. Li, D. Guzun, G. Salamo, and M. Xiao. High-efficiency blue-light generation by frequency doubling of picosecond pulses in a thick $KNbO_3$ crystal. *J. Opt. Soc. Am. B 20(6)*, pages 1285–1289, 2003.

[22] S. Yu and A. M. Weiner. Phase-matching temperature shifts in blue generation by frequency doubling of femtosecond pulses in $KNbO_3$. *J. Opt. Soc. Am. B 16(8)*, pages 1300–1304, 1999.

[23] Z. Zheng, A. M. Weiner, K. R. Parameswaran, M. H. Chou, and M. M. Fejer. Femtosecond second-harmonic generation in periodically poled lithium niobate waveguides with simultaneous strong pump depletion and group-velocity walkoff. *J. Opt. Soc. Am. B 19(4)*, pages 839–848, 2002.

[24] D. Guzun, Y. Q. Li, and M. Xiao. Blue light generation in single-pass frequency doubling of femtosecond pulses in $KNbO_3$. *Opt. Commun. 180*, pages 367–371, 2000.

[25] L. E. Busse, L. Goldberg, M. R. Surette, and G. Mizell. Absorption losses in MgO-doped and undoped potassium niobate. *J. Appl. Phys. 75 (2)*, pages 1102–1110, 1994.

[26] A. V. Smith, R. J. Gehr, and M. S. Bowers. Numerical models of broadbandwidth nanosecond optical parametric oscillators. *J. Opt. Soc. Am. B 16(4)*, pages 609–619, 1999.

[27] www.sandia.gov/imrl/xweb1128/xxtal.htm.

[28] J. A. Arnaud and H. Kogelnik. Gaussian light beams with general astigmatism. *Appl. Optics 8*, page 1687, 1969.

[29] I. S. Gradshteyn and I. M. Ryzhik. *Table of integrals, series, and products.* Fifth edition, 1996.

[30] S. Ramo, J. R. Whinnery, and T. V. Duzer. *Fields and waves in communication electronics Appendix 1.* Third edition, 1993.

[31] Vittorio Magni. Optimum beams for efficient frequency mixing in crystals with second order nonlinearity. *Opt. Commun. 184*, pages 245–255, 2000.

[32] Guo-Ding Xu, Tie-Wei Ren, Yue-Hua Wang, Yong-Yuan Zhu, Shi-Ning Zhu, and Nai-Ben Ming. Third-harmonic generation by use of focused gaussian beams in an optical superlattice. *J. Opt. Soc. Am. B 20*, pages 360–365, 2003.

[33] T. W. Tukker, C. Otto, and J. Greve. Elliptical-focusing effect on parametric oscillation and downconversion. *J. Opt. Soc. Am. B 15 (9)*, pages 2455–2461, 1998.

[34] D. A. Roberts. Simplified characterization of uniaxial and biaxial nonlinear optical crystals - a plea for standardization of nomenclature and cenventions. *IEEE J Quantum Elect. 28(10)*, pages 2057–2074, 1992.

[35] K. Kato. 2nd-harmonic generation to 2048 $\mathring{A}$ in β-BaB_2O_4. *IEEE J. Quantum Elect. 22*, pages 1013–1014, 1986.

[36] K. Kato. Tunable UV generation to 0.2325μm in LiB_3O_5. *IEEE J. Quantum Elect. 26*, pages 1173–1175, 1990.

[37] F. Eickemeyer, R. A. Kaindl, M. Woerner, T. Elsaesser, and A. M. Weiner. Controlled shaping of ultrafast electric field transients in the mid-infrared spectral range. *Opt. Lett. 25 (19)*, pages 1472–1474, 2000.

[38] T. Witte, D. Zeidler, D. Proch, K. L. Kompa, and M. Motzkus. Programmable amplitude- and phase-modulated femtosecond laser pulses in the mid-infrared. *Opt. Lett. 27(2)*, pages 131–133, 2002.

[39] H. S. Tan and W. S. Warren. Mid infrared pulse shaping by optical parametric amplification and its application to optical free induction decay measurement. *Opt. Express 11(9)*, pages 1021–1028, 2003.

[40] N. Belabas, J. P. Likforman, L. Canioni, B. Bousquet, and M. Joffre. Coherent broadband pulse shaping in the mid infrared. *Opt. Lett. 26(10)*, pages 743–745, 2001.

[41] A. Umbrasas, J. C. Diels, J. Jacob, G. Valiulis, and A. Piskarskas. Generation of femtosecond pulses through 2nd-harmonic compression of the output of a ND-YAG laser. *Opt. Lett. 20 (21)*, pages 2228–2230, 1995.

[42] A. M. Weiner. Femtosecond optical pulse shaping and processing. *Prog. Quantum Electron. 19*, pages 161–238, 1995.

[43] M. Hacker, G. Stobrawa, R. Sauerbrey, T. Buckup, M. Motzkus, M. Wildenhain, and A. Gehner. Micromirror SLM for femtosecond pulse shaping in the ultraviolet. *Appl. Phys. B 76(6)*, pages 711–714, 2003.

[44] Y. Q. Liu, S. G. Park, and A. M. Weiner. Enhancement of narrow-band terahertz radiation from photoconducting antennas by optical pulse shaping. *Opt. Lett. 21(21)*, pages 1762–1764, 1996.

[45] M. Hacker, R. Netz, M. Roth, G. Stobrawa, T. Feurer, and R. Sauerbrey. Frequency doubling of phase-modulated, ultrashort laser pulses. *Appl. Phys. B 73(3)*, pages 273–277, 2001.

[46] Z. Zheng and A. M. Weiner. Coherent control of second harmonic generation using spectrally phase coded femtosecond waveforms. *Chem. Phys. 267*, pages 161–171, 2001.

[47] G. Imeshev, A. Galvanauskas, D. Harter, M. A. Arbore, M. Proctor, and M. M. Fejer. Engineerable femtosecond pulse shaping by second-harmonic generation with fourier synthetic quasi-phase-matching gratings. *Opt. Lett. 23(11)*, pages 864–866, 1998.

[48] H. Wang, Z. Zheng, D. E. Leaird, A. M. Weiner, T. A. Dorschner, J. J. Fijol, L. J. Friedman, H. Q. Nguyen, and L. A. Palmaccio. 20-fs pulse shaping with a 512-element phase only liquid crystal modulator. *IEEE J. Selected Topics in Quantum Elect. Vol. 7 No. 4*, pages 718–727, 2001.

[49] V. G. Dmitriev and D. N. Nikogosyan. Effective nonlinearity coefficients for 3-wave interactions in biaxial crystals of mm2 point group symmetry. *Opt. Commun. 95*, pages 173–182, 1993.

APPENDIX

APPENDIX A

THE DERIVATION OF Ψ_K

Here we will derive Equation 2.6 in detail.

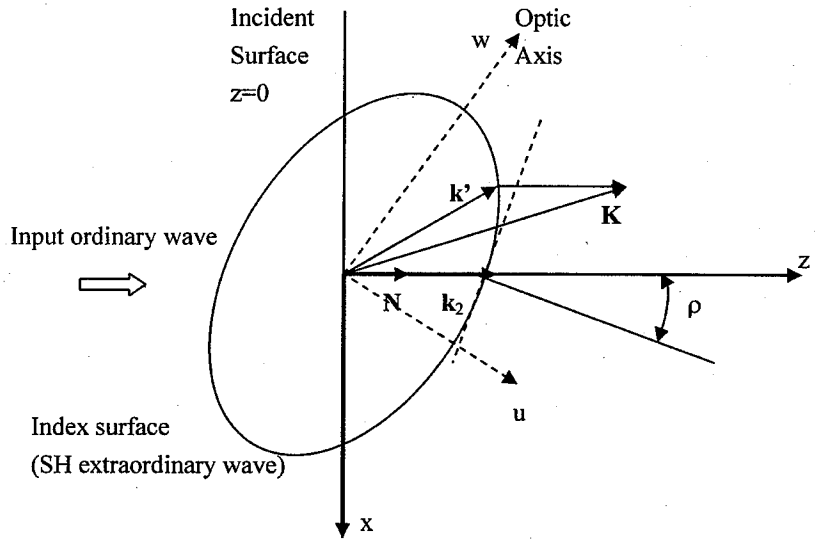

Fig. A.1. The index surface and the vector mismatch relationship

Fig. A.1 is Fig. 2.2 plus a new coordinates system (u, v, w), where w axis is along the optic axis, v axis is the same as y axis (perpendicular to the figure plane) and u axis is orthogonal to both v and w axis. Using these new coordinates, the index surface of SH e-wave in the $\vec{k}$ space is described by:

$$\frac{k_u^2 + k_v^2}{n_o^2} + \frac{k_w^2}{n_e^2} = k_{vac}^2 \tag{A.1}$$

k_{vac} is the wave vector of the SH wave in vacuum. By a rotation of θ (it can be any angle but here we specifically mean the phase matching angle), we can derive the index surface function in (x, y, z) coordinates:

$$f(k_x, k_y, k_z) = \frac{k_x^2}{n_x^2} + \frac{k_y^2}{n_o^2} + \frac{k_z^2}{n_z^2} + 2sk_xk_z = k_{vac}^2 \tag{A.2}$$

$$n_x = (\frac{\cos^2\theta}{n_o^2} + \frac{\sin^2\theta}{n_e^2})^{-\frac{1}{2}} \tag{A.3}$$

$$n_z = (\frac{\sin^2\theta}{n_o^2} + \frac{\cos^2\theta}{n_e^2})^{-\frac{1}{2}} \tag{A.4}$$

$$s = \sin\theta\cos\theta(\frac{1}{n_e^2} - \frac{1}{n_o^2}) \tag{A.5}$$

The wave vector of the SH wave is along the Z axis (the same direction as the input fundamental wave), and so we have $k_2 = n_z k_{vac}$. The walk-off angle ρ is the angle between z axis and the normal to the index surface at the point $\vec{k_2}$, and so $\tan\rho = -\frac{\partial k_z}{\partial k_x}|(k_x = k_y = 0) = n_z^2 s$. From Equation 2.4, what we want to calculate is $(\vec{K} - \vec{k'}) \bullet \vec{N} = K_z - k'_z$. What we already know is that $k'_x = K_x$, $k'_y = K_y$ and $\vec{k'}$ is on the index surface. So we have:

$$\frac{K_x^2}{n_x^2} + \frac{K_y^2}{n_o^2} + \frac{k_z'^2}{n_z^2} + 2sK_xk'_z = k_{vac}^2 \tag{A.6}$$

The positive solution of k'_z is:

$$\begin{aligned} k'_z &= n_z^2\left[-sK_x + \sqrt{s^2K_x^2 + \frac{1}{n_z^2}(k_{vac}^2 - \frac{K_x^2}{n_x^2} + \frac{K_y^2}{n_o^2})}\right] \\ &= -K_x\tan\rho + n_z\sqrt{k_{vac}^2 - (\frac{1}{n_x^2} - s^2n_z^2)K_x^2 - \frac{K_y^2}{n_o^2}} \end{aligned} \tag{A.7}$$

Using some algebra we can get:

$$\frac{1}{n_x^2} - s^2n_z^2 = \frac{n_z^2}{n_o^2n_e^2} \tag{A.8}$$

In the region we are studying there is $K_x, K_y << k_{vac}$, so Equation A.7 can be simplified to:

$$\begin{aligned} k'_z &= -K_x\tan\rho + n_z\left[k_{vac} - \frac{1}{2k_{vac}}(\frac{n_z^2K_x^2}{n_o^2n_e^2} + \frac{K_y^2}{n_o^2})\right] \\ &= k_2 - K_x\tan\rho - \frac{1}{2k_2}(\frac{n_z^4K_x^2}{n_o^2n_e^2} + \frac{n_z^2K_y^2}{n_o^2}) \end{aligned} \tag{A.9}$$

Because the second order terms are just small modifications and the crystal is usually nearly isotropic, it is proper that we take $n_o \approx n_e \approx n_z$ in the brackets. It is equivalent to assume that a small area of the index surface around k_2 is close to part of a sphere. And we have:

$$(\vec{K} - \vec{k'}) \bullet \vec{N} = K_z - k'_z = K_z - k_2 + K_x \tan\rho + \frac{K_x^2 + K_y^2}{2k_2} \tag{A.10}$$

Substitute this equation into Equation 2.4, and we can see that Equation 2.6 is proved.

VITA

VITA

I was born in Wuhan city, central China in 1975. I completed the elementary school and middle school in my hometown. In 1993 I went to Tsinghua University in Beijing, which has the best engineering school in China. In 1998 I accepted the offer from Purdue University and became a Ph. D student here. In these five years I have learned a lot and made new friends. It's been an enjoyable experience I will always remember.